Optimal Interferometric Maneuvers for Distributed Telescopes

Master of Science Degree Thesis

Author:
Marc Diaz Aguilo

Supervisor:
Dr. Alvar Saenz-Otero

Space Systems Laboratory
Massachusetts Institute of Technology (MIT)
Cambridge (USA)

Institut Supérieur de l'Aéronautique et de l'Espace
SUPAERO
Toulouse (France)

E. T. S. d'Enginyeria de Telecomunicació de Barcelona
Telecom-BCN
Universitat Politècnica de Catalunya (UPC)

September 4, 2008

Optimal Interferometric Maneuvers for Distributed Telescopes

by Marc Diaz Aguilo

Research realized at the Space Systems Laboratory (Massachusetts Institute of Technology, Cambridge, USA) and submitted to Institute Supérieure de l'Aéronautique et de l'Espace (SUPAERO, Toulouse, FRANCE) on September 4, 2008 in Fulfillment of the requirements for the Double Degree of Master of Science *Ingénieur SUPAERO - Enginyer Superior de Telecomunicació (ETSETB, UPC, Barcelona)* and for *Master de Recherche SAID* from École Doctorale Systèmes, Toulouse, FRANCE.

Abstract

The scientific community has proposed several missions to expand our knowledge about the universe, its formation and search for distant Earth-like planets. Most of the present space-based observation missions have reached angular resolution limits, therefore the potential benefits concerning angular resolution and intensity that can be reaped from the realization of interferometry within a distributed satellite telescope have led to the proposal of several multi-spacecraft systems. Among these missions synthetic imaging space based interferometers, consisting of multiple telescope apertures flying in controlled formation in order to combine received information from each of the flotilla members are nowadays the subject of interesting research. The objective of synthesizing images with high angular resolution, low ambiguity and high intensity is always a tradeoff with the whole fuel consumption of the mission.

As a consequence, this research focuses on the design of interferometric maneuvers and optimal interferometric controllers balancing image performance and energy consumption. The first part of the thesis presents the optimization and design process of coordinated spiral maneuvers due to their interferometric interest when filling the frequency plane of the observed image. On the other hand, the second part of this work focuses in the resolution of an optimal control problem within the LQ framework, to determine the optimal imaging reconfigurations of a formation flying system. Its objective is to balance the quality of the celestial observation and the usage of fuel, which are the key aspects of any space-based observation mission. This study concerning implementability and performance of interferometric maneuvers will lead towards the enlargement of mission lifetime and flexibility of the system conserving acceptable quality observations.

Acknowledgements

First of all, I would like to thank Dr. Alvar Saenz-Otero for giving the possibility of pursuing this research within the Space Systems Laboratory (Massachusetts Institute of Technology). At the same time, I really appreciate the help of Prof. David Miller, Dr. Alvar Saenz-Otero and specially Christophe Mandy. Thank you for helping me conducting this work within your research group and for your advice and guidance. I would like to thank as well everybody in the Lab for making research so interesting and for being so helpful.

One special thank as well for Dr. Caroline Berard and Dr. Daniel Alazard for all their help during my stay at SUPAERO. Everything has been easier with their teaching, their comprehension and their help.

I appreciate the economic help from CTAE (Centre Tecnològic d'Aeronàutica i Espai) and Fundación Vodafone España to make this work possible.

I need to thank as well my roommates, Laura and Cristina, for making my life in Boston easier, more interesting and more enjoyable. I have felt like within a little family with you, I would always be grateful for the great moments we have shared listening to each other. When I felt lonely, your company has been simply wonderful. Thanks to Marta for these great talks and listening to me when I needed to. Amazing talks and laughes that I will never forget and I will carry always with me. It was always a pleasure to talk to you, being listened and to listen. Jordi has been like another roommate and I have also really enjoyed his company, his jokes and his way of understanding life. He was one more of this little family. I really appreciate as well Patri and Josep Miquel's help when I arrived here, everything was a lot easier. It has been a great experience. Thank you all.

A very special gratitude to my mother and my father, who have always been there showing their support and their never ending love. Their good advise and opinion has always been a reference in my life and I appreciate their tireless support thinking always what would be best for me. I will never be capable to thank you enough for everything you have given me. Thank you very much Ariadna for being my best friend and best sister ever. Thank you for still being there, next to me, and for your continuous love and trust during these two difficult years away from home. You have always been a very special person in my life and you will always be.

Last but not least, a very special thank for my girlfriend, Andrea, who has been very comprehensive and very supportive during all this period despite being so far apart. Her love has given me the strength to pursue this journey and her words have helped me to appreciate what really makes life so wonderful. Thank you for being who you are. Thank you for believing in the power of dreams.

Contents

Abstract **3**

Acknowledgements **5**

List of Figures **11**

List of Tables **13**

Nomenclature **15**

1 Introduction **17**
1.1 Motivation . . . 17
1.2 Literature Review . . . 18
1.3 SPHERES testbed . . . 20
1.3.1 Testbed overview . . . 20
1.4 Thesis Objectives . . . 23
1.5 Thesis Outline . . . 24

2 Distributed Telescopes in Space: Interferometry **25**
2.1 Fundamentals of Interferometry . . . 25
2.2 Types of Space interferometers . . . 27
2.2.1 Existing and future missions . . . 29
2.3 Imaging objectives and scientific goals . . . 30
2.3.1 Formation-flying maneuvers . . . 31
2.3.2 Imaging reconfiguration maneuvers . . . 31
2.4 Summary . . . 32

3 Spiral expansion maneuvers **33**
3.1 Interest of spiral maneuvers . . . 33
3.1.1 Stop and Stare and Drift Through maneuvers . . . 33
3.1.2 Minimum-fuel problem with image constraints . . . 34
3.1.3 UV plane coverage . . . 34
3.2 Design of spiral trajectories . . . 38
3.2.1 Analysis of spirals dynamics . . . 38
3.2.2 Design process for Stop and Stare spirals . . . 39

3.2.3 Design process for Continuous and Drift Through spirals . . . 39
3.3 Implementation on SPHERES . . . 43
3.3.1 Matlab simulation . . . 43
3.3.2 MIT 2D air table results . . . 45
3.3.3 International Space Station planned tests . . . 46
3.4 Summary . . . 46

4 Optimal Imaging Controllers 49
4.1 Optimal Control Problem - Variational Approach . . . 50
4.1.1 Necessary Conditions . . . 52
4.1.2 Boundary Conditions . . . 52
4.2 Linear Quadratic Problems - LQ formulation . . . 53
4.2.1 Dynamics linearization . . . 53
4.2.2 Quadratic cost function . . . 53
4.2.3 LQ controller . . . 54
4.2.4 Numerical solution . . . 55
4.3 Incremental Controller . . . 56
4.3.1 Controller objective . . . 56
4.3.2 Image metrics . . . 56
4.3.3 Cost function and terminal cost . . . 57
4.3.4 Optimization problem resolution . . . 58
4.3.5 Incremental Controller calculation algorithm . . . 60
4.3.6 Simulation results with two spacecrafts . . . 61
4.4 Position-Redefining Controller . . . 65
4.4.1 Controller objective . . . 65
4.4.2 Image metrics . . . 66
4.4.3 Cost function: Balance between image quality and fuel consumption . . . 66
4.4.4 Problem resolution . . . 67
4.4.5 Position Redefining Controller calculation algorithm . . . 67
4.4.6 Simulation results . . . 68
4.5 Summary . . . 70

5 Conclusion 73
5.1 Thesis summary and contributions . . . 73
5.2 Future work . . . 75

A Spiral optimization expressions 77
A.1 Fuel and time optimal maneuvers of the double integrator plant . . . 77
A.1.1 Time optimal maneuver of the double integrator plant . . . 78
A.1.2 Fuel optimal maneuver of the double integrator plant . . . 79
A.1.3 Combination of time-fuel optimal maneuver of the double integrator plant . . . 80
A.2 Polynomial expression of the design process . . . 82
A.3 Fuel usage expressions . . . 83
A.3.1 First phase: acceleration phase . . . 83

A.3.2 Second phase: coast phase 84
A.3.3 Third phase: deceleration phase 84
A.4 Open-loop control law expressions 84

B Optimal Imaging Controllers results **86**
B.1 Incremental Controller 86
B.2 Position Redefining Controller 89

Bibliography **93**

List of Figures

1.1 *A SPHERE satellite* 20
1.2 *CAD model of flight sphere with important external features identified. The sphere shell measures approximately 21 cm in diameter, and the vehicle wet mass is approximately 3.6 kg* . . 21

2.1 *Relation between the different functions representing an image in different domains* 26
2.2 *Diffraction pattern from a single telescope as a function of the direction θ* 26
2.3 *Schematic configuration for a two collector interferometer operating in the visible regime* . . 28

3.1 *Spiral trajectory of a two-apertures distributed telescope achieving unitary and full UV coverage: a) XY plane b) UV plane* 38
3.2 *Spiral trajectory of a three-apertures distributed telescope achieving unitary and full UV coverage: a) XY plane b) UV plane* 38
3.3 *Spiral trajectory of a two-apertures distributed telescope performing Stop and Stare observations. Straight lines are described using a bang off bang acceleration profile between locations.* 40
3.4 *Evolution of $\Upsilon(\gamma, t_f)$ for different values of t_f* 42
3.5 *Matlab simulation of the Continuous spiral maneuvers performed in different times: a) 120s b) 60s* 44
3.6 *Tests on the MIT air table: a) Continuous spiral b) Stop and Stare spiral c) Drift Through spiral* 47

4.1 *First two steps performed by the optimal controller with low r/a ratio: a) XY plane (first step) b) UV plane (first step) c) XY plane (second step) d) UV plane (second step)* 63
4.2 *Steps 3 and 4 performed by the optimal controller with low r/a ratio: a) XY plane (third step) b) UV plane (third step) c) XY plane (fourth step) d) UV plane (fourth step)* 64
4.4 *Performance of the Incremental Controller for different values of ratio r/a: a) Image metrics comparison b) Energy comparison* 64
4.3 *First two steps performed by the optimal controller with high r/a ratio: a) XY plane (first step) b) UV plane (first step) c) XY plane (second step) d) UV plane (second step)* 65
4.5 *Repositioning of a 4 satellites formation with low r/a ratio : a) XY plane b) UV plane* . . . 69
4.6 *Repositioning of a 4 satellites formation with high r/a ratio : a) XY plane b) UV plane* . . . 69
4.7 *Performance of the repositioning controller: a) low r/a ratio b) high r/a ratio* 71

5.1 *ESA's Darwin mission for the quest of extrasolar planets* 73

A.1 *Illustration of the switch curve for the double integrator plant* 79

A.2 *The switch curve and the $x_2 = 0$ axis divide the state space into four sets* 80
A.3 *The switch curve and the Γ_k curve divide the state space into four sets* 82
A.4 *Representation of: a) $\Upsilon(\gamma, t_f)$ and b) $\frac{d\Upsilon(\gamma,t_f)}{d\gamma}$ for different values of t_f.* 83

B.1 *First two steps performed by the optimal controller with low r/a ratio: a) XY plane (first step) b) UV plane (first step) c) XY plane (second step) d) UV plane (second step)* 86
B.2 *Steps 3, 4, 5 and 6 performed by the optimal controller with low r/a ratio: a) XY plane (third step) b) UV plane (third step) c) XY plane (fourth step) d) UV plane (fourth step) e) XY plane (fifth step) f) UV plane (fifth step) g) XY plane (sixth step) h) UV plane (sixth step)* . 87
B.3 *First four steps performed by the optimal controller with high r/a ratio: a) XY plane (first step) b) UV plane (first step) c) XY plane (second step) d) UV plane (second step) e) XY plane (third step) f) UV plane (third step) g) XY plane (fourth step) h) UV plane (fourth step)* 88
B.4 *Steps 5 and 6 performed by the optimal controller with high r/a ratio: a) XY plane (fifth step) b) UV plane (fifth step) c) XY plane (sixth step) d) UV plane (sixth step)* 89
B.5 *Repositioning of a 2 satellites formation with low r/a ratio : a) XY plane b) UV plane* . . . 89
B.6 *Repositioning of a 3 satellites formation with low r/a ratio : a) XY plane b) UV plane* . . . 90
B.7 *Repositioning of a 4 satellites formation with low r/a ratio : a) XY plane b) UV plane* . . . 90
B.8 *Repositioning of a 5 satellites formation with low r/a ratio : a) XY plane b) UV plane* . . . 90
B.9 *Repositioning of a 2 satellites formation with high r/a ratio : a) XY plane b) UV plane* . . . 91
B.10 *Repositioning of a 3 satellites formation with high r/a ratio : a) XY plane b) UV plane* . . . 91
B.11 *Repositioning of a 4 satellites formation with high r/a ratio : a) XY plane b) UV plane* . . . 91
B.12 *Repositioning of a 5 satellites formation with high r/a ratio : a) XY plane b) UV plane* . . . 92

List of Tables

3.1 *Optimization parameters for spiral maneuvers* 43
3.2 *Theoretical design parameters for the complete turn Continuous spiral maneuvers and their fuel consumption* 44
3.3 *Results of the Matlab simulation for the Continuous maneuvers of 120s, and 60s* 44
3.4 *Comparison of Stop and Stare and Drift Through maneuvers. Results from Matlab simulation.* 45
3.5 *Comparison of the Continuous maneuver, the Stop and Stare one and the Drift Through one on the MIT table with the real Spheres testbed* 46

4.1 *Image metrics evolution along the Incremental Controller reconfigurations. Units of this image metrics comparable to MSE* $(W/m^2)^2$ 63
4.2 *Results of the statistical analysis for SI mission for a low* r/a *ratio* 70
4.3 *Results of the statistical analysis for SI mission for a high* r/a *ratio* 70

Nomenclature

N_s	Number of spacecrafts
m	Mass of each spacecraft
a_r	Radial acceleration
a_θ	Transversal acceleration
Γ	Thrust
μ	Fuel rate
$\overrightarrow{r}$	Position vector
x	X position of the spacecraft
y	Y position of the spacecraft
$\boldsymbol{x}$	Total state of the spacecraft
θ	Orientation angle
λ	Wavelength of the light observed
D	Diameter of the aperture
B	Baseline, distance between two apertures
LOS	Line-of-sight
A	Autocorrelation of one aperture
I	Intensity function
J_1	Bessel function, first kind, order one
UV point	Spatial frequency information
u	U-component of the UV point
v	V-component of the UV point
α	Angular acceleration
t_f	Final maneuver time
t_a	Thrusting time
γ	Fraction of the total time corresponding to thrust
Υ	Polynomial expressions concerning the spiral optimization
J	Cost function
J_{aug}	Augmented cost function
I	Intensity function
H	Hamiltonian
ψ	Co-state
$\boldsymbol{u}$	Control effort
h	Final cost

Chapter 1

Introduction

1.1 Motivation

The scientific community and all different space agencies have recently initiated different programs to roadmap future space astronomy and astrophysics for the future years. Among these programs, the National Aeronautics and Space Administration (NASA) has defined the Origins Program. The purpose of this program, and the analog ones from other agencies, is to help answer fundamental question regarding the origins of life and the universe such as:

- How did the first galaxies form?
- How do stars and planetary systems form?
- Are there any planets outside our solar system that are capable of sustaining life?
- How did life originate on Earth?
- Is there life (however primitive or evolved) outside our solar system?

Even though it is not possible to go back in time to determine how the galaxy was formed, one can observe how new interstellar objects are formed through the use of telescopes. Similarly, the existence of life sustaining planets outside this solar system may also be determined by direct observation. In short, the Origins Program attempts to answer the above fundamental questions through the collection of direct observational evidence [1], [2].

Before the initiation of the Origins Program, terrestrial telescopes have been used to look at distant astronomical objects. Unfortunately, due to atmospheric disturbances and physical constraints, there exists a limit at which these astronomical objects can be resolved. To overcome the atmospheric disturbances, the Hubble Space Telescope was then developed [3], and has been in operation in Low Earth Orbit (LEO) since 1990. This telescope, which operates in the visible to infrared regime, can provide resolutions up to ten times better than any ground-based telescope with its 2.4 m reflecting aperture. There is, however, a limitation to the size that these telescopes can be launched as they have to fit within the shroud of a launch vehicle.

The physical limitation, however, is overcome through the use of distributed structures, where a telescope would be constituted of different spacecraft that would perform as an space-based interferometer and will fly in formation. The potential benefits that can be reaped from a distributed

satellite system have led to the proposal of several multi-spacecraft missions, such as NASA's Terrestrial Planet Finder (TPF) [4], the ESA's Darwin [5] or the NASA's Stellar Imager missions [6], [7], [8]. This distributed concept may offer significant improvements in the overall system's reliability, angular resolution and reconfigurability when compared to their single monolith counterpart. With inherent redundancies added through the use of multi-spacecraft systems, failure of a spacecraft in a large constellation does not automatically cripple the entire system. Angular resolutions that are not possible with a single monolith, can now be easily achieved with the use of smaller spacecraft placed far apart. Last, but not least, the capability to reconfigure the array to meet the changes in mission requirements make these multi-spacecraft systems much more desirable.

In general, the capability of an interferometer to produce high quality images is dependent upon the locations of the apertures. Terrestrial arrays can be placed in any pattern conceivable, and in this pattern they will remain. Hence, given a certain number of apertures, only interferometric measurements at the baseline separations defined by the locations of the apertures can be obtained. These terrestrial arrays do not allow additional baseline measurements to be taken as the apertures have very limited maneuverability, but, the array rotates on the sky due to Earth's rotation, which provides additional baselines.

Arrays that are placed in space, however, may be maneuvered by the use of propulsion units. Given that a certain number of different baseline measurements are made using a specified number of apertures, it exists a tradeoff between adding more apertures into the system or using more propellant to maneuver the fewer number of apertures such that measurements at all the required baseline separations are obtained. This tradeoff can be carried out only if the propellant resources required for the limited number of apertures are determined. In order to maximize the science returns, the purpose of this study is to determine optimal imaging maneuvers and reconfigurations for separated spacecraft interferometers operating in free space.

1.2 Literature Review

The development of new missions constituting distributed telescopes is dependent on the evolution of different technology capabilities, among these important aspects there is the necessity of developing accurate and precise formation flying algorithms. Review of literature reveals that different control strategies could be affronted for formation flying missions. The main techniques are [9], [10]:

- Consideration of the whole formation like a MIMO plant (Multiple Input Multiple Output).
- Leader-follower structure.
- Virtual structure, where all satellites are positioned with respect to a virtual point.

Besides, all authors confirm that staged control actuators will be the best strategy to follow, where a first coarse formation is established (with actuators of low precision but wide range) and then followed by more accurate and precise actuators, with a narrower range of actuation.

At the Space Systems Laboratory, a considerable amount of publications refer to the realization and implementation of different formation flying maneuvers on their testbed. This research have the objective of maturation of techniques to develop formation flying algorithms, coordinate different spacecraft and defining how should they interact interact between them (communications). The fact

of implementing them in the real SPHERES testbed gives the possibility to the scientist to test in a real environment how these algorithms behave. The main results of the formation flying research realized at MIT is presented in different publications showing the design of the algorithms, their performance in space, their precision and the future work to be done [11], [12], [13].

Furthermore, an extensive literature review has been realized on the subject of implementation of formation flying algorithms for the SPHERES testbed at MIT and as well for the International Space Station, which was a key aspect of this actual research. The most important references related to this topic are Dr. Alvar Saenz-Otero thesis [14], [15], Mark Hilstad thesis [16] and Dr. Simon Nolet thesis [17] thesis, concerning the theoretical development of the testbed and some internal documents showing how to interact with the software architecture and code new algorithms [18], [19].

On the other hand, an extensive literature review has been considered necessary concerning the work realized by the Jet Propulsion Laboratory (California Institute of Technology) about the design and conception of formation flying rotations because they represent one important set of maneuvers to reconfigure the imaging configuration of the spacecraft flotilla. These maneuvers have been differentiated in two groups: constrained rotations (when the satellites should follow a determined trajectory) or unconstrained rotations (where the most important fact is the final configuration). The main references consulted for this topic are done by Fred Hadaegh [20], [21], [22]. Furthermore, considering that the realization of this kind of maneuvers have as the main objective the achievement of a determined position with the minimum fuel usage, the scientific community has developed different fuel saving strategies [23]. Most of the times design of optimal controllers is the adopted solution, therefore two optimal control books [24], [25] have also been an important reference in this thesis.

Finally, another key aspect for the development of distributed telescopes is the necessity of studying the best optical configurations of the space based interferometers. Numerous interferometric studies have been carried out to determine which types of interferometer are suitable for each space mission to best accomplish their optical requirements. Most of authors coincide that taking into account their performances and the present technology to implement them, two main types of interferometers are on the stage for future space-based missions. These two are the Michelson Interferometer and the Fizeau Interferometer. The first one has shorter baseline between spacecrafts and is suitable to observe steady targets, with the necessity to take more than one unique measurement and the latter is adapted to the observation of rapidly changing targets, like Earth observation or star dynamics study [26], [27], [28], [29], [30], [31]. Review of technical literature about current missions confirms this fact because Terrestrial Planet Finder is designed with a nulling Michelson Interferometer [4] and the Stellar Imager Mission design considers a Fizeau type [6], [7].

Once the type of interferometer is decided, a profound study is performed concerning the optimal imaging configurations of the spacecraft to obtain best image quality. Fundamentals of interferometry have been reviewed in optics books [32] but special attention has been conducted in reviewing publications concerning imaging configurations and image metrics to evaluate telescope's performance, because the obtention of a mathematical expression representing the quality of one measurement gives the possibility of incorporating this performance in the design of controllers and optimal trajectories. Non-redundant configurations like Golay [33], Cornwell [34] and Golomb [35], where the measurement of determined spatial frequencies are only taken once to better the system

efficiency and to avoid speckle noise difficulties, are the configurations most accepted among the scientist community. Extensive studies have been performed as well by Dr. Edmund Kong in his both thesis presented at MIT [36], [37]), where specific image metrics and imaging configurations are discussed.

The research performed in this present thesis concerns the development of new imaging maneuvers and their correspondent optimal imaging controllers to fulfill new formation flying requirements to realize synthetic imaging with the less fuel consumption as possible.

1.3 SPHERES testbed

1.3.1 Testbed overview

The SPHERES (Synchronized Position Hold, Engage, Reorient Experimental Satellites) testbed provides a fault-tolerant development and verification environment for high-risk formation-flying, rendezvous, docking, and autonomy algorithms. The testbed is designed to test algorithms that may be used in future space missions; consequently, each individual sphere is designed to mimic the functionality of a true satellite [16], [18], [19].

Figure 1.1: *A SPHERE satellite*

The testbed is operated inside the station by NASA astronauts. Six degree-of-freedom (DOF) operations on the ISS are complemented by a 3 DOF low-friction air table facility in the Space Systems Laboratory (SSL) at MIT. The SPHERES separated spacecraft testbed provides investigators with a long-term, replenishable, and upgradeable platform for the validation of high-risk metrology, control, and autonomy technologies. These technologies are critical to the operation of distributed spacecraft and docking missions such as Terrestrial Planet Finder and Stellar Imager. The SPHERES testbed consists of three free-flyer vehicles (commonly referred to as "satellite" or "spheres"), five ultrasonic beacons, and a laptop control station. The satellites are self-contained, with onboard power, propulsion, communications, sensor, and computer subsystems. They operate semiautonomously, requiring human interaction primarily for replenishment of consumables and to command the beginning of each test. An external view of the sphere design, showing thrusters, ultrasonic sensors, propellant tank, and pressure system regulator knob, is given in figure 1.1.

SPHERES subsystems

The elements of the satellite hardware and software are organized by subsystems representative of those on real spacecraft. The avionics, communications, propulsion, control, and state estimation subsystems are directly relevant to the ability of the spheres to perform coordinated maneuvers. A CAD model of an individual flight sphere with key external features identified is shown in figure 1.2. The following list summarizes key features of the testbed, from an end-user point of view:

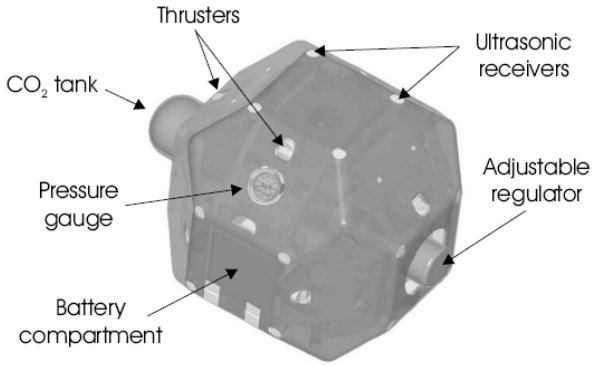

Figure 1.2: *CAD model of flight sphere with important external features identified. The sphere shell measures approximately 21 cm in diameter, and the vehicle wet mass is approximately 3.6 kg*

- The flight software is written in C, and runs on a Texas Instruments C6701 DSP at 167 MHz.
- Analog sensors are sampled and digitized by an FPGA at 12-bit resolution.
- The communications subsystem consists of two independent radio frequency channels. The sphere-to-sphere (STS) channel is used for communication between the spheres, enabling co-operative and coordinated maneuvers. The sphere-to-laptop (STL) channel is used to send command and telemetry data between the spheres and the laptop control station. The design and implementation of the SPHERES communications subsystem is described in detail by Dr. Saenz-Otero [14], [15].
- The propulsion subsystem hardware consists of twelve cold-gas thrusters, a tank containing liquid CO_2 propellant, and the regulator, piping, manifolds, and valves required to connect the tank to the thrusters. The propulsion hardware is serviced by flight software running in a dedicated high-frequency timed interrupt process. Thruster forces are fixed, but pulse modulation to a time resolution of one millisecond can be used to produce effectively variable forces.
- The position and attitude determination system (PADS) has both inertial and external sensors. Gyroscopes and accelerometers are available for rapid updates to the state estimate over short time periods, and ultrasonic time of flight range measurements from wall-mounted beacons

to the sphere surfaces are used to update the state estimate with respect to the laboratory reference frame. It provides real-time position, velocity, attitude, and angular rate information to each sphere

- The control subsystem is serviced by flight software running in a dedicated timed-interrupt process. The control subsystem produces thruster on-time commands based on a specified maneuver profile, a control law, and the thruster geometry and actuation properties. The typical control architecture that is implemented in the type of missions that the SPHERES testbed tries to emulate consists on a graduated scale of modules organized by level of autonomy. First of all, with the less level of autonomy, we find the GN&C modules (Guidance,Navigation and Control), which takes the information of the spacecraft sensors and using their GN&C modes and their actuators assures the stability of the spaceship, but no autonomous decision are made in this module. The next module consists on the automatic MVM (Mission & Vehicle Management) which is in charge of planning the mission and the tasks of the spacecraft in an autonomous way. This module gives the appropriate references to follow to the GN&C modules. At the same time, the MVM module is in constant communication with the FDIR module (Fault Detection, Isolation & Recovery System) that will supervise autonomously the state of all subsystems in the spacecraft, will detect possible failures, and eventually will try to isolate them and recover the spacecraft from them. Finally, the last loop could be composed by the human operator, who is in charge of the remote monitoring and eventually can proportionate priority commands.

- An event-driven background task is available to complement and augment traditional estimation and control processes. The combination of the task process with the estimation and control processes allows scientists significant freedom in algorithm design.

SPHERES operations

The SPHERES testbed provides the possibility of realizing high-risk formation-flying tests with a fault-tolerant development and verification environment. Despite being a fault-tolerant development process, standard research procedures have been defined in order to accelerate the iterative research process and succeed with most of the experiments sent to the International Space Station laboratory, which is the real verification location of the testbed.

The SPHERES testbed has a Matlab simulation created by the first Graduate Students working within the project that simulates the behavior of the SPHERES in the ISS environment. In this Matlab simulation, the satellites dynamics, the testbed metrology, the position and attitude determination system and the communication system has been coded taking into account all the testbed characteristics. Therefore, all designing processes begin with the implementation of new algorithms within this simulation, because it permits the behavioral analysis of the algorithm and the visualization of the most important data evolving during the test. As a consequence, this simulation characterizes the first and unavoidable step of the implementation process. Firsts implementation errors and debugging can be solved on computer, what makes the first iterative research step faster and cheaper.

Once the Matlab simulation is fully working and algorithms are validated, the scientist may start the coding process on the real SPHERES platform. The implementation of the algorithm in

the Spheres platform should be followed by a first test phase on the air table at the SSL Laboratory at MIT. On this table, where the satellites are floated by a thin air layer, a 3 degrees-of-freedom environment is created where only maneuvers in 2D can be performed. This environment is slightly perturbed by the calibration of the table (gravitational effects), by imperfections on the floating system or by scratches on the glass table. However, this first testing phase gives a very accurate idea about the correctness of the algorithm in order to evaluate if it represents a potential test to be sent to the International Space Station. Within this phase, the code should be verified to assure that the test is running properly until the end of the execution and that the satellites are behaving as expected (firing in the right direction, performing the moves expected and etc). All this beforehand verification helps to increase the science output of the tests performed in the International Space Station.

Finally, the last step of the procedure represents the realization of the test by the astronaut in charge of the Voluntary Science at ISS. In order to facilitate the realization of the test, the MIT scientist should specify the experiment's basic procedures to inform the astronaut how to position the satellites, how to execute the test and what to expect from this test. Once the test is performed, MIT scientists should analyze data obtained from the test, and his/her conclusions will lead to the next step of the iterative research process.

1.4 Thesis Objectives

The primary objective of this study is the design of optimal imaging maneuvers for a separated spacecraft interferometer to successfully carry out a synthetic imaging mission. This optimal imaging maneuvers should take into account the image quality of the image measured but at the same time must be designed to consume the less resources as possible, because those are scarce on every space mission and represent one of the aspects that most increase their resulting total cost.

This objectives will be achieved from two different approaches throughout this thesis. The first one will consist on the optimization of a constrained trajectory, where the satellites should follow a determined trajectory consuming the minimum energy. In this kind of optimization, no image metrics is used because the type of trajectory is already designed to fulfill the optical requirement. Spiral trajectories will be those trajectories under study in the first part of the thesis. Once this optimization is performed, designed trajectories are implemented on the SPHERES spacecraft in order to prove their optimal behavior in real conditions. Thus, full interaction with SPHERES testbed has been necessary. First of all, computer based simulations on Matlab, followed by the implementation on the MIT table and finally with the real test in space, onboard the International Space Station.

A different approach is followed on the second part of the thesis where optimal imaging controllers are designed. These controllers compute trajectories that minimize energy consumptions and at the same time contribute to the maximization of an image metrics that represent the image quality of the observations. The definition of these optical metrics is the first step in order to define the optimal controllers because they evaluate the benefices of positioning the different spacecrafts in determined positions with the objective of having the best spatial frequency samples of the image (UV points). The combination of an image metrics and energy metrics in the same controller lead to the resolution of an LQR problem, considering the spacecraft flying in free space. Within

this optimal control problem, two type of controllers are designed: the first one computes the best reconfiguration to do when the number of total reconfigurations is unknown and the second one reconfigures the formation considering the non-noise-free nature of any space-based mission.

1.5 Thesis Outline

From the list of the primary objectives, this study can be broken down into two major sections, the determination and implementation of optimal spiral maneuvers and design and realization of optimal imaging controllers, combining image and energy metrics.

These both main topics are highly related to the fundamentals of space-based interferometry, because every of these imaging maneuvers implemented on distributed space telescopes have as their main objective the realization of precise interferometric measurements. As a consequence, in chapter 2 the fundamentals of interferometry are introduced as well as the main types of interferometers used in the main current and future interferometric missions. Finally, a brief explanation of the necessities of imaging maneuvers are discussed.

Spiral maneuvers optimizations are treated throughout chapter 3, where a first phase about the interest of spiral maneuvers is presented and followed by the design of these type of maneuvers, trying to minimize their fuel consumption. Furthermore, these maneuvers are adapted to the SPHERES testbed and of course implemented onboard the flight software. Simulation results and real results on MIT table are presented proving the possibility of implementing this kind of coordinated maneuvers in space conditions.

In chapter 4 design of optimal imaging controllers is discussed. First of all the interest of these controllers is presented, secondly the optimal control problem is stated and specified for these kind of applications. The presentation of the LQ framework used in this thesis is discussed in the next section, suitable for problems using linear dynamics (in this case free space dynamics) and quadratic cost functions (energy consumption). Finally, this framework is applied to both type of controllers desired. The first one for the incremental controller and the second one for the repositioning controller, showing results of their performance and applicability in real space missions.

The final chapter of conclusions summarizes the main contributions of the present thesis, highlighting the most important results contributing to the synthetic imaging formation flight technologies. Possible future work concerning imaging interferometric maneuvers is proposed in the future work section in order to keep on improving the different ways in which a separated spacecraft interferometer can be most efficiently utilized.

Chapter 2

Distributed Telescopes in Space: Interferometry

2.1 Fundamentals of Interferometry

The performances in a space observation system could be evaluated by three factors [32]:

- **Angular resolution:** predicts how crisply an optical system is able to resolve an observing target. The smaller the angular resolution is, the more graphical features a telescope system can extract from an image.
- **Sensitivity:** the minimum amount of photons that the system should receive in order to have a satisfying signal to noise ratio.
- **Ambiguity:** consists on the capacity of the system of concentrating its observation power in one direction (directivity, suppression of sidelobes).

A single telescope with a single aperture is limited by diffraction [38]. Diffraction is normally taken to refer to various phenomena which occur when a wave encounters an obstacle. It is described as the apparent bending of waves around small obstacles and the spreading out of waves past small openings. This fact will be as well a limiting factor in an interferometric system, but combination of light from different sources permits overcoming these penalties and obtaining a better system than the monolithic configuration. In case of a one dimensional aperture, the amplitude is calculated as a Fourier Transform of a pupil function as indicated in equation 2.1. In figure 2.1, different relationships between the different main functions to represent images mathematically in spatial and frequency domain are presented.

$$A_{one}(\theta) = \int_{-D/2}^{D/2} e^{i(2\pi x\theta/\lambda)} dx = \frac{\sin(\pi\theta D/\lambda)}{\pi\theta D/\lambda} D \tag{2.1}$$

The measured intensity I is the squared magnitude of the amplitude,

$$I_{one}(\theta) = \left[\frac{\sin(\pi\theta D/\lambda)}{\pi\theta D/\lambda}\right]^2 D^2 \tag{2.2}$$

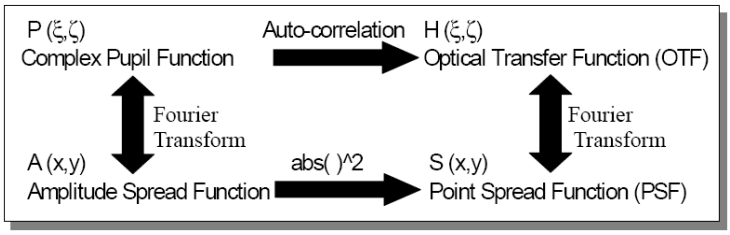

Figure 2.1: *Relation between the different functions representing an image in different domains*

For a two dimensional aperture, the sine function in the last equation is replaced by a Bessel function of the first kind, order one, a J_1, which leads to this equation:

$$I_{one}(\theta) = \Big[\frac{2J_1(\pi\theta D/\lambda)}{\pi\theta D/\lambda}\Big]^2 D^2 \tag{2.3}$$

which is plotted in figure 2.2 in thick trace, and has the first null point at 1.22, what gives the angular resolution $\theta_r = 1.22\lambda/D$, known as the Rayleigh angular resolution and it represents a limiting factor in every optical system [38], [39].

From the previous discussion, in order to evaluate the advantages of light combination (interferometry), one aperture one can be added to the same analysis. Interfering light from two apertures separated a distance length of B (baseline) would create a two telescope interferometer. For this case, the result of the intensity is the one that follows and is plotted also in figure 2.2 with thinner trace.

$$I_{two}(\theta) = 2I_{one}(\theta)[1 + \cos(2\pi\theta B/\lambda)] \tag{2.4}$$

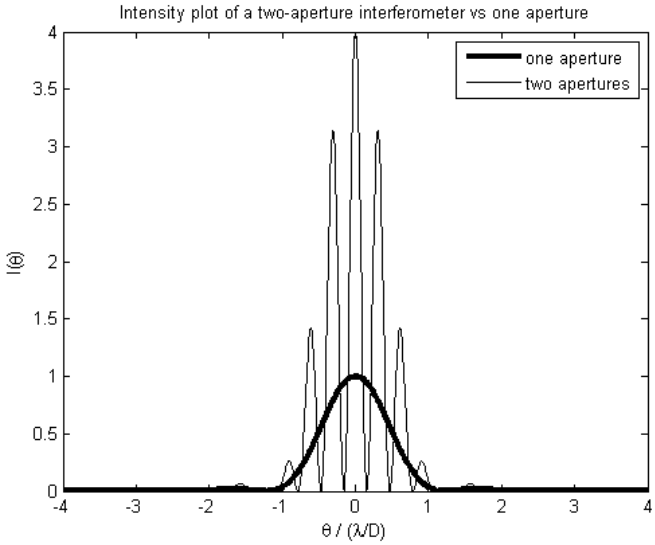

Figure 2.2: *Diffraction pattern from a single telescope as a function of the direction θ*

It is observed that the peak intensity of a two aperture interferometer is four times higher than that of the one aperture diffraction pattern (thick trace). It is worth mentioning as well that the

broad envelope of the interference pattern of two apertures is produced by a single aperture whereas the rapidly oscillating interference pattern depends on the baseline length, B. This behavior is the result of the interference of the two sources of light. Depending on the distance between these two sources interfered and the wavelength observed, constructive and destructive interference are produced. This allows the system to have bigger intensity due to the fact of the constructive scenario and better angular resolution because a destructive interference creates a zero closer to the origin in the intensity pattern. These are the two key aspects that make interferometry so interesting for space missions. Besides, configuring an space mission as a distributed system, gives the possibility of creating a system that is more fault tolerant, more flexible, more reconfigurable and with a lower total cost.

2.2 Types of Space interferometers

Due to the improved angular resolution obtainable using an interferometer, many astronomical missions are turning towards the use of multiple aperture systems. The signals received at the interferometer's apertures are combined to provide the angular resolution that is equivalent to that of a single aperture that has a diameter roughly equal to the separation distance between the interferometer's apertures. In this subsection, a brief overview of the two interferometers that are commonly being used to image astronomical objects is presented. These two interferometers are the Michelson and Fizeau interferometers.

The Michelson interferometer is the most commonly used interferometer among the two. Some of the missions that have been proposed to operate in this interferometer mode are the Space Interferometer Mission (SIM) [40] or the Terrestrial Planet Finder (TPF) [4] and Darwin [5] (used in the nulling mode). Irrespective of whether the interferometer is operating in the radio or visible regime, signals collected at the collector apertures must be combined at a single location to provide a single data point. In radio interferometry, signals from the different apertures are normally recorded and correlated at a later time because it exists sufficient computation speed to sample these signal satisfying Shannon principle. The output of the correlation is a single complex value, which gives the magnitude and phase of the image's spatial Fourier component associated with the separation between the apertures projected normal to the line-of-sight (LOS) to the target. However, in the visible regime, the science light collected at the apertures must be combined in real time since its phase cannot be recorded because there is no existing detector with a high enough sampling rate. This combined light is then focused onto a single-pixel, photon counting detector to detect its intensity. Figure 2.3 shows an scheme of an interferometer operating in the visible regime. The optical delay line is required to allow the combiner to interfere the same wavefront originating from the target and thereby create a coherent fringe.

The interferometric measurement described in the previous paragraph is only for one baseline separation. In Fourier space, this baseline separation is normally known as the UV point, given by:

$$\begin{aligned} u &= \pm\frac{x_1-x_2}{\lambda} \\ v &= \pm\frac{y_1-y_2}{\lambda} \end{aligned} \tag{2.5}$$

where (x_i, y_i) are the coordinates of the i-th aperture. The variables u and v correspond to spatial wave numbers (frequencies) of intensity variation across the image. It is worth mentioning, that

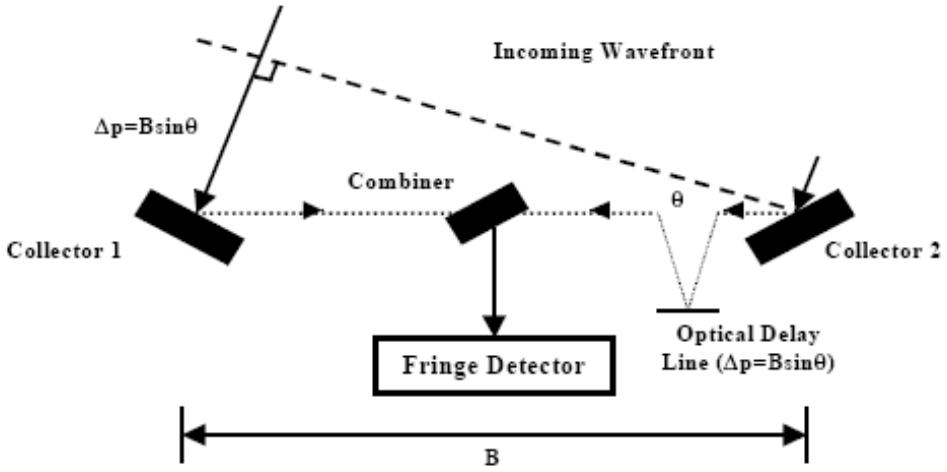

Figure 2.3: *Schematic configuration for a two collector interferometer operating in the visible regime*

the frequency samples by the interferometric system will depend on the relative distances between each pair of spacecrafts and their relative orientation. Furthermore, if the number of spacecrafts that constitute the system is known, $N_s(N_s-1)$ number of UV points will be obtained, what corresponds to the number of baselines multiplied by two (each UV point and its image, rotated 180°).

In order to obtain good interferometric images, different measurements must be taken at different UV points to obtain multiple Fourier terms in the image. This can be done by either moving the collector spacecraft (for space-based systems) or for ground-based apertures, the UV coverage of the system may be swept out through the Earth's rotation. Once all the necessary measurements are made, the visibility map, which consists of all the interferometric measurements at the different baseline separations, is inverted to give the brightness image of the source. This inversion is performed by taking the inverse Fourier transform of the visibility map, as it is explained in figure 2.1.

As it has been mentioned before, the angular extent of an object which an interferometer can resolve from its neighbor is known as the angular resolution. For a Michelson interferometer, the angular resolution is given by:

$$\theta_r = \frac{\lambda}{Bcos(\theta)} \tag{2.6}$$

where $B\cos(\theta)$ is separation between the apertures projected normal to the LOS and λ is the target's wavelength of interest, also measured in units of length. Since angular resolution improves with the separation of the apertures, most of the astronomical missions have proposed to adopt the Michelson interferometer. In general, the separation between the apertures is much larger than the size of the apertures themselves [26], [27].

An underlying assumption that is made in using an interferometer that makes sequential baseline measurements is that the states of the target remain constant throughout the imaging process. This is usually a reasonable assumption for imaging astronomical objects. However, in order to image a rapidly changing target, such as a terrestrial target, instantaneous imaging is required. Instantaneous

imaging of a target is possible if a Fizeau interferometer is used [28], [29].

Designed to operate in the visible spectrum, the Fizeau interferometer is essentially like a conventional telescope where small segments of apertures make up parts of a virtual primary mirror such that they have UV coverage that is equivalent to that of a filled aperture. As in the Michelson interferometer, the science light path lengths from the target to the combiner through the collector apertures must remain the same. However, the combined light is brought to focus onto a multichannel detector to obtain the image. The Fizeau interferometer is used for wide field astrometry as it offers a very much wider field-of-view but poorer angular resolution than a Michelson interferometer. For observation of rapidly changing targets, like stars internal dynamics, this interferometer can be designed to give full instantaneous UV coverage, as it is planned for the Stellar Imager mission [6], [7], [8], where time varying phenomena is intended to be observed.

2.2.1 Existing and future missions

Most of the missions that are nowadays performing interferometry are ground-based missions because the level of readiness of the formation flying technology to perform good interferometric space based observations is not yet good enough. Nevertheless, the experience obtained from the ground missions and the numerous studies performed in different research laboratories will make good space distributed interferometric observations possible very soon in the future.

Ground-based missions

Among the most important ground-based interferometers there are [41]:

- **The Palomar Testbed Interferometer**: It is a Michelson Interferometer operating in the infrared regime and it represents a testbed for Keck and SIM (Space Interferometry Mission). Located in San Diego County [42].
- **The Keck Interferometer**: It is a Michelson Interferometer operating in the infrared regime with two 10 m Keck Telescopes and four 1.8 m outriggers. It uses a baseline of 85m. Located in Hawaii [43].
- **Large Binocular Telescope Interferometer**: It is constituted of two separate 8.4 meter mirrors working in the infrared regime. Michelson Interferometer operating in nulling mode. Located in Arizona [44].
- **Multiple Mirror Telescope**: This telescope operates in mode Fizeau in the visible and infrared regime, using 36 hexagonal segments that constitute a 10m overall aperture. Located as well in Hawaii [45].
- **Very Large Array (VLA)**: Operated in the radio regime. It consists on 27 independent antennas, each of which has a dish diameter of 25 meters. Located in New Mexico [46].
- **Multi-Element Radio Linked Interferometer Network (MERLIN)**: Interferometer with a longest baseline of 217km. Obviously it operated only in the radio regime. Located across England and Wales [47].

Space-based missions

Concerning the future distributed space-based interferometers, the most important and representative future missions are:

- **Space Interferometry Mission (SIM)**: This space mission will be used as a Michelson Interferometer with a baseline of 7.2m. Launching date will not be earliest that 2015-2016. Objective: detection of extrasolar planets [40].
- **Terrestrial Planet Finder (TPF)**: This mission will consist on four 4-meter-class mid-infrared telescopes and one combiner spacecraft to which the light from the four telescopes is relayed to be combined and detected. Michelson interferometer operating in nulling mode to cancel light from the big star and detecting nearby planets. Launching date not earlier than 2020 and final design not determined. Objective: detection of extrasolar planets and observation of stars [4].
- **Darwin**: The Darwin Mission is a proposed European Space Agency (ESA) program designed to directly detect Earth-like planets orbiting nearby stars, and search for evidence of life on these planets. 3 free-flying space telescopes (3 meters in diameter). The launch date will be at or after 2015. Objective: detection of extrasolar planets [5].
- **Stellar Imager (SI)**: A UV/Optical deep-space telescope to image stars and observe the Universe with 0.1 milliarcsec resolution. 30 free flyers positioned within a parabolic surface with a maximum baseline of 500m. Biggest formation flying mission ever envisaged. Operating as a Fizeau interferometer. Objective: enable an understanding of solar/stellar magnetic activity and its impact on the origin and continued existence of life in the Universe, the structure and evolution of stars and habitability of planets [6], [7] [8].
- **Planet Imager (PI)**: This mission would follow on from the Terrestrial Planet Finder (TPF) and produce images of Earth-like planets. It would consist on an array of 5 TPF-class optical interferometers flying in formation. Each interferometer would consist of four 8-m telescopes to collect light and null it. The five interferometers would be arranged in a parabola, creating a very long baseline of 6,000 km with the combining spacecraft at the focal point of the array. Objective: precise imaging of Earth-like planets, trying to create a 25 x 25 pixel image of each planet [48].

2.3 Imaging objectives and scientific goals

All these kind of observation missions that synthesize space-based distributed telescopes have as their main objective the maximization of the science output and the quality of this output considering the shortage of onboard resources. As a consequence, the type of maneuvers needed should be a combination of interesting maneuvers from the point of view of the scientific observation (image quality) and of minimum energy consumption.

Different missions will determine different imaging objectives or scientific goals because every type of missions will be designed for the observation of specific target, which will imply different technical requirements. For instance, the angular resolution needed for Stellar Imager, where specific

details of far-away stars should be detected, is not the same of Terrestrial Planet Finder, where the objectives are the finding of new "worlds" in other planetary systems. Astrophysicists, astronomers and optical engineers would determine the optical requirements of these missions, and as a result of these requirements, the necessary optical parameters such as angular resolution, intensity and ambiguity will be specified. Once this step would be achieved, in order to fulfill these optical necessities, the optical payload and all the interferometric equipment will be decided. At this same step, the number of spacecraft needed, their orbits (for instance L2-point) and their formation-flight precision is also agreed. After all these preliminary decisions, design of type of maneuvers will determine the amount of energy needed, the amount of propellant and lifetime of the mission. This phase of dimensioning spacecrafts and their fuel needed is critical in the engineering process, thus the maneuver design should be done very consciously.

2.3.1 Formation-flying maneuvers

Within a formation flying mission, different control phases can be differentiated [9], [10]:

- Capture of the states of satellites after their deployment.
- Acquisition of the formation.
- Maintenance of the formation and precision control.
- Reconfiguration maneuvers to take new measurement of the same target.
- Re-targeting maneuvers to observe new celestial objects.

All these phases are of different nature and their needed performance, precision and overshooting characteristics are also different, thus different control approaches should be applied to each of them.

In this thesis, research will be conducted in the design of reconfiguration maneuvers to take new measurements of the same target. Every of these reconfiguration maneuvers has as a main objective the positioning of the spacecraft in new relative configurations in order to sample new frequency information. This frequency information, as it has been explained in section 2.2, is related to the relative position between each pair of spacecrafts, therefore designing coordinated maneuvers between satellites will have a direct impact on the image information that the mission will measure, thus on the image quality.

2.3.2 Imaging reconfiguration maneuvers

Spiral maneuvers

Interesting studies have been performed in order to find continuous set of maneuvers, where spacecraft describe coordinated relative movement that permit the sampling of a big amount of frequency information. These kind of maneuvers should perform continuous changes in orientation and in distance between satellites, what gives the possibility of sampling different UV points throughout the maneuver. Spirals represent an important set with these characteristics [49], [50], [51]. The fuel-wise optimization and implementation of these type of maneuvers in real spacecraft will be an important objective of this thesis in order to fulfill some of the nowadays formation flying research objectives within the SIFFT program (Synthetic Imaging Formation Flight Testbed), supported by NASA.

Optimal Imaging maneuvers

On the other hand, considering stationary observations, several studies have been conducted by several authors in order to find configurations that result in optimal UV coverages. These configurations were first proposed by Golay [33] and Cornwell [34] for a reduced number of spacecraft and by Golomb [35] for a large number of apertures. This configurations are extremely useful for Earth based arrays, as most apertures are either stationary or have very limited maneuvering space. This limitation, however, does not apply to a separated spacecraft interferometer, as the objective of designing such a system is to allow better UV coverage by relocating the collector spacecrafts to take new interferometric measurements at various aperture baselines. These different positioning must be evaluated to know which are their effects on image quality, and in order to do so, a representative image metrics should be developed. An extensive work, concerning the definition of image metrics has been conducted by Dr. Edmund Kong [36], [37], and some of these results are used throughout this thesis. Design of controllers that take into account these image metrics and the fuel consumption of the spacecraft and balance both performances are the topic of the second part of this thesis, and their interest and performance is discussed.

2.4 Summary

This chapter presents a brief recall of the main fundamentals of interferometry and how they are related to separated spacecraft missions. At the same time, the main interferometric missions are presented clarifying that Michelson interferometer and Fizeau interferometer are the most used. The performance of these two interferometers is highly related to the placement of UV points and in the case of Fizeau interferometer also with the aperture's diameter. In this research intensive study is performed concerning the balance of the placement of these UV points and the fuel usage used. As a consequence, all analysis here realized are directly applicable for Michelson interferometers and would need an extension considering aperture diameters for Fizeau Interferometers. Finally, at the end of this chapter, interest of spiral maneuvers and optimal imaging maneuvers is introduced to justify their implementability as interferometric maneuvers.

Chapter 3

Spiral expansion maneuvers

3.1 Interest of spiral maneuvers

The scientific goal of obtaining high quality images is related to the capacity of our interferometric system to "paint" a large resolution disk with smaller coverage disks or "paintbrushes" while maintaining a minimum thickness of paint. This artistic definition describes the best manner to fill in the frequency information (UV coverage) of an interferometric observation.

When using interferometers as the Michelson one, this image quality depends on the capacity of obtaining a UV coverage as full as possible, each point of UV coverage being the information of the image in a unique spatial frequency.

As it has been explained in chapter 2, these frequency information depends on the measurement baselines of the interferometer and on the wavelength observed. When considering the possibility of using multispacecraft interferometric imaging systems, the realization of these imaging maneuvers will have direct consequences on the fuel consumption of the spacecraft and on the image quality.

Various studies have been performed to study static array configurations, nevertheless, if the problem of covering the UV plane is no longer considered as a static problem, and instead, this coverage is considered to be done within a certain period of time, enabling the different spacecraft to be moved, a new set of imaging maneuvers instead of imaging configurations could be defined. These kind of scenarios are no longer static and represent a new challenge concerning the formation trajectory design because the "design and optimization" variables are the trajectories of the constituent spacecraft.

3.1.1 Stop and Stare and Drift Through maneuvers

Interferometric maneuvers may be classified within two types of maneuvers [36], [37]:

- **Stop and Stare:** In this scenario, the distributed spacecraft telescope performs only steady observations. Therefore, all reconfigurations are done between states where all satellite's speeds are null. These maneuvers are high consuming.
- **Drift Through:** This type of maneuvers perform the interferometric measurement without stopping completely all spacecrafts and they sweep by the observation point only reducing their speed. The fact of not stopping completely the satellites causes the obtention of less consuming trajectories.

3.1.2 Minimum-fuel problem with image constraints

As it has been shown in previous studies [49], [50], [51], the imaging constraints on a multispacecraft interferometric imaging system translate into trajectory constraints on the constituent spacecraft of the system.

The process of minimum-fuel image formation could be posed as a painting problem [49] because it is analogous to the painting of a large disk (the UV coverage disk) by smaller coverage disks (frequency information of a pair of apertures). The problem could be posed as follows:

$$min_{u_{N_1}...u_{N_s}} \int_0^{T_{max}} \boldsymbol{u}^T \boldsymbol{u} dt \tag{3.1}$$

$$\text{subject to } \dot{\mathbf{X}} = f(\mathbf{X}, \boldsymbol{u}) \text{ and } \mathbf{q}(T) \geq \Delta$$

where $\mathbf{X} = \begin{bmatrix} \boldsymbol{x} \\ \boldsymbol{q} \end{bmatrix}$ and $\boldsymbol{x} = [x_1...x_{n_s}]^T$ is the state of the different spacecrafts, including the position and velocity, u is a vector containing the control acting on each individual spacecraft and the variables q_k correspond to the "paint" laid down at the frequency point ν_k and their evolution could be posed as:

$$\dot{q_k} = \sum_{n=1}^{N_s} \sum_{m=1}^{N_s} A[\nu_k - (r_m - r_n)] \tag{3.2}$$

where A is the autocorrelation function of one aperture and $(r_m - r_n)$ is the relative distance between spacecrafts.

Fortunately, the class of spiral trajectories, with a small enough spiraling rate, can satisfy these constraints and they also form the dominant set for minimum time problems [49]. Hence, the design of minimum fuel trajectories could be taken into account as an optimal scientific approach that would enable the possibility of realizing a good UV coverage (good imaging performance) within a minimum time and with low consumption of propellant.

3.1.3 UV plane coverage

The analysis realized in the previous section, in which the number of frequencies measured during our spiral imaging maneuver are considered as the result of a painting maneuver leads towards the necessity of analyzing some of the imaging parameters that will affect the resulting UV coverage.

While the different apertures will describe the spiral on the configuration plane (XY plane), the specific frequencies measured at each time will also evolve within a spiral, because they depend exclusively on the relative position between each pair of spacecraft, as it has been explained in the introductory section.

The trajectory of the UV points on the UV plane may be determined as a function of the trajectory of the apertures on the configuration plane. This "frequency" trajectory will permit drawing some new conclusions of the value of some parameters of the XY trajectory.

In previous sections, it has been stated that the UV coverage is indeed the autocorrelation of the XY positions of the different apertures. As it was posed on the image problem, the autocorrelation of spiral relatives movements leads to a trajectory in the UV plane that answers as well to the equation of the spiral. As a simple example, this calculation may be made for the two-apertures case:

$$\begin{array}{rcl} \overrightarrow{\boldsymbol{r_1}} & = & r\angle(\theta) \\ \overrightarrow{\boldsymbol{r_2}} & = & r\angle(\theta+\pi) \end{array} \tag{3.3}$$

$$\begin{array}{rcccl} \lambda u & = & x_1 - x_2 & = & 2r\cos(\theta) \\ \lambda u & = & y_1 - y_2 & = & 2r\sin(\theta) \end{array} \tag{3.4}$$

To obtain the maximum quality image, these spiral trajectory has to be designed to obtain full and unitary UV coverage, where information is obtained only once but in every spatial frequency, so then, a perfect reconstruction of the real image might be achieved with the Inverse Fourier Transform.

Unitary and Full UV coverage

Unitary UV coverage stands for the measuring situation where each of the spatial frequencies taken of the desired image are only taken once, therefore, no redundant measurements are done. This situation leads to several interesting facts [33], [34]:

- The overall efficiency of the "telescope system" is higher because every maneuver leads to obtain new information and not repeating the measurement of already obtained samples.
- With no redundant frequency, errors of two different baselines are not entwined and they can be isolated.
- With one only measure, phase error might be easily eliminated with phase knowledge and stability.
- Measuring only once each frequency enables the possibility of measuring other frequencies within the same integration time, what leads to a fuller UV coverage.

In the case of spirals, to achieve the mentioned unitary UV coverage, two conditions should be considered:

1. Taking into consideration the autocorrelation of the aperture disk, successive turns of the "frequency painting spiral" should not coincide in any frequency point.
2. While realizing the spiral, measuring interval times should be determined in order not to overlap successive snap-shots. These intervals will be varying because of the expansion of the formation.

Successive imaging passages

The first case, can be considered, taking into account the "frequency painting trajectory". The painting brush is $2D$ in diameter, where D is the diameter dimension of the collector aperture, so then the successive passage of the spiral painting trajectory on the same angular orientation, should be increased at least $2D$ in magnitude.

Particularly, results are stated for for spirals realized by a two-apertures interferometer which describe an archimedean spiral. The archimedean spiral vector position is defined as: $r(t) = (a + b\theta(t))$ where a specifies the initial distance to the coordinate center and and b is the spiraling rate,

which is defined as: $\frac{dr}{d\theta}$. As a consequence, the apertures trajectories and the UV points trajectories are respectively:

$$\begin{array}{rclcl} \overrightarrow{\boldsymbol{r}_1} & = & r\angle(\theta) & = & (a+b\theta)\angle(\theta) \\ \overrightarrow{\boldsymbol{r}_2} & = & r\angle(\theta+\pi) & = & (a+b\theta)\angle(\theta+\pi) \\ \lambda u & = & x_1 - x_2 & = & 2(a+b\theta)\cos(\theta) \\ \lambda u & = & y_1 - y_2 & = & 2(a+b\theta)\sin(\theta) \end{array} \tag{3.5}$$

So then, analyzing the evolution within the UV plane, successive passages in the same angular orientation on the UV plane occur every gap of π in θ. These passages should be spaced by $2D$, therefore the following conclusion is drawn:

$$b > \frac{2D}{2\pi} \tag{3.6}$$

For the three satellites case disposed in an equilateral triangle golay configuration, a similar conclusion could be drawn. The XY and UV trajectories for one pair of baselines are:

$$\begin{array}{rclcl} \overrightarrow{\boldsymbol{r}_1} & = & r\angle(\theta) & = & (a+b\theta)\angle(\theta) \\ \overrightarrow{\boldsymbol{r}_2} & = & r\angle(\theta+\pi) & = & (a+b\theta)\angle(\theta+2\pi/3) \\ \lambda u & = & x_1 - x_2 & = & (a+b\theta)[\frac{-3}{2}\cos(\theta) + \frac{\sqrt{3}}{2}\sin(\theta)] \\ \lambda u & = & y_1 - y_2 & = & (a+b\theta)[\frac{-\sqrt{3}}{2}\cos(\theta) + \frac{-3}{2}\sin(\theta)] \end{array} \tag{3.7}$$

In this case successive passages occur for gaps of $\frac{\pi}{3}$ because with 3 apertures, the number of baselines in the UV plane is 6 (3 and their 3 images). Taking into consideration this situation, passages every $\frac{\pi}{3}$ should be spaced $2D$, leading to equation 3.8:

$$b > \frac{4D\sqrt{3}}{2\pi} \tag{3.8}$$

Similar conditions might be stated for different spiral configurations (exponential spiral, cornu spiral, fermat's spiral and others) but the archimedean case has been chosen because is the only one conserving the spacing between passages at each turn, characteristic very interesting to proceed with a full UV coverage. This analysis could be carried out as well for different number of spacecraft. For two and three spacecrafts, the positioning considered in the previous calculus are the standard non redundant configurations (Golay [33] and Cornwell [34] configurations). The author has considered more interesting the analysis of the 2 satellites and 3 satellites formations because these two cases show clearly the physics and reasoning of the analysis and can be extended to any new and more complicated configuration. At the same time, these two cases may be implemented within the SPHERES testbed.

Successive imaging interval times

The second case might be also analyzed mathematically taking into consideration the UV plane trajectories obtained in the previous section. In this case, the variation of "frequency position" in relation to θ variation should be considered. The minimum θ variation that may be chosen is the one that assures that the UV point variation is bigger than $2D$. This condition would assure that no overlapping will be done throughout the whole UV trajectory.

In order to know these conditions, we will proceed with the corresponding mathematical analysis for the two cases considered previously. First of all, derivatives of the UV positions should be calculated:

$$\begin{array}{rcl} \frac{d(\lambda u)}{d\theta} & = & -2(a+b\theta)\sin(\theta)+2b\cos(\theta) \\ \frac{d(\lambda v)}{d\theta} & = & 2(a+b\theta)\cos(\theta)+2b\sin(\theta) \end{array} \tag{3.9}$$

Once these derivatives are calculated, this condition might be stated:

$$\big(d(\lambda u)\big)^2+\big(d(\lambda v)\big)^2>(2D)^2 \tag{3.10}$$

With all the necessary calculus made, this final condition for the two spacecraft configuration is found to be:

$$d\theta>\sqrt{\frac{D^2}{(a+b\theta)^2+b^2}} \tag{3.11}$$

this indicates the minimum θ increment between different snap-shots to assure that every new measuring will cause no overlapping in our UV plane. The same analysis could be brought to fruition for the three spacecraft configuration. Its derivatives and its final θ condition are:

$$\begin{array}{rcl} \frac{d(\lambda u)}{d\theta} & = & [\frac{3}{2}b+\frac{\sqrt{3}}{2}(a+b\theta)]\cos(\theta)-[\frac{3}{2}(a+b\theta)-\frac{\sqrt{3}}{2}b]\sin(\theta) \\ \frac{d(\lambda v)}{d\theta} & = & [\frac{3}{2}b+\frac{\sqrt{3}}{2}(a+b\theta)]\sin(\theta)+[\frac{3}{2}(a+b\theta)-\frac{\sqrt{3}}{2}b]\cos(\theta) \\ d\theta & > & \sqrt{\frac{(2D)^2}{3((a+b\theta)^2+b^2)}} \end{array} \tag{3.12}$$

This second condition permits the calculation of the θ increment in order to succeed in the unitary and full UV coverage at each step, that means that this condition would not be a static parameter of our trajectory. This θ increment depends on the modulus of the spiral, and as it is expanding, this modulus will be different at each step. This fact should be considered when planning the trajectory, whether it would be planned online or offline.

The obtention of these two conditions permit the creation of a UV trajectory that intends to cover the UV plane without overlapping any single frequency, so then it gives the most compact UV coverage possible with these kind of trajectories. This behavior may be observed in figures 3.1 and 3.2:

This full and non redundant UV coverage will only be interesting for determined applications where very precise images in low frequencies should be measured. Otherwise, other conditions for the UV coverage should be stated. For this analysis, apertures of 1m diameter have been considered (which create a UV coverage dot of a diameter of twice this length) and for the case of 2 satellite formation, a complete 2π turn generates the same UV coverage as a unique aperture of 8m of diameter which is technologically not possible in space. For the case of three apertures, with the same complete spiral turn, the coverage achieved would be equivalent to an aperture of 14m of diameter. On the other hand, these maneuvers are subjected to bigger measurement times because, when the unique aperture would take the image with one only integration time, spiral maneuvers would have to perform various reconfigurations. Furthermore, these ideally situations defined in this section would only be perfectly achieved with Stop and Stare maneuvers, which sometime are too fuel consuming. Therefore, Drift Through approaches are a future topic of research, where satellites

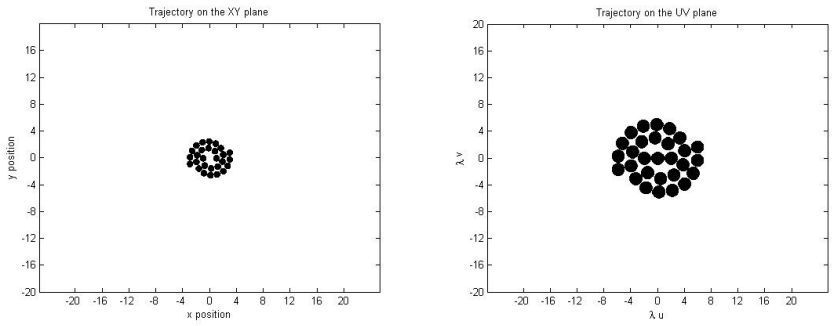

(a) (b)

Figure 3.1: *Spiral trajectory of a two-apertures distributed telescope achieving unitary and full UV coverage: a) XY plane b) UV plane*

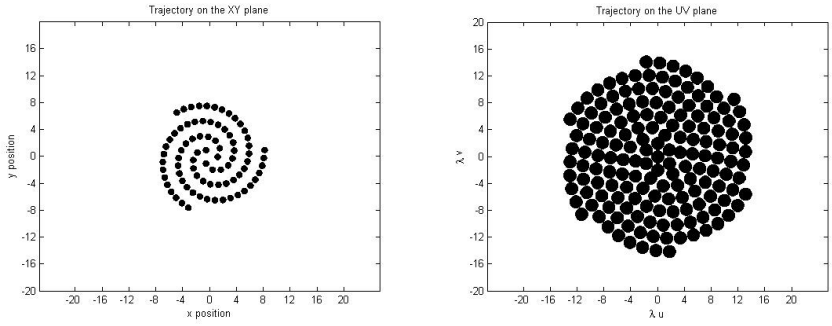

(a) (b)

Figure 3.2: *Spiral trajectory of a three-apertures distributed telescope achieving unitary and full UV coverage: a) XY plane b) UV plane*

will not take steady measurements and they will drift through the measurement locations. These UV measurements will suffer overlapping and some blurry effects on the images should be overcome by postprocessing.

3.2 Design of spiral trajectories

3.2.1 Analysis of spirals dynamics

As a first step of a trajectory design process, the analysis of the dynamics of the trajectory planning about to be effectuated should be realized. In this particular case, the spacecraft trajectories are restricted to a planar movement.

In order to introduce this study, a brief recall of the general planar movement kinematics equations is going to be stated in order to clarify the steps of the optimization process.

Polar coordinates are going to be used throughout this study because those are the most adapted to this kind of kinematics. Thus, the position vector, the velocity vector and the acceleration vector of one spacecraft are defined by equation 3.13:

$$\begin{aligned} \overrightarrow{\boldsymbol{r}} &= r\widehat{\boldsymbol{e}_r} \\ \dot{\overrightarrow{\boldsymbol{r}}} &= \dot{r}\widehat{\boldsymbol{e}_r} + r\dot{\theta}\widehat{\boldsymbol{e}_\theta} \\ \ddot{\overrightarrow{\boldsymbol{r}}} &= (\ddot{r} - r\dot{\theta}^2)\widehat{\boldsymbol{e}_r} + (r\ddot{\theta} + 2\dot{r}\dot{\theta})\widehat{\boldsymbol{e}_\theta} \end{aligned} \tag{3.13}$$

To analyze the necessities of thrust to maintain an spiral trajectory, the analysis will follow with the specification of these general kinematics equations of planar movement in the spiral case. Without lack of generality in the reasoning, an archimedean spiral equation will be used to analyze the main dynamical aspects of this kind of trajectories.

Considering the archimedean spiral vector position stated before ($r(t) = a + b\theta(t)$), the velocity vector and acceleration vector are characterized by:

$$\begin{aligned} \dot{\overrightarrow{\boldsymbol{r}}} &= b\dot{\theta}\widehat{\boldsymbol{e}_r} + (a + b\theta)\dot{\theta}\widehat{\boldsymbol{e}_\theta} \\ \ddot{\overrightarrow{\boldsymbol{r}}} &= (b\ddot{\theta} - (a + b\theta)\dot{\theta}^2)\widehat{\boldsymbol{e}_r} + ((a + b\theta)\ddot{\theta} + 2b\dot{\theta}^2)\widehat{\boldsymbol{e}_\theta} \end{aligned} \tag{3.14}$$

After this brief analysis of the acceleration needs of a spiral trajectory, as it happens in the circular motion, it is concluded that thrusters should be fired all along the trajectory to succeed with the following of a curved trajectory. Whereas in a uniform circular motion, thrusters are only needed to create the necessary centripetal acceleration, in a uniform spiral trajectory, both components of acceleration are needed to expand the radial distance. Nevertheless the overall consumption would be less for spiral maneuvers because if we stop firing within a circular maneuver, the constituent satellites will spiral out as a consequence of conservation of momentum.

Designing a spiral trajectory where the initial and final positions of spacecrafts are defined needs the definition of the angular rate and the acceleration profile but the expansion rate is already fixed by the unitary and full UV conditions stated before. In this thesis, design and analysis of three main scenarios is presented. Continuous scenarios proving the realization of coordinated maneuvers and two interferometric scenarios like Stop and Stare and Drift Through.

3.2.2 Design process for Stop and Stare spirals

Considering the particular case of Stop and Stare spirals, as the satellites should move between steady configurations, there is no need to track completely the whole spiral trajectory. The less consuming scenario is the description of a straight lines between these locations using a bang-off-bang acceleration profiles. In this case spiral dynamics do not intervene. This solution is corroborated by numerous optimal control books [24], [25]. Main results and how these are obtained are described also in appendix A.1, where the minimum Principle of Poyntraguin is stated and used to solve this optimal control problem for the double-integrator plant. In this case, the trajectories described are shown in figure 3.3.

3.2.3 Design process for Continuous and Drift Through spirals

In the case of Continuous and Drift Through spirals, the engineering interest lays in the strict tracking of a spiral trajectory, as a consequence no optimization could be done on the trajectory position variables, because all the planar coordinates to be followed are strictly defined by the spiral evolution, the initial position of the flotilla, their final positions and the image constraints to be attained.

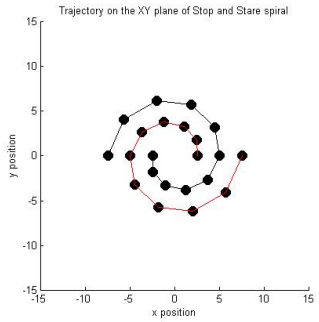

Figure 3.3: *Spiral trajectory of a two-apertures distributed telescope performing Stop and Stare observations. Straight lines are described using a bang off bang acceleration profile between locations.*

Nevertheless, determining the acceleration to be applied by the different thrusters along this determined trajectory are the aspects that will determine the real cost of the maneuver in terms of fuel and time consumption. As a consequence, the optimization procedure in this trajectory design will be to state the acceleration profile of this trajectory.

Thus, the analysis given here assumes that the constellation is spiraled via a trajectory corresponding to a bang-off-bang angular acceleration profile, which is optimal for a double-integrator plant with actuator saturation. Although linear accelerations during the acceleration and deceleration phases of the trajectory are not constant for each spacecraft (the centripetal component changes with θ and other spiral expansion terms change too), the assumption of a bang-off-bang trajectory is a reasonable approach for the spiral maneuver problem, as it is corroborated in reference [22].

Definition of the bang-off-bang profile

The first step of the determination process will be the definition of the main parameters of the desired bang-off-bang profile:

$$\ddot{\theta}(t) = \begin{cases} \alpha & 0 < t < t_a \\ 0 & t_a < t < t_f - t_a \\ -\alpha & t_f - t_a < t < t_f \end{cases} \tag{3.15}$$

$$\dot{\theta}(t) = \begin{cases} \alpha t & 0 < t < t_a \\ \alpha t_a & t_a < t < t_f - t_a \\ -\alpha(t - t_f) & t_f - t_a < t < t_f \end{cases} \tag{3.16}$$

$$\theta(t) = \begin{cases} \frac{1}{2}\alpha t^2 & 0 < t < t_a \\ \frac{1}{2}\alpha {t_a}^2 + \alpha t_a(t - t_a) & t_a < t < t_f - t_a \\ \alpha[t_a(t_f - t_a) - \frac{(t_f - t)^2}{2}] & t_f - t_a < t < t_f \end{cases} \tag{3.17}$$

where t_a is the width of the thrust pulse and t_f is the complete duration of the maneuver.

Once the profile acceleration is defined, an equation limiting the maximum acceleration allowed by the system must be set in order to determine the optimal factors of this profile. System's spacecraft have a limited acceleration capacity and this one should be taken into account.

In this case, linear acceleration demanded to spacecraft is always going to be higher at the final instants due to the expansion of this spiral. This maximum of acceleration will not be always placed

at $t = t_f - t_a$ and it could be placed also at the end of the deceleration interval, at $t = t_f$. This fact depends on the spiraling rate of the spiral and on the acceleration time. For spirals, with a large spiraling rate and short acceleration time (what means large angular acceleration), this maximum will be placed at $t = t_f$, but on the other hand for spirals with small spiraling rate or small values of angular acceleration, this situation could be found at $t = t_f - t_a$.

In the following design process, a parallel procedure is considered in order to be sure that in any case, the design of the trajectory does not exceed the spacecraft capabilities. To do so, this trajectory is designed for both situations taking as valid the most restrictive one.

Knowing the characteristics of the spacecraft forming the mission, it is necessary to define the maximum acceleration that could be demanded throughout the mission. If the magnitude of the smallest available maximum thrust in any direction for any of the spacecraft of the mission is defined as Γ, then the lowest maximum linear acceleration that each spacecraft is capable of is: $\frac{\Gamma}{m}$.

Once the constellation geometry and trajectory type are determined, and the maximum acceleration capability is considered, the next expressions could be formulated (for both instants: $t = t_f - t_a$ and $t = t_f$). This expressions will allow us to solve for the unknown trajectory parameters (α and t_a) given the formation flying system characteristics (initial radius, spiraling rate, final radius, maximum thrust available [Γ] and the spacecraft's mass [m]) and the specified trajectory parameters (θ and t_f). This is done by setting the maximum acceleration to the acceleration bound,

$$\sqrt{a_r^2|_{t=t_x} + a_\theta^2\big|_{t=t_x}} = \frac{\Gamma}{m} \tag{3.18}$$

in which we can substitute, for the first instant, where $t_x = t_f - t_a$:

$$\begin{aligned} a_r|_{t=t_f-t_a} &= (-b\alpha - (a + b\alpha[t_a^2/2 + t_a t_f])\alpha^2 t_a^2) \\ a_\theta|_{t=t_f-t_a} &= -\alpha(a + b\alpha[t_a^2/2 + t_a t_f]) + 2b\alpha^2 t_a^2 \end{aligned} \tag{3.19}$$

and for the second, where $t_x = t_f$, we substitute:

$$\begin{aligned} a_r|_{t=t_f} &= b\alpha \\ a_\theta|_{t=t_f} &= -\alpha(a + b\alpha t_a(t_f - t_a)) \end{aligned} \tag{3.20}$$

Noting that the spiral expansion has a rotation angle defined by: $\hat{\theta} = \theta(t_f) = \alpha t_a(t_f - t_a)$ and that the thruster time should be a fraction of the total maneuver time, we define: $t_a = \gamma t_f$ with $0 < \gamma < \frac{1}{2}$.

Taking all these aspects into consideration and by manipulation of this expressions, complicated non-linear relations are obtained having γ and t_f as independent parameters. This functions, called $\Upsilon(\gamma, t_f)$ are analytically defined in the appendix A.2.

The resolution of this non-linear equations would have only as valid roots, those that place γ within the range between 0 and $\frac{1}{2}$ because those are the only solutions which have physical meaning regarding the problem posed (t_a is defined as $t_a = \gamma t_f$ and $t_a + t_a < t_f$, these conditions imply $0 < \gamma < \frac{1}{2}$). Considering that t_f is a given parameter that the mission engineer would like to determine, the resulting equation yields a sixth order polynomial in γ. Its solution gives four possible scenarios of interest:

1. Case 1: No roots between 0 and $\frac{1}{2}$. This results when the trajectory duration t_f is too short

for the limiting spacecraft to accomplish the trajectory given the rotation angle and its acceleration capabilities.

2. Case 2: Two identical roots between 0 and $\frac{1}{2}$. This case occurs when the minimum possible trajectory duration that is within the capabilities of the limiting spacecraft is chosen.

3. Case 3: Two different roots between 0 and $\frac{1}{2}$. This is unusual in that two different values of γ are found that result in 3.18 being satisfied. However, the smaller value of γ gives a more fuel-efficient trajectory and, therefore, it should be chosen when case 3 occurs.

4. Case 4: One root between 0 and $\frac{1}{2}$. This occurs when the acceleration capabilities of the spacecraft are not stressed by the selection of t_f.

In selecting the trajectory duration (t_f), one specific condition is of great interest. Case 2 that results in the minimum possible trajectory duration for the formation and represents the transition between case 1 (no roots found, and no feasibility of the maneuver) and case 3 (two roots). In figure 3.4, case 1 (dashed), case 2 (solid) and case 3 (dotted) are represented for values obtained for the SPHERES scenario. Hence, finding this minimum time is an important milestone in the design process of this trajectory. This case 2 occurs when:

$$\Upsilon(\gamma, t_f) = 0 \quad \text{and} \quad \frac{d\Upsilon(\gamma,t_f)}{d\gamma} = 0. \tag{3.21}$$

This leads to a resolution of two non-linear equation system, where this condition is satisfied by only one pair of values with physical signification. This resolution is not computational-high demanding and can be solved easily with MATLAB's built in *fsolve* function specifying correctly its necessary optimization parameters with *optimset* function.

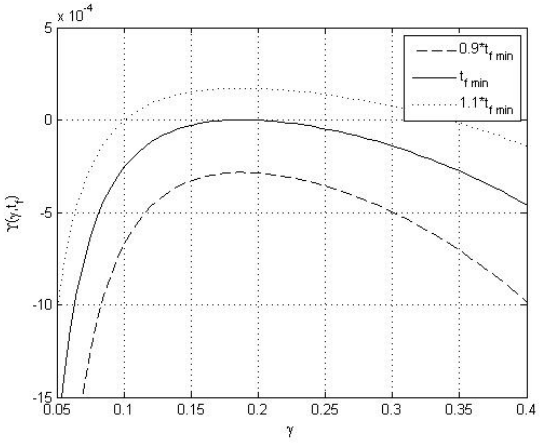

Figure 3.4: *Evolution of* $\Upsilon(\gamma, t_f)$ *for different values of* t_f

Depending on the necessities in image quality, fuel and time consumption, taking into account that big image quality represents long integration times and that fast maneuvers lead to high consumptions, the engineer will define a maneuver duration time bigger than the minimum time defined by the last mathematical condition.

This tradeoff lead to a specific maneuver maximum time. Once this time is determined, a new iteration should be made and solve once more $\Upsilon(\gamma, t_f) = 0$ in order to find the γ value that defines the acceleration profile. As a consequence the fuel usage and the open loop control law of the maneuver may be calculated. This calculation is done in appendix A.3 and appendix A.4.

3.3 Implementation on SPHERES

All previous sections have shown and explained all the procedures of the design process of these type of maneuvers. In this section, this approach is applied to the SPHERES testbed.

Spheres testbed consist on 3 free flyers of $4.3kg$ of mass, and with a thruster capacity of $0.1N$. In order to compute the fuel propelled it is required to know the fuel rate of these thrusters, which is of $4.28 \cdot 10^{-4} kg/s$. All these specific characteristics about the SPHERES testbed are specified in Dr. Simon Nolet thesis [17].

Once these characteristics are known, the same theoretical approach shown in the previous sections may be applied with these numerical values, which leads to the following values for a complete turn (2π) and for a quarter of a turn ($\pi/2$). The complete turn value has been chose to design a Continuous spiral and the quarter of a turn is chosen because the Stop and Stare and Drift Through experiments performed in SPHERES will represent an spiral trajectory with 4 observation points ($\pi/2, \pi, 3\pi/2$ and 2π). In table 3.1, the resulting values of minimum duration to respect spacecraft capacities are shown.

Table 3.1: *Optimization parameters for spiral maneuvers*

Turn Angle (rad)	$\boldsymbol{t_{f_{min}}}$ ***(s)***	$\boldsymbol{\gamma}$
2π	33.809	0.185
$\pi/2$	8.283	0.338

After the first phase, and knowing already the minimum maneuver time that the scientist may demand to this testbed, the procedure of design leads the scientist to a first experiment of spiral maneuvers of a complete coordinated turn between two satellites. This first experiment will realize different time spirals in order to compare their fuel usage and the tracking performance of the different controllers designed within the SPHERES testbed. The minimum time encountered represents the result of a theoretical approach concerning only the open-loop law, but the scientist experimenting with SPHERES has to be conscious that these open-loop laws are going to be tracked by closed loop controllers with a response time non negligible. This fact causes that in the real testbed such a fast trajectory would not be properly followed. As a consequence, in order to implement real tests, the performance of the closed loop controllers have been considered and more relaxed duration spirals have been designed.

The design parameters of these first spirals and their theoretical fuel consumption is:

3.3.1 Matlab simulation

Before sending the trajectory planning algorithms to the ISS, as it has been recommended in the SPHERES operations section, a Matlab simulation should validate the correct behavior of

Table 3.2: *Theoretical design parameters for the complete turn Continuous spiral maneuvers and their fuel consumption*

Turn Angle (rad)	$t_{f_{designed}}(s)$	γ	$t_a(s)$	***Theoretical fuel usage (g)***
2π	120	0.0076	0.906	2.8
2π	60	0.0311	1.865	5.7

the system. In this simulation, the scientist has assured the proper performance of the trajectory planning algorithm and has analyzed that these trajectories are going to be tracked properly by the present system.

The firsts tests planned consider the scenario of Continuous spirals for two satellites formations. First of all, at the beginning of the test and after the deployment phase, the satellites reach their initial positions and they align themselves along the X axis. Right afterwards they start their coordinated maneuver describing spirals about the Z axis. In figure 3.5, planned and real trajectories issued from the Matlab simulation are plotted for the experiment of 120s and the experiment of 60s.

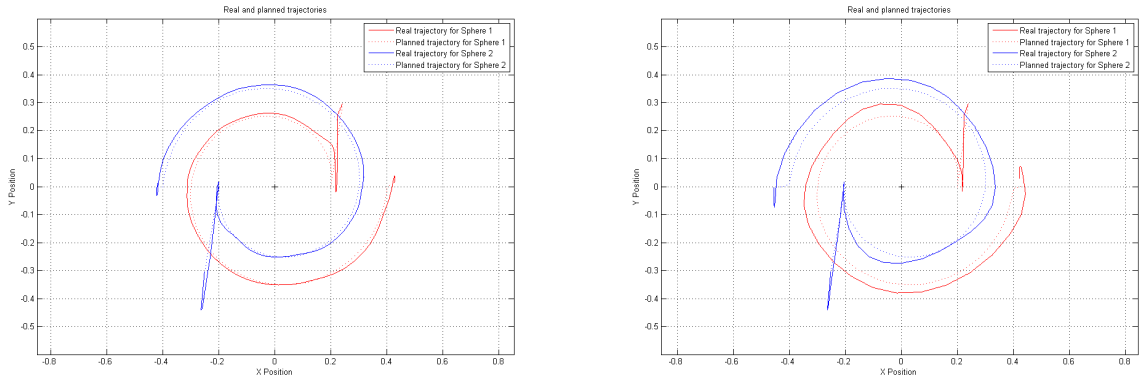

(a) (b)

Figure 3.5: *Matlab simulation of the Continuous spiral maneuvers performed in different times: a) 120s b) 60s*

Table 3.3: *Results of the Matlab simulation for the Continuous maneuvers of 120s, and 60s*

$t_{f_{designed}}(s)$	***Error Sph.1 (cm)***	***Fuel Sph.1 (g)***	***Error Sph.2 (cm)***	***Fuel Sph.2 (g)***
120	2.55	5.64	3.55	5.34
60	5.73	8.71	7.68	8.16

In these continuous experiments (table 3.3), it is observed that fuel usage is similar to the one predicted but a little bit increased due to the fact that in the theoretical approach a decoupled approach between translation and attitude has been followed (consideration of the satellites as mass points). But in reality, those two movements are coupled together due to the satellites geometry. Further studies taking into account this coupled behavior would be interesting. Concerning the

tracking error, as it is shown in table 3.3, close loop controller can not track properly fast maneuvers and they average a position error of around 6cm, on the other hand, with slow continuous spirals, acceptable precision is achieved (around 3 cm).

After the continuous experiments, the author of this thesis has found interesting the development of Stop and Stare and Drift Through trajectories that fulfill more appropriately the interferometric requirements. The first experiment will consist on a Stop and Stare maneuver, where satellites will stop themselves each quarter of turn ($\pi/2$) in order to simulate the instants were the measurements would be taken. In the second experiment, these measurements would not be taken statically, but the satellites will reduce velocity and they will drift through around the observation position (Drift Through measurement of 10°). This type of maneuver will cause a blurrier image in comparison to the one registered with the Stop and Stare maneuver but it will consume less propellant, which is a key aspect of the space systems design. These two experiments have conformed two of the tests of Test Session 13 sent to the International Space Station.

Table 3.4: *Comparison of Stop and Stare and Drift Through maneuvers. Results from Matlab simulation.*

Type	***Ideal fuel usage (g)***	***Error (cm)***	***Fuel usage Sphere(g)***
Stop and Stare	6.8	3.91	13.76
Drift through	5.4	3.66	11.42

As it can be observed in table 3.4 issued from the Matlab simulation of these two scenarios, fuel consumption is higher in Stop and Stare maneuvers in comparison to Drift Through but overall tracking errors are less important due to the fact that the acceleration profile is smoother.

All these tests, as it has been stated in section 1.3, are going to be coded within the structure of Spheres testbed software in order to supply the trajectory reference to the control function, which will effectuate the tracking of the optimal spiral. They have been tested on the MIT 2D table and they will be tested in the International Space Station, when NASA will allocate SPHERES program in their Voluntary Science program.

3.3.2 MIT 2D air table results

After performing the Matlab simulation, firsts tests should be conducted on the MIT air table. These tests have not scientific objective, because satellites are not performing in real environment conditions and there are some important technical difficulties to overcome. For instance, this environment is slightly perturbed by the calibration of the table (gravitational effects) that make the satellite drift. This results in tracking problems, big overshoots and higher fuel consumptions. At the same time, imperfections on the floating system or scratches on the glass table make these tests not totally realistic. Nevertheless, realization of these tests is needed to test the overall behavior of the algorithm. Continuous spirals, Stop and Stare and Drift Through spirals were tested and their results can be observed in table 3.5 and in figure 3.6, showing the realization of these spirals.

As it can be observed, there is less consumption on the Continuous spiral and on the Drift Through maneuver, in comparison to the Stop and Stare maneuver, where most thrusters firing are demanded and the acceleration profile is not smooth. Concerning the tracking error, they represent the average precision with which the tracking controllers have followed the open loop trajectory.

Table 3.5: *Comparison of the Continuous maneuver, the Stop and Stare one and the Drift Through one on the MIT table with the real Spheres testbed*

Type	***Tracking error (cm)***	***Fuel usage (g)***
Continuous	9.62	23.821
Stop and Stare	9.29	26.601
Drift through	7.87	25.319

These tests confirm the trend explained in the simulation section where the less error is found in the Drift Through experiment because it consists on a smoother trajectory and not high demanding, which is easier to track without accumulating big amounts of error. However, main drawback of Drift Through is the blurry effect that causes on images due to the existent relative movement between spacecraft while observing the target. This effect should be mathematically analyzed in order to be able to decide which of the two scenarios is more interesting for future interferometric missions.

3.3.3 International Space Station planned tests

SPHERES program is part of the Voluntary Science onboard the International Space Station, as a consequence the tests performed in Space are scheduled by NASA taking into account astronauts priority tasks and other Voluntary Science. SPHERES program have been rescheduled during the whole month of July and August, and hopefully Test Session 12 and Test Session 13 are going to be tested during the beginning of September 2008. Due to the delay of these tests, these results could not be included in this thesis but they will be analyzed afterwards to draw the necessary scientific conclusions.

3.4 Summary

Interest of spiral maneuvers have been presented at the beginning of this chapter considering their good performance in image quality. Important aspects related to their unitary and full UV coverage have been studied in order to adapt the trajectory planning algorithm to these image sampling situations. Furthermore, fuel wise optimization of spiral maneuvers have been performed considering three different scenarios: Continuous spiral, Stop and Stare and Drift Through. Finally, the trajectory planning algorithm has been adapted to the SPHERES testbed, performing the necessary Matlab simulations. Their good behavior have been proved on the MIT 2D air table with self contained satellites. The tests concerning the real space conditions will be run in the International Space Station during September 2008 and their results will be then analyzed. However, Matlab simulations and 2D air table tests have confirmed the possibility of realizing coordinated fuel minimum spirals in space. At the same time, it has been concluded that Drift Through maneuvers represent a very interesting set of reconfiguration scenarios due to their low consumption and easy tracking.

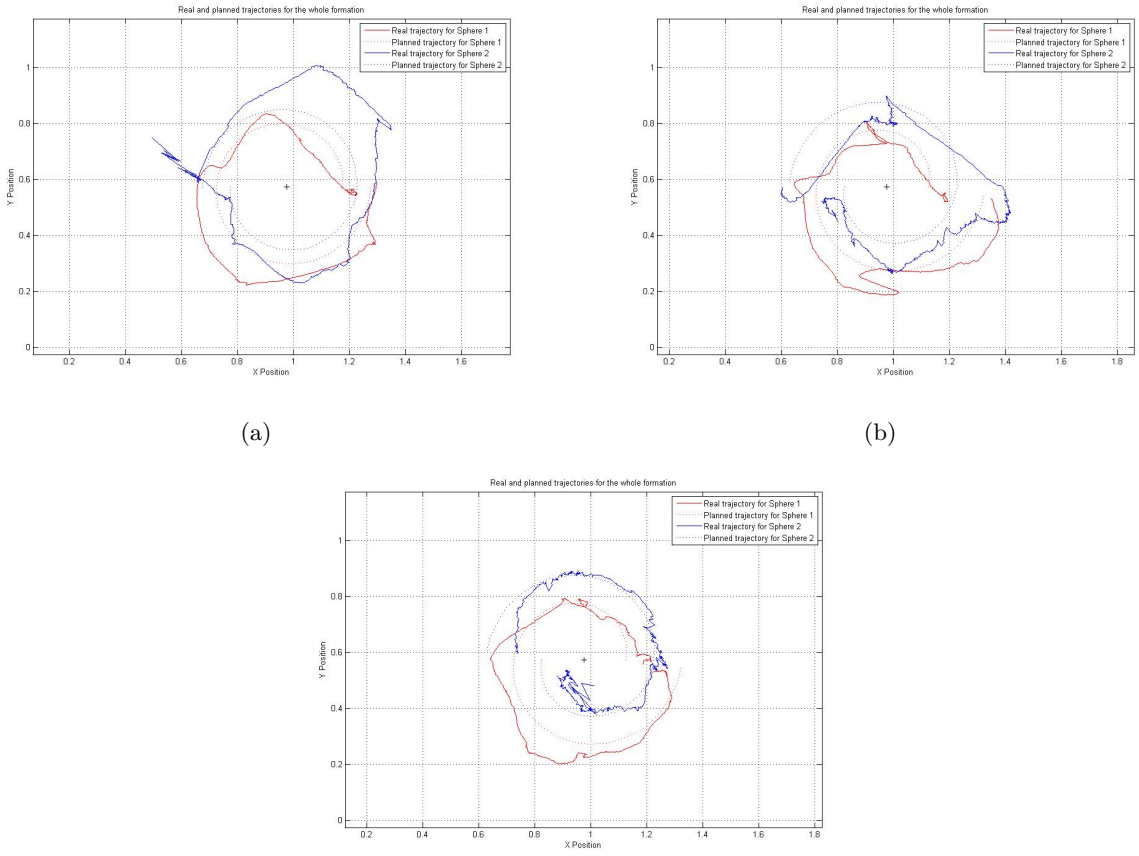

(a)

(b)

(c)

Figure 3.6: *Tests on the MIT air table: a) Continuous spiral b) Stop and Stare spiral c) Drift Through spiral*

Chapter 4

Optimal Imaging Controllers

One of the key fundamentals to the research of multi-spacecraft problems is to maximize the returns of the system given the minimal resources that are available. The ability to minimize the use of theses resources will most certainly ensure longer mission lifetime, which is one of the key aspects of the nowadays missions. As a consequence, the most important aspect of this research is to determine optimal trajectories for these spacecraft taking into account the available resources and the performances obtained.

As it has been explained in previous chapters, formation flying interferometers missions have been already well studied because of their excellent performances to observe celestial objects minimizing the amount of mass needed to be launched and constructing a distributed telescope. As stated before, a major obstacle that must be overcome by Earth orbiting interferometers is the relatively fast dynamics experienced by the spacecraft which makes difficult to achieve the nanometer precision (order of the wavelength observed). Since this precision is required for visible systems, interferometers operating from an Earth orbit will require controls technologies that are currently not available. As such, some missions have proposed placing these interferometers far away from any major body such that a "gravitation free" environment is created. This fact justifies the utilization of the free space dynamics used in this thesis. One of the more popular locations is the Earth trailing Lagrange point, which is hosting and is planned to be hosting a great number of observation missions. Formation flying control and trajectory planning are two of the main key aspects of the mission because they are in charge of assuring image quality (good formation flying control) and optimum utilization of all resources (trajectory planning) [39], [36], [37].

Most of the research made and published until now, showed suboptimal trajectory planning, where the best imaging positions are precalculated beforehand in order to maximize a predetermined image metrics, and afterwards the trajectory optimization is performed to achieve these final positions, but little effort has been yet done balancing image quality and fuel consumption within the same controller.

The objective of this research consists on designing controllers that optimize both image quality and resources at the same time (not suboptimal then), taking into account the actual positions and the status of the imaging process. This applications are interesting because sometimes it would be more interesting to detect poor image quality if important fuel savings are achieved, which will represent an significant increase in mission lifetime.

Determination of optimal trajectories has been extensively studied and researched, besides it

is well documented in plenty of optimal control text books [24], [25]. Various methodologies have been developed to solve these problems. It is not the goal of this research to determine new and alternative methodologies to solve this kind of problems, rather, the optimal control framework is used to obtain these trajectories and these results will be used to systematically analyze the viability of the various missions to meet some requirements.

As such, the theoretical development of the optimal control problem is presented in order to introduce the reader to the framework that is going to be used in the subsequent chapters.

One of the most well known and common approaches to solving optimal control problems is the use of the calculus of variation technique. The main principle of this technique is very simple but at the same time very powerful, and it consists on obtaining the first variation of the optimal control problem and equate it to zero to find the solution. This principle is exactly the same idea used to obtain the extrema of a given function, if it is continuous within the range of interest.

In this chapter, this framework is used to solve two kind of problems. The first one consists on a controller that determines the best trajectories to follow in order to obtain the best imaging configuration at one precise moment of the imaging process. In other words, this controller determines the maneuver which would best increase the image quality taking into consideration the state of the imaging process and the resources consumption. This first controller is named Incremental Controller. The second controller, named as Position Redefining Controller, takes into account the non-noise-free nature of an spacecraft system. Considering that spacecraft do not reach the exact position with the exact speed, this controller reconfigures the final position of the flotilla in order to balance final image quality achieved and fuel used.

4.1 Optimal Control Problem - Variational Approach

The goal of this section is to present to the reader a general understanding of the optimal control problem through the use of the already mentioned Calculus of Variation technique. Theoretically, the formulation presented in this section can be applied to a big variety of problems, but it is concretized to solve the problems of interest for this research.

The objective in solving the optimal problem is to obtain an admissible control u that causes the system:

$$\dot{x}(t) = f(x(t), u(t), t) \tag{4.1}$$

to follow an admissible trajectory x that minimizes the performance cost function:

$$J = h(x(t_f), t_f) + \int_{t_0}^{t_f} g(x(t), u(t), t)dt \tag{4.2}$$

where h is the terminal cost and g is the integrated cost. To ensure that the system dynamics constraint are not violated, the Calculus of Variation technique requires that equation 4.1 be appended to equation 4.2 to generate another augmented cost function which is the one to be optimized:

$$J_{aug} = h(x(t_f), t_f) + \int_{t_0}^{t_f} \left\{ g(x(t), u(t), t) + \psi^T(t)[f(x(t), u(t), t) - \dot{x}(t)] \right\} dt \tag{4.3}$$

this augmentation is done through the use of $\psi(t)$, the Lagrange multipliers. To simplify the notation, most of optimal control text books introduce the Hamiltonian function as:

$$H(x(t), u(t), \psi(t), t) = g(x(t), u(t), t) + \psi^T(t)[f(x(t), u(t), t)] \tag{4.4}$$

which leads to equation 4.3 to be rewritten as:

$$J_{aug} = h(x(t_f), t_f) + \int_{t_0}^{t_f} \left\{ H(x(t), u(t), \psi(t), t) - \psi^T(t)\dot{x}(t) \right\} dt \tag{4.5}$$

The next step in the formulation is to obtain the first variation of the augmented cost function with respect to all its dependencies (x, u, ψ, $\dot{x}$, t) and equate it to zero:

$$\begin{array}{rcl} \delta J_{aug} & = & [\frac{\partial}{\partial x_f} h(x_f, t_f)]^T \delta x_f + [H(x(t), u(t), \psi(t), t) + \frac{\partial}{\partial t_f} h(x_f, t_f)] \delta t_f \\ & & \int_{t_0}^{t_f} \Big\{ [\frac{\partial}{\partial x} H(x(t), u(t), \psi(t), t)]^T \delta x \\ & & + [\frac{\partial}{\partial u} H(x(t), u(t), \psi(t), t)]^T \delta u \\ & & + [\frac{\partial}{\partial \psi} H(x(t), u(t), \psi(t), t)]^T \delta \psi + [-\psi(t)]^T \delta \dot{x} \Big\} dt = 0 \end{array} \tag{4.6}$$

where variations of the augmented cost function with respect to the initial time (t_0) and the initial states are assumed to be zero. Since the initial conditions are usually known and fixed, this assumption is valid. Also, it is worth mentioning that the variations with respect to x and $\dot{x}$ are actually related since the latter is simply the derivative of the former. Utilizing, the simple integration by parts technique, the variation in $\dot{x}$ shown in equation 4.6 can be rewritten as:

$$\int_{t_0}^{t_f} \psi^T(t) \delta \dot{x(t)} dt = -\psi^T \delta x(t) \Big|_{t_0}^{t_f} + \int_{t_0}^{t_f} \dot{\psi}^T(t) \delta x(t) dt \tag{4.7}$$

which, after substitution of equation 4.7 into equation 4.6 leads to the final expression of the variation of the augmented cost:

$$\begin{array}{rcl} \delta J_{aug} & = & [\frac{\partial}{\partial x_f} h(x_f, t_f) - \psi(t)]^T \delta x_f + [H(x(t), u(t), \psi(t), t) + \frac{\partial}{\partial t_f} h(x_f, t_f)] \delta t_f \\ & & \int_{t_0}^{t_f} \Big\{ [\frac{\partial}{\partial x} H(x(t), u(t), \psi(t), t) + \dot{\psi}]^T \delta x \\ & & + [\frac{\partial}{\partial u} H(x(t), u(t), \psi(t), t)]^T \delta u \\ & & + [\frac{\partial}{\partial \psi} H(x(t), u(t), \psi(t), t) - \dot{x}(t)]^T \delta \psi \Big\} dt = 0 \end{array} \tag{4.8}$$

Since the integral must vanish on an extreme regardless of the boundary conditions, the following necessary conditions must be satisfied.

$$\left.\begin{array}{rcl} \dot{x} & = & \frac{\partial}{\partial \psi} H(x(t), u(t), \psi(t), t) \\ \dot{\psi} & = & \frac{\partial}{\partial x} H(x(t), u(t), \psi(t), t) \\ 0 & = & \frac{\partial}{\partial u} H(x(t), u(t), \psi(t), t) \end{array}\right\} t \in [t_0, t_f] \tag{4.9}$$

At the same time, as the variation of the augmented cost must equate to zero at the extremal, the terminal condition must also be satisfied:

$$[\frac{\partial}{\partial x_f} h(x_f, t_f) - \psi(t)]^T \delta x_f + [H(x(t), u(t), \psi(t), t) + \frac{\partial}{\partial t_f} h(x_f, t_f)] \delta t_f = 0 \tag{4.10}$$

4.1.1 Necessary Conditions

The necessary conditions stated in equation 4.9 are conditions that must be satisfied on the extremal regardless of the boundary conditions. The first equation is in fact the dynamics constraint given by equation 4.1. This is easily shown by substituting the Hamiltonian function in this first equation. Commonly, this equation is known as the state equation.

The second equation in equation 4.1 is known as the co-state equation. In general, estimating the co-states is usually the key to solving optimal control problems since they are not intuitively simple to estimate. Expanding this co-state equation gives the following:

$$\dot{\psi} = -[\frac{\partial}{\partial x} f(x(t), u(t), t)]^T \psi(t) - \frac{\partial}{\partial x} g(x(t), u(t), t) \tag{4.11}$$

The third equation occurs from the fact that the variation of $\delta u(t)$ is independent and it must also be equated to zero. In general, the optimal controller for the problem is obtained from this equation, which has as its expansion form:

$$0 = \frac{\partial}{\partial u} g(x(t), u(t), t) + [\frac{\partial}{\partial u} f(x(t), u(t), t)]^T \psi(t) \tag{4.12}$$

These necessary conditions must be satisfied to obtain the solution to the optimal control problem. In cases where the admissible controls are bounded, it can be shown that only the third equation needs to be modified. Furthermore, to guarantee that $u(t)$ causes the Hamiltonian a local minimum, it is sufficient to guarantee that $\frac{\partial^2 H}{\partial u^2}(x(t), u(t), \psi(t), t)$ is positive definite [24], [25].

4.1.2 Boundary Conditions

Besides satisfying the necessary conditions, the variation of the augmented cost (equation 4.8) requires that the boundary conditions be satisfied as well. These boundary conditions can be divided into three general conditions: the initial, the intermediate and terminal conditions. For the present research only the initial and terminal conditions are necessary, so then those are the ones which are briefly discussed here. In case of further interest, the intermediate conditions are well documented in reference [25].

Initial Conditions

For any optimal control problem, it is reasonable to assume that the initial conditions of the states will be known. In aerospace engineering, assuming this fact, relies on the case that the engineer may estimate quite precisely positions and velocities of spacecrafts before the beginning of a determined maneuver. This assumption is already made in the previous formulation of the optimal control problem outlined in this section because that is the case for the present research. In the rare event that the initial conditions are not given and, so then, need to be determined, the formulation can be easily modified including a free initial condition which will lead to a new formulation which will look very similar to the free terminal condition assumption made in this formulation.

Terminal Conditions

As opposed to the fixed initial condition assumption made in this formulation, the terminal condition have yet to be specified. In fact, the free terminal condition assumption made requires the

condition in equation 4.10 to be satisfied. In the case where the variations of the terminal states are independent of the terminal time, which is the case of this research, equation 4.10 can be separated in two different conditions:

$$\begin{gathered} \frac{\partial}{\partial x(t_f)} h(x(t_f), t_f) - \psi(t_f) = 0 \\ H(x(t_f), u(t_f), \psi(t_f), t_f) + \frac{\partial}{\partial t_f} h(x(t_f), t_f) = 0 \end{gathered} \tag{4.13}$$

where both have to be satisfied. If the final state is specified, the variation of the final state (δx_f) is therefore zero, which results in the top terminal condition in equation 4.13 being ignored. The same case is true for problems with their terminal times (t_f) being specified, where the second condition is ignored. This second terminal condition is commonly known as the transversality condition. In this thesis, time is fixed due to the interest of performing determined maneuvers with a predetermined time. However, final states are not specified because they are considered as the optimization variables to obtain the desired image quality.

The derivation of other terminal conditions that are often encountered in optimal control problems may be found in reference [25].

4.2 Linear Quadratic Problems - LQ formulation

The formulation of the optimal control problem in the previous section only assumes that the dynamics and the cost of the system are function of the states, controls and time. There is, however, no assumption made as to what these dependencies are. These dependencies could be highly complicated depending on the kind of problem trying to solve, but in this case the problem is stated with linear dynamic and quadratic cost (LQ). These assumptions could be considered generally valid as it is common practice to linearize complicated dynamics and assuming a quadratic control cost for spacecraft because control effort or thrust is proportional or related to fuel needed. In this section, the necessary conditions and boundary conditions are expressed in the LQ formulation, stating the optimization framework for the ulterior research.

4.2.1 Dynamics linearization

Most rigid body dynamics can be represented by simple linear dynamics systems. For localized distributed imaging systems located most of them in heliocentric orbits, a rigid body dynamic relationship that depends only on the thruster firings can validly be considered, as it will be explained further on in this chapter. In general, this linearization of the dynamics lead to an expression with the following form:

$$\dot{\boldsymbol{x}} = A\boldsymbol{x} + B\boldsymbol{u} \tag{4.14}$$

where the time derivative of the states is just a simple linear combination of the state itself and the control variables.

4.2.2 Quadratic cost function

Since fuel used may be assumed to be directly related to thrust and this thrust may be represented by control effort, u, one can therefore formulate the problem in terms of the already mentioned LQ

framework. In this framework, this quadratic cost can be rewritten as:

$$g(\boldsymbol{x}, \boldsymbol{u}) = \boldsymbol{x}^T Q \boldsymbol{x} + \boldsymbol{u}^T R \boldsymbol{u} \tag{4.15}$$

where the Q matrix is assumed to be semi-positive definite, and R, a positive definite matrix. Since the goal of the controllers designed throughout this thesis is the determination of optimal trajectories in terms of the required control effort and the image quality. The matrix Q is set to zero, because this matrix represent the integrated weighting for the whole trajectory and these controllers are designed to consider the final position but not their evolution. Consequently, the integrated cost used is:

$$g(\boldsymbol{x}, \boldsymbol{u}) = \boldsymbol{u}^T R \boldsymbol{u} \tag{4.16}$$

4.2.3 LQ controller

Once the utilization of linear dynamics and a quadratic cost function has been justified, all the necessary conditions stated in equation 4.9 can be reformulated within the LQ framework, and the results obtained are the following:

$$\begin{aligned} \dot{\boldsymbol{x}} &= A\boldsymbol{x} + B\boldsymbol{u} \\ \dot{\boldsymbol{\psi}} &= -A^T \boldsymbol{\psi} \\ \boldsymbol{u} &= -R^{-1} B^T \boldsymbol{\psi} \end{aligned} \tag{4.17}$$

where the evolution of the state, co-state and control effort is represented. It is worth mentioning once more that the global optimality of the Hamiltonian is assured because $\frac{\partial^2 H}{\partial u^2} = R$ and R is positive definite. Since this optimal LQ controller is a linear combination of only the co-states, one can rewrite both the state and the co-state equations in terms of their own variables. This combination of these two equations into a matrix form, leads to the following state space first order differential expression:

$$\frac{d}{dt} \begin{bmatrix} \boldsymbol{x} \\ \boldsymbol{\psi} \end{bmatrix} = \begin{bmatrix} A & -BR^{-1}B^T \\ 0 & -A^T \end{bmatrix} \begin{bmatrix} \boldsymbol{x} \\ \boldsymbol{\psi} \end{bmatrix} = H\tilde{\boldsymbol{x}} \tag{4.18}$$

where $\tilde{x}$ represents both the state and the co-state variables, and the matrix H is known as the Hamiltonian matrix. From differential equation resolution and particularly, from control theory, this linear differential equation has the following solution:

$$\tilde{\boldsymbol{x}}(t_2) = \Phi(t_2, t_1)\tilde{\boldsymbol{x}}(t_1) \tag{4.19}$$

where $\Phi(t_2, t_1)$ is known as the state transition matrix. Since the system considered here and all throughout this thesis is dependent only on their own variables, the state transition matrix can be represented by the matrix exponential as follows:

$$\Phi(t_2, t_1) = e^{H(t_2 - t_1)} \tag{4.20}$$

Unless the problem is very simple, it is generally not possible to obtain analytical solutions to optimal control problems. As such, numerical techniques are normally used to determine the optimal

trajectories because the procedure of obtaining the initial conditions that match the necessary conditions and at the same time the boundary conditions is not an easy task to compute manually. In order to do so, one simple numerical method is introduced in the next section which is valid to solve the problems treated in the present thesis.

4.2.4 Numerical solution

Obtaining analytical solutions to optimal trajectory problems is almost impossible especially for problems involving a large number of states. The task at hand calls for solving a system of differential equations such that the optimal trajectory may be determined. Normally, the equations can be integrated as long as all the initial conditions are specified. In a N_s spacecraft problem, there are $12N_s$ initial conditions which need to be determined, because each spacecraft counts with 6 states (3 positions and 3 velocities) and the 6 corresponding co-states. Generally, only half of this required initial conditions are specified since none of the initial conditions for the co-states are given. Instead, $6N_s$ terminal conditions should be specified. Such problems are commonly referred to as two point boundary value problems.

A two point boundary problem may be solved using a simple shooting method where an initial guess is taken on the missing initial conditions and then integrates the differential equations to obtain the terminal states. These terminal states are then used to determine the missing initial conditions through Newton-Rapshon's method, and the process is iterated until the specified terminal conditions are met. This simple shooting method is a good starting point to find first valid results, but one should be aware that it consists on a quite numerically unstable method for problems with a large number of states and long integration times $(t_f - t_0)$. This is largely due to the fact that small errors occurred in guessing the initial conditions may translate to large errors at the end of the integration process and the solution may not converge to a valid solution. Nevertheless, to avoid this converging problems large-scale algorithms using the trust-region algorithms [52], [53] could be used before the Newton-Raphson's method to guess roughly the initial values, and then carry out a finer optimization with the latter. At the same time, knowing that fulfillment of the necessary conditions do not assure the finding of the global minima of the function, an extensive search should be performed throughout the whole optimization space, which permits to find the "best" local minima within the optimization domain.

Newton-Rapshon method

In order to find this optimum, all calculation are grouped together using matrix notation which facilitates computation and clarity of results. The problem to solve is the following:

$$L(\tilde{\boldsymbol{x}_0}) = \begin{bmatrix} l_1(\tilde{\boldsymbol{x}_0}) \\ l_2(\tilde{\boldsymbol{x}_0}) \\ \vdots \\ l_{12N_s}(\tilde{\boldsymbol{x}_0}) \end{bmatrix} = 0 \tag{4.21}$$

where the $6N_s$ initial conditions and the $6N_s$ terminal conditions are grouped together within a vectorial manner, where every relation is function of the initial value of the states and the co-states $(\tilde{x_0})$. The goal of the iterative algorithm is to find the set of values $\tilde{x_0}$ which solve at the same time

the set of $12N_s$ conditions stated in equation 4.21. Once these initial conditions are known, the evolution of the states and the optimal control law can be easily calculated using equation 4.17.

In order to do so, this problem can be solved iteratively using Newton-Rapshon's method, which consists on approximating the solution with the one computed with the tangent line of the function (in N-dimensional case, by its Jacobian).

$$\tilde{\boldsymbol{x}_0}^{i+1} = \tilde{\boldsymbol{x}_0}^{(i)} - [J_L(\tilde{\boldsymbol{x}_0}^{(i)})]^{-1} L(\tilde{\boldsymbol{x}_0}^{(i)}) \tag{4.22}$$

where $J_L(\tilde{\boldsymbol{x}_0})$ is the $12N_s$ x $12N_s$ Jacobian matrix of function $L(\tilde{\boldsymbol{x}_0})$.

4.3 Incremental Controller

4.3.1 Controller objective

Interferometric formation flying missions that will be operating around the L2-Lagrangian point will perform different imaging maneuvers in order to best fill in the image UV plane of the celestial object observed (chapter 2). For primary observation objectives, missions might be planned using a global optimization procedure to obtain best image quality independent of fuel usage. Nevertheless, it is well known that throughout a determined observation mission, there is always moments where the desired celestial object might not be in line of sight of our distributed telescope. In these cases, secondary observations (and not planned beforehand) may be done. These secondary observations might not need best image quality and their main interest is to balance image quality with fuel consumption in order to maximize the scientific output of the whole mission without decreasing its lifetime dramatically.

Hence, it is here where an incremental controller maximizing image quality and minimizing propellant resources is interesting. These kind of observations might work as follows: a first imaging configuration will be determined, and a first set of UV-points information will be captured. If the space agency allocates sufficient time for this observation in order to realize a new maneuver, the online controller will determine the maneuver that maximizes the image quality taking into account the status of the imaging process (all UV-points already recorded), and of course, minimizing fuel consumption. This procedure will carry on successively until the spatial agency will abort this secondary mission in order to pass on to a principal one. This controller assures that every time the telescope is designated to realize a new maneuver, the best image quality and fuel usage balance is achieved. It is worth mentioning that this incremental approach will never be as good as a global optimization controller, but the fact of knowing the total number of reconfigurations and the interest of saving fuel makes this incremental controller useful for these kind of applications.

4.3.2 Image metrics

As it has been explained in the first sections about space-based interferometry, multiple array configurations have been studied in order to have optimal imaging configurations for small stationary arrays. For instance, Golay configuration [33] or Cornwell configuration [34] for distributed telescopes of small number of apertures or Golomb configurations [35] for distributed telescopes with a large number of apertures. All of these configurations are non-redundant which means that UV-points are calculated only once and no frequency points replicas are recorded, maximizing the efficiency

of the observation system. Golay and Cornwell metrics are only concerned and based on their corresponding autocorrelations function, in other words on their corresponding UV distributions. Other metrics take into account the encircled energy and others the position of the secondary lobes of the PSF function. Each of these metrics represent the image quality in a slightly different way and each of them could be particularly interesting for different kind of applications, but it is worth saying that any of them takes non-redundancy as one of the most important facts [36], [37].

Therefore, the usage of a simpler image metric that considers non-redundancy as one of the key aspects and at the same time not being highly computational demanding would be an interesting fact for the controller implementation. The image metrics introduced by Dr. Edmund Kong is considered:

$$C_{i,j,k,l} = \sqrt{(u_{i,j} - u_{k,l})^2 + (v_{i,j} - v_{k,l})^2} \tag{4.23}$$

where

$$u_{i,j} = \pm\frac{x_i - x_j}{\lambda} \quad \text{and} \quad v_{i,j} = \pm\frac{y_i - y_j}{\lambda} \tag{4.24}$$

are the measured UV points.

If this equation is maximized, the distance between the UV points is maximized what leads to obtain a fairly distributed spatial frequency information avoiding redundant configurations. At the same time, as it is referenced in Dr. Edmund Kong's work, this metric is representative of the mean square error of the image (MSE). The function to be minimized within the LQ framework is:

$$h = \frac{1}{k^2}\sum \frac{a}{{C^2}_{i,j,k,l}} \tag{4.25}$$

where the inverse of the distances between all UV points are added together and they are weighted by a constant a, which will permit a weighting tradeoff with the control effort. The constant k corresponds to the number of recombinations between UV points. This factor is necessary because as the number of UV points increase, the metrics should be weighted by the number of reconfigurations considered.

This imaging metric is used to implement the final cost of the Incremental Controller designed in this section. Though simple, this imaging metric captures the essential characteristics of a good UV-coverage map, that is, it penalization of short and redundant UV separations, enabling fairly distributed UV coverages.

4.3.3 Cost function and terminal cost

The first step before starting the resolution of an optimal control problem, as it has been explained in the LQ framework section (4.2.3), is the definition of the cost function and the terminal cost that best represent the mission requirements.

Setting the value of matrix R, represents the weighting of each of the control efforts. With high values of this matrix, less control effort will be allowed and as opposite, if little values are chosen for R, big control efforts will be permitted.

On the other hand, the definition of the terminal cost, in this specific problem, depends on the final positions of our spacecraft, that determines the new UV points about to be measured and on all

the UV-points already recorded throughout the whole imaging process. Following the nomenclature specified in the preceding section, this terminal cost function could be expressed as follows:

$$h(x(t_f)) = \frac{1}{k^2}\sum \frac{a}{C^2{}_{i,j,k,l}} = \sum_{k=1}^{\gamma}\sum_{i=1}^{N_s}\sum_{j=1,j\neq i}^{N_s} \frac{a}{(\frac{x_i-x_j}{\lambda}-u_k)^2+(\frac{y_i-y_j}{\lambda}-v_k)^2} \tag{4.26}$$

where γ is the number of all the UV measurements already made and N_s the number of spacecraft of the flotilla.

Once the terminal cost and the cost function are defined, the complete augmented cost of the optimization problem can be stated as:

$$J_{aug} = h(x(t_f)) + \int_{t_0}^{t_f} \left\{u^T R u + \psi^T[Ax + Bu - \dot{x}]\right\} dt \tag{4.27}$$

and from this equation may begin all the optimization procedure.

4.3.4 Optimization problem resolution

Initial conditions

Initial conditions of the spacecraft can be easily known because in these kind of problems, inertial sensors, metrology systems and positioning systems may proportionate a very good estimation of the actual spacecraft position and their velocities. Therefore, $6N_s$ initial conditions are already known. ($6N_s$ initial equations that directly solve the first $6N_s$ unknowns).

Terminal conditions

In order to solve the complete problem, there are still $6N_s$ initial values to be determined corresponding to the co-states (ψ) initial values.

The first $3N_s$ conditions are determined by the fixation of the final velocities of all spacecraft, which should be zero in order to have an stationary array where taking the interferometric measurement. These conditions could be expressed in the following manner:

$$
\begin{aligned}
\begin{bmatrix} x_f(2) \\ x_f(4) \\ x_f(6) \\ \vdots \\ x_f(6N_s) \end{bmatrix} &= \begin{bmatrix} 0 \\ 0 \\ 0 \\ \vdots \\ 0 \end{bmatrix} \\
&= \underbrace{\begin{bmatrix} 0 & 1 & 0 & 0\dots & 0 \\ 0 & 0 & 0 & 1\dots & 0 \\ \vdots & \vdots & \vdots & \vdots\ddots & \vdots \\ 0 & 0 & 0 & 0\dots & 1 \end{bmatrix}}_{3N_s \times 6N_s} \underbrace{\begin{bmatrix} x_f(1) \\ x_f(2) \\ x_f(3) \\ \vdots \\ x_f(6N_s) \end{bmatrix}}_{6N_s \times 1} \\
&= \underbrace{\begin{bmatrix} 0 & 1 & 0 & 0\dots & 0 \\ 0 & 0 & 0 & 1\dots & 0 \\ \vdots & \vdots & \vdots & \vdots\ddots & \vdots \\ 0 & 0 & 0 & 0\dots & 1 \end{bmatrix}}_{3N_s \times 6N_s} \underbrace{[I_{6N_s \times 6N_s} 0_{6N_s \times 6N_s}]}_{6N_s \times 12N_s} e^{H(t_f - t_0)} \begin{bmatrix} x_0(1) \\ \vdots \\ x_0(6N_s) \\ \psi_0(1) \\ \vdots \\ \psi_0(6N_s) \end{bmatrix}
\end{aligned}
\tag{4.28}
$$

Concerning the final states that are not yet determined (the final positions), in order to state the optimal control problem $3N_s$ additional equations are needed. These equations come from the top equation in 4.13 where the final states were not determined. These equations are:

$$
\frac{\partial}{\partial x(t_f)} h(x(t_f), t_f) - \psi(t_f) = 0 \tag{4.29}
$$

only stated for the $3N_s$ states representing the positions of the spacecraft.

The resolution of the optimal control problem presented here may be achieved by the numerical techniques presented in the previous section but a first analysis about the physical meaning of the solutions leads us to the necessity of constraining the optimization space. As it has been specified in equation 4.26, the image metrics used in this optimization tries to maximize distances between UV points, that as a direct consequence, tries as well to maximize distances between the spacecraft's final positions. Therefore, running an optimization without constraining the optimization space leads to results where the final positions of the spacecraft are very far apart from each other what does not represent an implementable solution. Actually, in an interferometric mission, the optical engineer determines the maximum spatial frequency to achieve the desired image resolution, so then it can be assumed that the UV plane has to be filled up to a predetermined maximum spatial frequency. This assumption, leads to constrain the optimization space up to a maximum final position.

Trying to deepen a little bit more in the interests of an interferometric mission of this type, where N_s collectors redirect light towards a main beam combiner, it is very interesting to place all these collectors at the same distance from the beam combiner because this fact will simplify a lot the architecture of the beam combiner, which is the most expensive part of the mission. Therefore, an interesting option for constraining the optimization space consists on placing the N_s collectors within a circle, and this circle centered on the position of the beam combiner. This

circle is determined taking into consideration the maximum spatial frequency needed. This fact does not represent a limiting factor in order to fill in the UV plane because moving satellites close to each other within the circle enables the possibility of obtaining low frequencies and placing them diametrically opposed enables the possibility of measuring the maximum frequency.

This limitation lead to slightly new formulation in order to satisfy all the necessary conditions of the Variational Approach framework. First of all, N_s new conditions are introduced in order to represent the constrain for each satellite of lying within the circumference (2D formulation).

The inclusion of these new constraints, as it is explained in reference [25], lead to a new formulation of the boundary-condition equations, where N_s new variables (here named d_i) have to be introduced. In the general case, where the circumference equations are stated as a hypersurface in the n-dimensional state, k new equations describing this hypersurface may be written:

$$m(x(t_f)) = \begin{bmatrix} m_1(x(t_f)) \\ m_2(x(t_f)) \\ \vdots \\ m_k(x(t_f)) \end{bmatrix} \tag{4.30}$$

.

This means that the final state lies on the intersection of the hypersurface defined by $m(x(t_f))$, and that δx_f is (to first order) tangent to each of the hypersurfaces at the point $(x(t_f), t_f)$. Thus, as a consequence, δx_f is normal to each of the gradient vectors:

$$\frac{\partial m_1}{\partial x}(x(t_f)), ...\frac{\partial m_k}{\partial x}(x(t_f)) \tag{4.31}$$

which are assumed to be linearly independent.

This new fact leads to the possibility of rewriting the boundary-condition equations as follows:

$$\begin{gathered} \frac{\partial}{\partial x(t_f)} h(x(t_f), t_f) - \psi(t_f) = d_1[\frac{\partial m_1}{\partial x}(x(t_f))] + ... + d_k[\frac{\partial m_k}{\partial x}(x(t_f))] \\ m(x(t_f)) = 0 \end{gathered} \tag{4.32}$$

that represent $3N_s + k$ equations that added to the previously mentioned $3N_s$ conditions concerning the terminal velocities conform a problem with $6N_s + k$ unknowns to be determined out of $6N_s + k$ equations. Particularly, concerning the problems treated in this research, there is a new condition for each spacecraft, so then, $k = N_s$.

Although the problem has been stated as a 3 dimensional scenario, its resolution is effectuated within 2 dimensions. These scenarios represent the most typical and interesting scenarios of interferometric missions where the satellites evolve within the plane perpendicular to the direction of light, in order to facilitate the processing task of the beam combiner.

4.3.5 Incremental Controller calculation algorithm

Herein, only a brief presentation of the implementation of the resolution algorithm of the LQR framework for the incremental controller is intended. This pseudo code has as main objective to present a global overview on how this resolution is coded but not specific details about the coding are included.

```
initialization of variables;
for number of reconfigurations do
    extensive creation of starting guesses;
    for number of starting guesses do
        solve the two-point value boundary problem issued from the LQ framework using
        Newton-Raphson's method;
        if algorithm converged then
            integrate differential equation;
            calculate total cost;
            actualize global minima if necessary;
            go to next starting guess;
        else
            go to next starting guess without actualization;
        end
    end
    save global minima;
    record image metrics value and fuel consumption;
    initialize variables for next step;
end
```

Algorithm 1: Incremental Controller algorithm to find optimal trajectory for an specific number of reconfigurations.

4.3.6 Simulation results with two spacecrafts

Firsts analysis of the performance of the optimal controller are done with the simplest case of a mission with only two spacecrafts.

In this case, where only two spacecraft are considered and those are performing within a 2 dimensional space, the matrix A, B and R and the state $\mathbf{x}$ that define the optimal problem are:

$$A = \begin{bmatrix} 0 & 1 & 0 & 0 & 0 & 0 & 0 & 0 \\ 0 & 0 & 0 & 0 & 0 & 0 & 0 & 0 \\ 0 & 0 & 0 & 1 & 0 & 0 & 0 & 0 \\ 0 & 0 & 0 & 0 & 0 & 0 & 0 & 0 \\ 0 & 0 & 0 & 0 & 0 & 1 & 0 & 0 \\ 0 & 0 & 0 & 0 & 0 & 0 & 0 & 0 \\ 0 & 0 & 0 & 0 & 0 & 0 & 0 & 1 \\ 0 & 0 & 0 & 0 & 0 & 0 & 0 & 0 \end{bmatrix}, \quad B = \begin{bmatrix} 0 & 0 & 0 & 0 \\ 1 & 0 & 0 & 0 \\ 0 & 0 & 0 & 0 \\ 0 & 1 & 0 & 0 \\ 0 & 0 & 0 & 0 \\ 0 & 0 & 1 & 0 \\ 0 & 0 & 0 & 0 \\ 0 & 0 & 0 & 1 \end{bmatrix}, \quad R = r \begin{bmatrix} 1 & 0 & 0 & 0 \\ 0 & 1 & 0 & 0 \\ 0 & 0 & 1 & 0 \\ 0 & 0 & 0 & 1 \end{bmatrix}, \quad \boldsymbol{x} = \begin{bmatrix} x_1 \\ v_{x_1} \\ y_1 \\ v_{y_1} \\ x_2 \\ v_{x_2} \\ y_2 \\ v_{y_2} \end{bmatrix} \tag{4.33}$$

Firsts steps of the optimal controller

In this section the results of the implementation of this optimal controller at the beginning of an image measurement are shown, where no UV-point have yet been measured and this optimal controller tries to find the best steps to perform at each time. This optimization starts from an

initial determined configuration where the two spacecrafts are placed diametrically opposed along the X axis.

The incremental steps determined by the optimal online controller are related to the different values of the r value that represent the weighting on the control effort and a that represent the weighting on the terminal cost, in particular the behavior's trend of the controller is related to the ratio between these two values (r/a ratio). As a first analysis, for large values of r in comparison to a, low values of commands are allowed, so then the positions of the satellites do not vary a lot and the performance of the system in terms of image quality is not very significant. On the other hand, when the controller optimizes the incremental steps with a value of a larger than r, new positions are found to improve a significantly the image quality but consuming a little bit more of propellant.

The evolution of the reconfiguration steps are observed in figures 4.1 and 4.2 and figure 4.3, where the spacecrafts are positioned in order to minimize the cost function. It is worth mentioning that with the LQ framework used in this research we assure a global optimum for the Hamiltonian because R is positive definite, but concerning the terminal cost we only can assure that it consists of a relative extrema, leading to a suboptimal controller. To overcome this problem, an extensive search is performed to find the best extrema in the domain of interest. Logically this linear extensive search is not exhaustive and it increments a lot the computing resolution time. Despite proportionating still a suboptimal solution, this one is the "best" while using an acceptable computation time. As future work, more computation efficient algorithm to find global maxima should be used or developed.

Herein the evolution of this controller for a low weighting in fuel is shown (figure 4.1 and 4.2), and it can observed that the evolution is similar to the optimal predefined one, getting all UV points the furthest apart as possible. The spots characterizing the evolution of the satellites are plotted from dark to light color, dark representing firsts steps and light color representing lasts steps.

On the other hand, if the ratio r/a is high, this incremental controller cannot consume all the fuel it needs to get to the optimal position, and it computes an intermediate solution that proportionates the best image quality being conservative with the onboard resources. As it confirmed by the next simulation of the evolution of the controller (figure 4.3), for large values of the ratio r/a new configurations obtained represent little displacement distances for all constituting satellites. As a drawback, the increment in the optical performance is not as good.

This same behavior may be observed in the following table 4.1 where the evolution of the image metrics of these two scenarios is presented and compared to an optimal configuration (knowing number configurations and obtaining best image quality without caring about fuel). It is observed that MSE is decreasing in both scenarios but this decrease evolution is steeper for a low r/a ratio because large amount of fuel can be consumed and getting a good metrics is an important fact for the controller. In figure 4.4(a), it is observed that the image metrics of the different configuration for a low r/a ratio is close to the optimal imaging configurations, but, on the other hand, for high r/a ratio, high sacrifices are done concerning image quality. In figure 4.4(b), a logical trend of the energy usage can be seen where this one increases where the number of reconfiguration does so. Besides, this consumption is higher for the case where a better metrics is obtained, what leads us to the performance/resources tradeoff that should be decided and adapted for the specific mission.

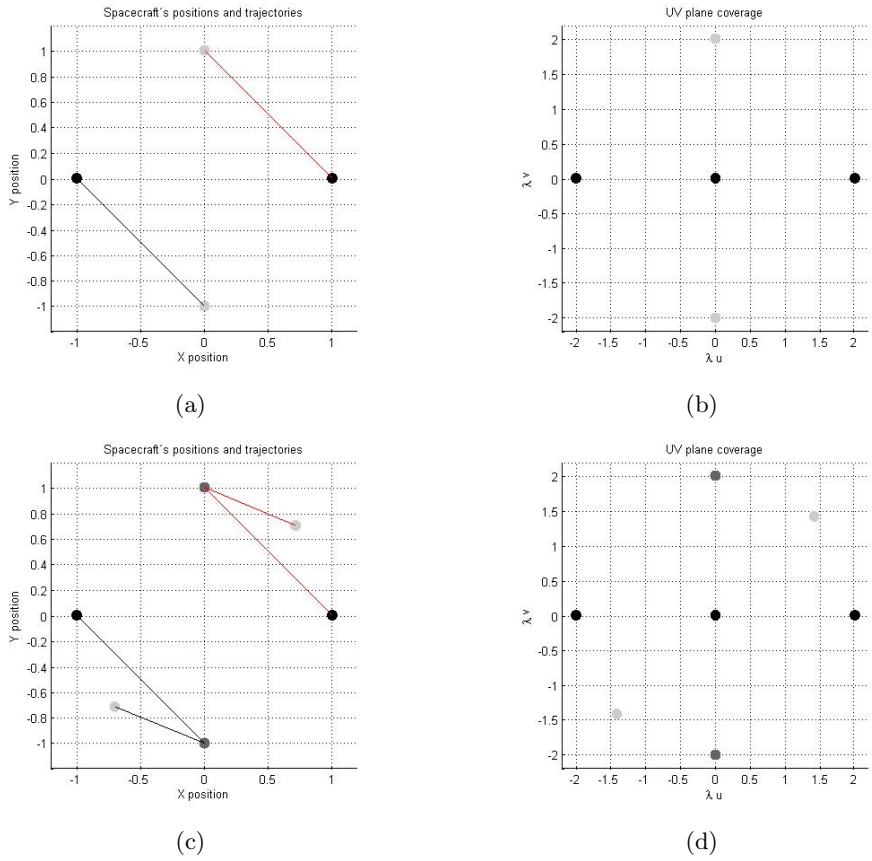

Figure 4.1: *First two steps performed by the optimal controller with low r/a ratio: a) XY plane (first step) b) UV plane (first step) c) XY plane (second step) d) UV plane (second step)*

Table 4.1: *Image metrics evolution along the Incremental Controller reconfigurations. Units of this image metrics comparable to MSE* $(W/m^2)^2$

Reconfigurations	***Low r/a ratio***	***High r/a ratio***	***Optimal Configurations***
1	0.2500	0.2500	0.2500
2	0.0295	0.0585	0.0226
3	0.0128	0.0248	0.0114
4	0.0072	0.0225	0.0062
5	0.0054	0.0151	0.0051
6	0.0044	0.0083	0.0038
7	0.0035	0.0051	0.0029
8	0.0029	0.0041	0.0022
9	0.0023	0.0029	0.0018
10	0.0019	0.0023	0.0015

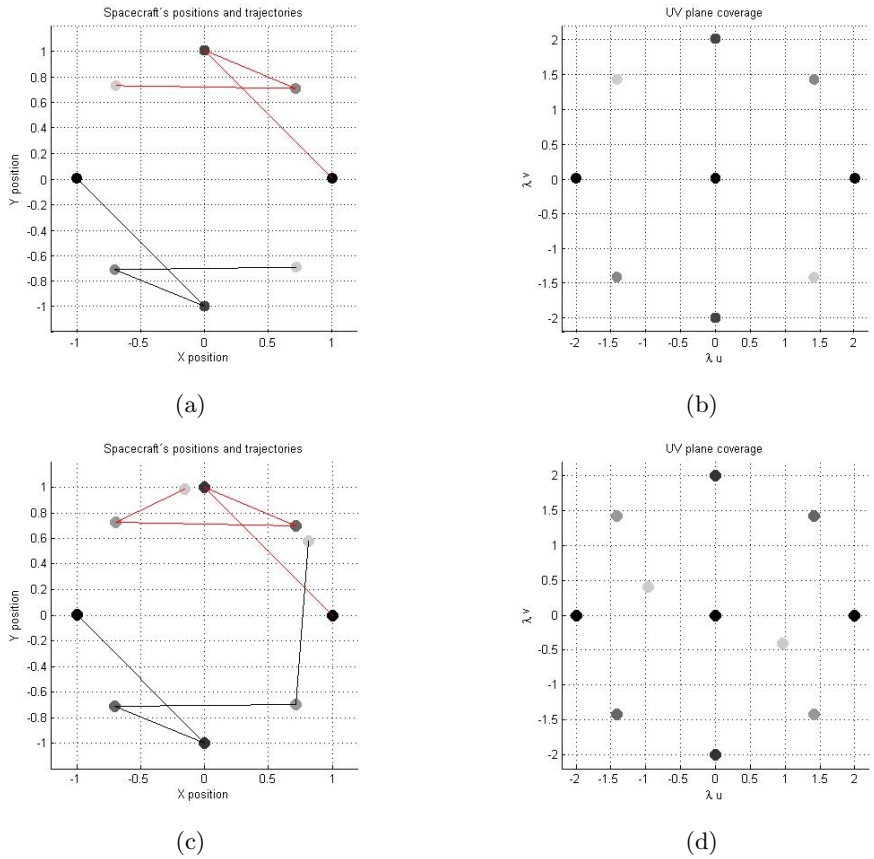

Figure 4.2: *Steps 3 and 4 performed by the optimal controller with low r/a ratio: a) XY plane (third step) b) UV plane (third step) c) XY plane (fourth step) d) UV plane (fourth step)*

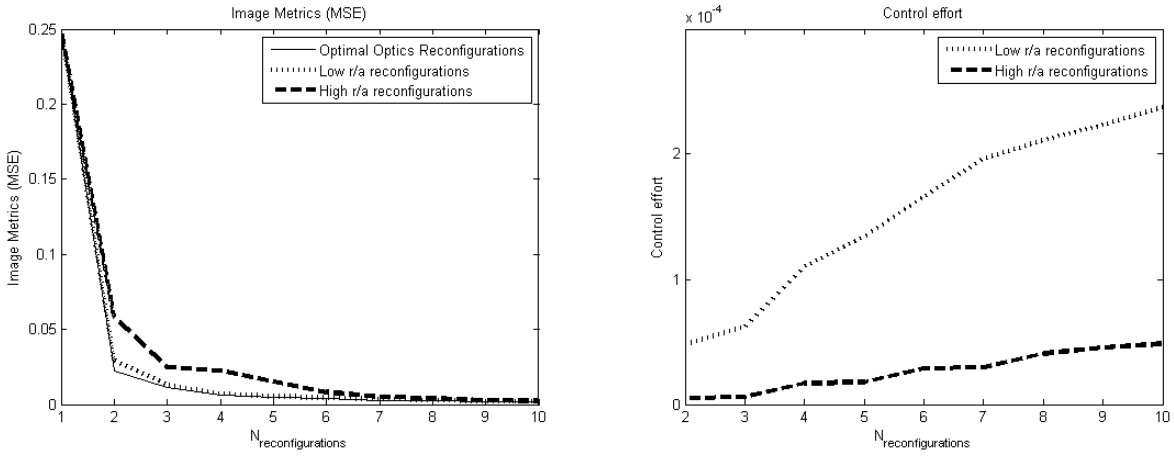

Figure 4.4: *Performance of the Incremental Controller for different values of ratio r/a: a) Image metrics comparison b) Energy comparison*

This study shows the trends and the good behavior of the application of these kind of controllers and their interest where the number of reconfiguration is unknown. Nevertheless, this study repre-

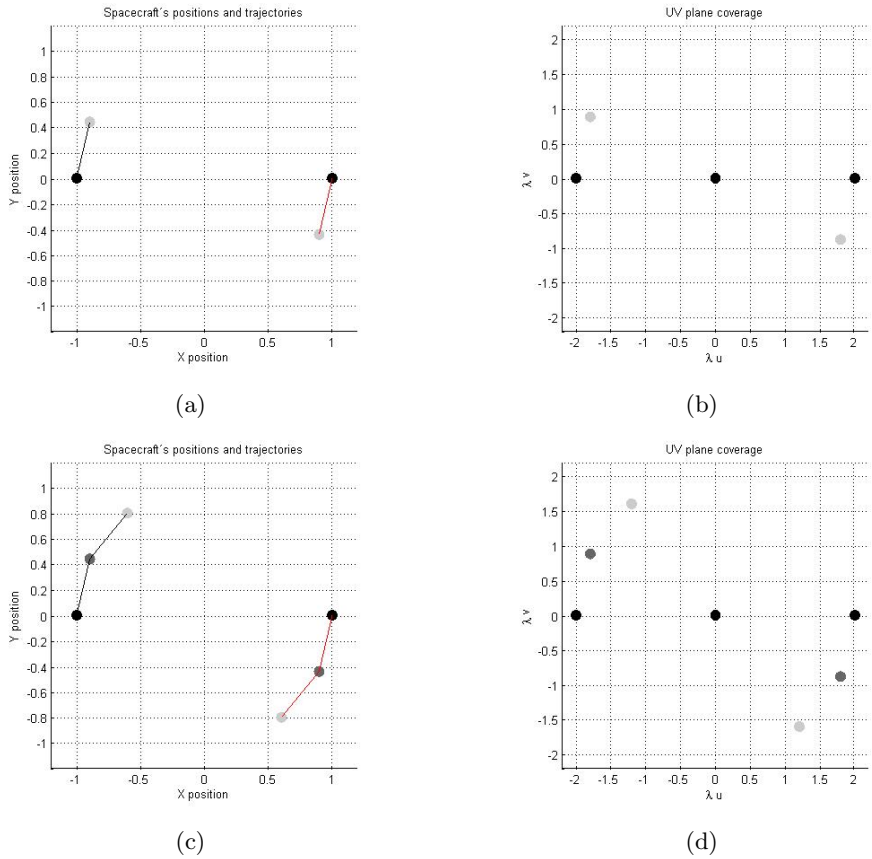

Figure 4.3: *First two steps performed by the optimal controller with high r/a ratio: a) XY plane (first step) b) UV plane (first step) c) XY plane (second step) d) UV plane (second step)*

sents only the first engineering step, where the controller has been designed and its performance has been analyzed. Before implementing this controller in real missions, specific tests, simulations and adaptation of parameters should be realized to obtain the desired performance for the specific mission.

4.4 Position-Redefining Controller

4.4.1 Controller objective

The second type of optimal controller developed in this research share the same objective of the ulterior section, where the interesting requirements are the image quality and the fuel usage. However, the application of this controller is within a different context.

When the number of spacecrafts are known and so are the number of reconfigurations to realize all the measurements of an image, an optimal approach can be calculated beforehand and all the trajectories and configuration positions of the spacecraft flotilla can be determined. These final positions of each reconfiguration represent the optimal way to sample the image.

Unfortunately, controlling satellites is not an ideal world because of multiple perturbations: approximation of the free space dynamics, solar wind perturbation, drift and tracking errors and

a lot others will cause that the final positions will not always be achieved very precisely. The final approach phase, where each of the satellites try to reach their precise state (position and velocity) is normally the more fuel and time consuming phase because it represents the phase where more accuracy is needed and normally these perturbations make the stabilization process last too long.

In order to avoid a large amount of fuel consumption in this final approach phase a Position-Redefining controller is designed. This controller starts its application when each of the satellites reach a close position to the desired final configuration. Once this area of influence reached, the controller takes into account the real state of the satellite and the real state of the other satellites and computes a new configuration which minimizes the image metrics error in comparison to the initial metrics designed and at the same time tries to minimize the fuel consumption of these spacecraft.

This optimal online controller monitors only the last approach of the maneuver because his mission is only the minimization of resources in this last high cost phase but not to replan the whole image procedure that was designed from the ground and that has been widely studied by other authors [36],[37].

4.4.2 Image metrics

As it has been stated in the previous section, the main interest of this controller is the minimization of the difference between the final image metrics and the initially planned image metrics, while minimizing the usage of resources. This controller needs an image metrics of easy computation because this online controller should converge to a solution within an acceptable amount of time and it cannot envisage a long optimization algorithm like the ones that can be run on ground powerful computers.

The image metrics proposed for this controller minimizes the square error between the real UV points that are sampled with the ones that were planned to be sampled. As it was explained in the introductory section, the UV points are defined by the relative positions of each pair of spacecraft, so then the same UV points could be achieved without reaching the predefined XY configurations, what gives an interesting flexibility to the optimal controller. Thus, the image metrics proposed for the present controller is the following:

$$h(x(t_f)) = \sum_{i=1}^{N_s} \sum_{j=1, j\neq i}^{N_s} \left(\frac{(x_i - x_j)}{\lambda} - u_{i,j_{obj}}\right)^2 + \left(\frac{(y_i - y_j)}{\lambda} - v_{i,j_{obj}}\right)^2 \tag{4.34}$$

where $u_{i,j_{obj}}$ and $v_{i,j_{obj}}$ are the UV points defined at the starting plan of the mission.

Logically, if the controller can balance the amount of fuel necessary to obtain this UV positions, it tries to position this spatial frequency samples exactly in the same place, but on the other hand, if the amount of fuel necessary to reach them is excessive, it reconfigures the whole flotilla to a nearby position that does not deteriorate a lot the desired image performance.

4.4.3 Cost function: Balance between image quality and fuel consumption

Similarly as it has been defined in the section corresponding to the incremental controller, the cost function introduced to the optimal controller is a weighting function between the two main aspects that the controller should assure. The image metrics is represented by the terminal cost of the cost function because this metrics depends only on the final positions and the fuel consumption

is introduced in the integrated part, which represents the history of consumption throughout the whole trajectory.

$$J = h(x(t_f)) + \int_{t_0}^{t_f} u^T R u dt \tag{4.35}$$

4.4.4 Problem resolution

In this section, only a brief recall of the necessary conditions leading to the two-point boundary problem is done, because the resolution approach is very similar to the one realized in section 4.3.4 for the Incremental Controller.

Initial conditions

Initial conditions of the spacecraft can be easily known because inertial sensors, metrology systems and positioning systems may proportionate a very good estimation of the actual spacecraft position and their velocities. It is worth mentioning that the monitoring phase of this controller will be beginning also depending on the measurements of the spacecraft which are reasonably reliable. Therefore, $6N_s$ (3 positions and 3 velocities per spacecraft) initial conditions are already known.

Terminal conditions

In order to solve the complete problem, there are still $6N_s$ initial values to be determined corresponding to the co-states (ψ) initial values. As it was explained during the resolution of the Incremental Controller, the first $3N_s$ conditions are determined by the fixation of the final velocities of all spacecraft, that also in this case are fixed to zero.

Concerning the final states that are not yet determined (the final positions), $3N_s$ additional equations come from the top equation in 4.13:

$$\frac{\partial}{\partial x(t_f)} h(x(t_f), t_f) - \psi(t_f) = 0 \tag{4.36}$$

only stated for the $3N_s$ states representing the positions of the spacecraft (not for the states representing velocities).

4.4.5 Position Redefining Controller calculation algorithm

Herein, as it has been done in the Incremental Controller section, a brief pseudo code of the resolution algorithm for the Position Redefining Controller is presented in order to show a general overview of the resolution of LQ framework for this specific problem. In this case, a statistical analysis has been performed to take into account the random nature of this physical system.

```
initialization of variables;
for number of realizations of the statistical analysis do
    generate normal-random state of arrival;
    extensive creation of starting guesses;
    for number of starting guesses do
        solve the two-point value boundary problem using Newton-Raphson's method;
        if algorithm converged then
            integrate differential equation;
            calculate total cost;
            actualize global minima if necessary;
            go to next starting guess;
        else
            go to next starting guess without actualization;
        end
    end
    save global minima;
    compare performance to the state before the reconfiguration;
    record image metrics and fuel consumption;
end
analyze results of the statistical analysis;
```

Algorithm 2: Position Redefining Controller algorithm to find optimal reconfigurations minimizing image metrics error.

4.4.6 Simulation results

In this second application, the image metrics is of simpler computation, because the main optimization algorithm to determine optimal imaging locations has been performed beforehand. Nevertheless, when it comes up to a high number of spacecrafts, a centralized approach like the one presented up to now is not going to be implementable.

As it has been presented in the previous section of results concerning the Incremental Controller, the behavior of these controllers is highly dependent on the ratio between the image metrics and the fuel consumption. Thus, the analysis of results will also consider the two main situations, low and high r/a ratio.

Concerning the first scenario, where a low weighting is forced on the fuel metrics, the controller enables to use the sufficient amount of propellant in order to reach the relative positions between spacecraft that permits the system to measure the same UV point samples. Depending on the initial state (position and velocities) of the spacecrafts at the beginning of the monitoring process the optimal controller determines the best trajectories to position the spacecraft in the right optical configurations.

In figures 4.5 and 4.6, the case of 4 spacecrafts can be graphically examined, where the satellites arriving with a random state around the final desired state are repositioned in order to obtain the same optical performance. Figure 4.5, concerning the low r/a ratio, shows that the satellites are reconfigured in a manner that the same UV points are sampled. On the other hand, with a high r/a ratio, as it is observed on figure 4.6, the controller cannot allow the satellites to reposition

in order to obtain the maximum image quality, and the UV points sampled are not the same (crosses representing the real UV points samples and dots representing the planned UV point do not coincide), because in order to consume low fuel satellites describe only straight lines which are less consuming. Therefore, the image processus is a little bit deteriorated. The results of this simulation are for extreme values of the r/a ratio, in order to analyze the trend of the controller's behavior. Depending on the fuel status and the necessary quality of the actual UV snapshot, r/a ratio should be adapted for the specific mission. Generally for precise missions, this ratio will be fairly low because the objective is saving fuel but never be too far from the UV frequency points desired.

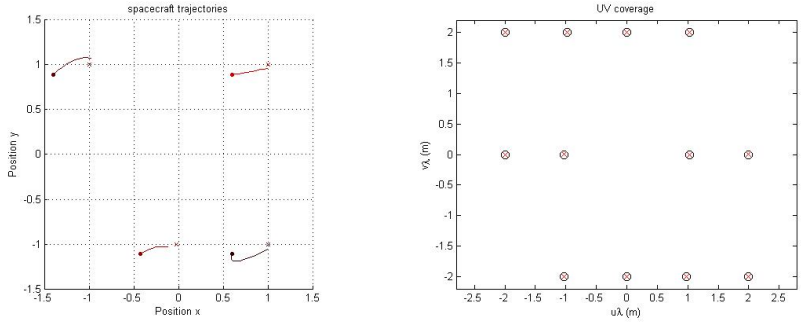

(a) (b)

Figure 4.5: *Repositioning of a 4 satellites formation with low r/a ratio : a) XY plane b) UV plane*

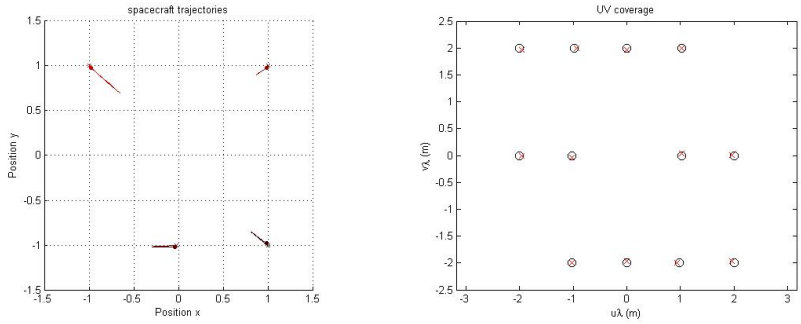

(a) (b)

Figure 4.6: *Repositioning of a 4 satellites formation with high r/a ratio : a) XY plane b) UV plane*

Statistical analysis on the Stellar Imager mission

The Stellar Imager mission is composed of a flotilla of around 30 satellites of 65kg each one that are distributed within a parabola with a maximum baseline of 1000m and a minimum one of 100m, typically of 500m. Using these values, a simulation of the Position Redefining Controller on this system will be implemented to characterize its behavior and evaluate its applicability and its performance.

Firstly, optimal configurations for different number of spacecrafts are obtained. Secondly, a state of arrival is simulated considering that the system is not ideal and that the satellites reach their

position with the correspondent physical random noise. Particularly, each satellite will get close to the final position with a standard deviation in position of $\sigma_{pos} = \frac{1}{100}B$, where B is the baseline and a standard deviation in velocity of $\sigma_{vel} = 0.5m/s$. After this recreation of scenario, the controller computes the best new configuration for a low and high r/a ratio. The resulting image quality is compared to the ideal one and the total consumption is compared to the fuel usage before the reconfiguration. These experiments are effectuated for different number of spacecrafts and with 25 realizations.

Table 4.2: *Results of the statistical analysis for SI mission for a low r/a ratio*

$N_{spacecraft}$	***Relative Error in metrics***	***% of control effort used***
2	$4.816 \cdot 10^{-8}\%$	85.598%
3	$1.335 \cdot 10^{-7}\%$	95.389%
4	$4.634 \cdot 10^{-7}\%$	98.947%
5	$4.883 \cdot 10^{-7}\%$	99.441%

Table 4.3: *Results of the statistical analysis for SI mission for a high r/a ratio*

$N_{spacecraft}$	***Relative Error in metrics***	***% of control effort used***
2	0.900%	56.313%
3	2.178%	37.378%
4	7.151%	33.606%
5	7.234%	29.069%

As it can be observed in figure 4.7(a) and in table 4.2, for a low r/a ratio, where a very good image quality is desired to be achieved, as the number of satellites increases, the maintenance of good image quality requires amount of fuel of the same order to the one used before the reconfiguration. Consumption percentages are around 95% and error in image metrics are negligible. This is due to the fact that wanting to attend an exact configuration gives little flexibility to the reconfiguration and nearly the same amount of fuel should be consumed.

On the other hand, as it can be seen in figure 4.7(b) and in table 4.3, for a high r/a ratio, if certain percentages of error on the image metrics are permitted, larger fuel savings are obtained in missions with larger number of satellites, because the fact of considering large number of variables gives more flexibility to the system and better improvements can be achieved. In this case, for instance, in the case of 5 satellites, savings of fuel around 70% may be achieved if the optical performance is decreased by a 7%. This error in metrics may be excessive but this performance in fuel savings gives an idea of the flexibility of the controller and proves the interest of using repositioning controllers for the final approach phase of any pre-configured formation flying mission.

4.5 Summary

The theoretical development using the calculus of variation technique applied to optimal control problems has been presented in this chapter. Through the formulation, it is observed that the

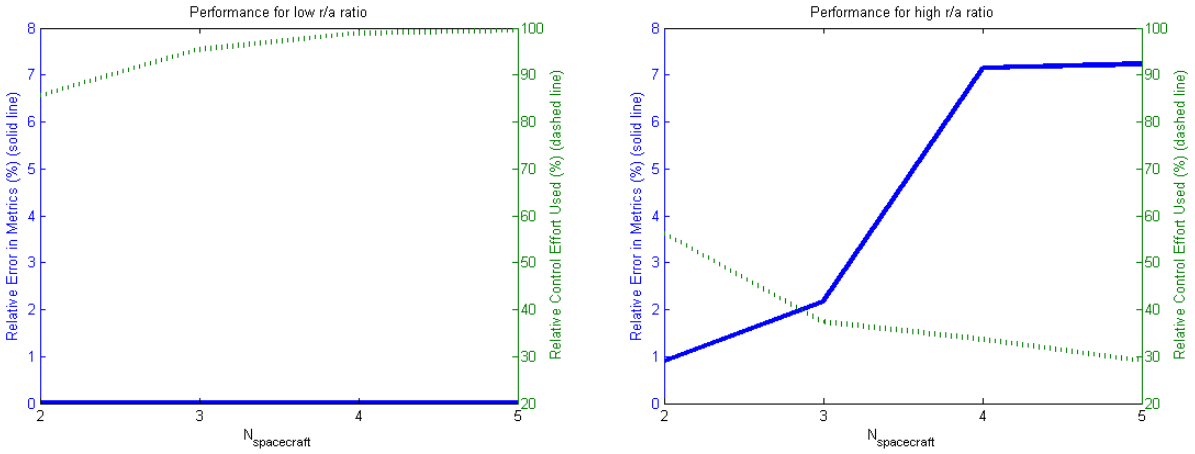

(a) (b)

Figure 4.7: *Performance of the repositioning controller: a) low r/a ratio b) high r/a ratio*

optimal trajectories are determined by satisfying both the necessary and boundary conditions. The formulation is then extended to consider a linear dynamic system with a quadratic cost function, such that the LQ controller is obtained. This LQ framework is used throughout this chapter to determine the results for the various optimal imaging controllers designed.

The Incremental Controller realizes always the best reconfiguration step trading off between image quality and fuel consumption and this chapter proves its capacity of performing good observations without knowing the number of reconfigurations that are going to be allowed to the present mission. The second controller designed is the Position Redefining Controller, which highlights the interest of monitoring the final approach phase of a satellite formation to a defined configuration in order to perform interesting fuel savings while conserving an acceptable image quality.

Chapter 5

Conclusion

5.1 Thesis summary and contributions

The necessity of improving exploration of outer space in order to answer some fundamental questions about the universe and its formation requires the improvement of the present observation systems to collect direct observational evidence. Monolithic telescopes have reached their limit in angular resolution, therefore in this present research the interest of performing interferometry within a distributed telescope is discussed. In the first two chapters the interest of using distributed spacecraft missions and interferometry is presented concluding that nowadays represents the most interesting space-based proposal to overcome angular resolution and intensity limiting factors.

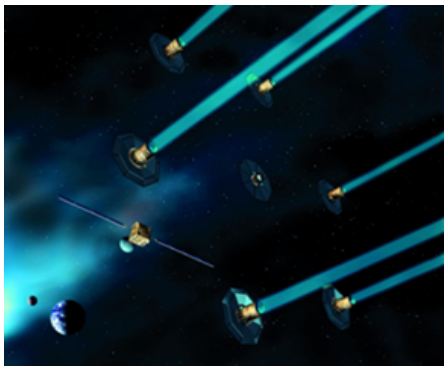

Figure 5.1: *ESA's Darwin mission for the quest of extrasolar planets*

Once the necessity of developing distributed spacecraft mission is demonstrated, research should be developed to analyze how to control these distributed systems and formation flying techniques have to be studied. Particularly interesting is the analysis of the implementability of coordinated maneuvers that lead to realize optimal reconfigurations to complete celestial observations. The interest of balancing image quality aspects and fuel consumption of the whole satellite flotilla is shown in this research, concluding that better savings in fuel usage could be achieved.

Particularly, in the first part of this research the implementability of a trajectory planning algorithm to realize coordinated spiral maneuvers in real space conditions using SPHERES testbed is proved. These spiral coordinated maneuvers being very interesting from the optical point of view have to be optimized fuel wise in order to minimize resources consumption. A new spiral maneuver

design process have been determined by the author and these algorithms have been implemented in SPHERES testbed. Only computer based simulation were not enough to demonstrate feasibility of spiral coordinated maneuvers, but during this research, the fact of having the possibility to use SPHERES as a real space conditions testbed, real tests have demonstrated their implementability using the concept of Virtual Structure formation flight.

At the same time, this research corroborates the interest of Drift Through in front of Stop and Stare maneuvers because it has been demonstrated that their tracking is easier and their fuel consumption is lower due to their smoother profile. Blurry effects due to their continuous relative movement should be studied to conclude which set is more interesting. No study has been done yet concerning this blurriness, so then it represents an important proposal for future work.

In the second block of this research, Optimal Imaging Controllers are designed proving the interest of combining image quality and fuel metrics within the same controller. This fact permits to find optimal trajectories between steady-observation configurations with an interesting balance between both key mission aspects. Up until now, a lot of research contributions were made consisting on the separate study of image quality and fuel consumption. This separate study leads to a very valid suboptimal solution of the engineering problem. Nevertheless, these solutions represent the minimum fuel usage to obtain the best image quality, which is a very restrictive scenario because those two optimization factors are not always independent. Space-based observation missions are highly dependent on fuel consumption because their life time is directly related to this consumption, and some times a worse observation would be worth if it represents a high fuel saving. Therefore the author presents in this research some preliminaries studies balancing both key aspects within the same optimal controller.

Specifically, the contribution of this research concerning optimal imaging controllers is the development of two new imaging controllers and the analysis of their behavior. The first controller is the Incremental Controller, which proves the efficiency of performing always "the best" step balancing image quality and fuel consumption without knowing the number of total reconfigurations allowed within the whole mission. Concerning the Incremental Controller, it has been proved its performance is satisfactory (less than $0.01(W/m^2)^2$ mean square error of image quality) with more than 4 reconfigurations and its error is monotonically decreasing. The second controller is the Position Redefining controller, which takes into account the non-noise-free nature of the distributed telescope system and considers the state of satellites in order to reconfigure their final position to achieve acceptable image performance while saving considerable amounts of fuel. This research has proved that depending on the state of satellites (positions and velocities), acceptable image quality observations can be achieved by reconfiguring the formation saving important percentages of fuel. Specifically, accepting relative errors in image metrics lower than 8%, this research has proved that interesting fuel savings (up to 70% of the fuel usage planned before the reconfiguration) can be achieved during the monitoring of the final approach phase of the formation. The applicability of these type of controllers will represent an improvement in lifetime and in flexibility for the future imaging distributed telescope missions.

These achievements contribute to the research work related to Synthetic Imaging Formation Flight realized within the Space Systems Laboratory and represent a little step further in the interesting research concerning future distributed telescopes missions.

5.2 Future work

After this research the author presents some proposals for future work taking into account the experience acquired during the development of this research.

First of all, due to the delay concerning the real tests performed in the International Space Station, the first step of this further research will be the analysis of the results from the experiments of the International Space Station. They are expected to confirm the trend of the tests of the computer-based simulations and the tests realized on the MIT air table.

Once this trajectory planning algorithm will be confirmed by the ISS tests, new acceleration profiles substituting the Bang Off Bang profile could be implemented. Splines or likewise approximations will be the following approaches considered. At the same time performance of constant angular velocities trajectories should be compared to constant linear velocities trajectories because other extra improvement in image quality could be achieved. Furthermore, the effect of relative movement between spacecraft while performing observations (Drift Through maneuvers) on blurriness of images should be observed and analyzed in order to be able to determine the actual interest of these kind of maneuvers for interferometric measurements.

Considering the work related to the Optimal Imaging Controllers, and particularly the Incremental Controller, the circle constraint should be substituted by a less restrictive optimal problem, where satellites could be positioned within a limiting box. This problem is less restrictive and more representative but it represents a more difficult LQ framework in terms of resolution. Problems of convergence and of resolution would represent a new challenge to overcome. Other improvement will be the inclusion of adaptive r/a coefficients along the reconfiguration steps to take into account the inertia of the image metrics function or to emphasize particular behavior when the number of reconfigurations is increasing. Time maneuvers changes and determining maximum consumption for each step will enable a more customized trajectory design, where the mission engineer will be capable of configuring a controller that will have specific behavior for each phase of the mission (the behavior of the controller do not have to be the same throughout the whole mission).

As it has been mentioned throughout the present thesis, other computing methods should be implemented to compare ways of assuring global minima, which is always an important mathematical issue of these kind of problems. Apart from the extensive search performed in this research, deep mathematical studies could be perform in order to prove performances of heuristic methods or contraction theory. Heuristic methods do not assure global minima but contraction theory does. The latter is a theory developed at MIT by professor J.Slotine [54], that consists on transforming the non-linear system into another non-linear representation where the global minima can be determined. Afterwards, returning to the original system, it exists mathematical proof about the location of the global minima. Implementation of these kind of techniques would be extremely interesting for these controller developments.

Finally, decentralized approaches where each satellite will have the knowledge of only the state of their neighbors but not of the whole formation, will represent an interesting saving in computation time and in communication links between members of the flotilla. These improvements will permit implementation of these algorithms in low power computation machines, therefore it could be thought of implementing those controllers in SPHERES and test them in real space environment.

Appendix A

Spiral optimization expressions

A.1 Fuel and time optimal maneuvers of the double integrator plant

In this appendix, a brief recall of the main results of the application of the Maximum Principle of Poyntraguin will be done. These results of the optimal control theory applied to the double integrator plant are very useful to justify some of the ulterior results. Three main cases will be treated, the first one where only time duration is minimized, the second one where only fuel consumption is the objective of minimization and the third one where a combination of the previous two is taken into account.

In any of the next three cases, the system under analysis is the following:

$$m\ddot{x}(t) = v(t) \tag{A.1}$$

The transfer function of this system is:

$$G(s) = \frac{1}{ms^2} \tag{A.2}$$

Let's simplify the analysis by setting $u(t) = v(t)/m$ and that leads to the well known state-space representation:

$$\begin{aligned} \dot{x_1}(t) &= x_2(t) \\ \dot{x_2}(t) &= u(t) \qquad\quad |u(t)| \leq 1 \end{aligned} \tag{A.3}$$

To resolve this problem, we shall find the H-minimal control, i.e the control that minimizes the Hamiltonian. In the following three cases the hamiltonian is expressed as:

$$H = r + x_2(t)\psi_1(t) + u(t)\psi_2(t) \tag{A.4}$$

where r corresponds to the cost function criteria: $J = \int_0^T r dt$.

And the evolution of the costate variables $\psi_1(t)$ and $\psi_2(t)$ is:

$$\begin{aligned} \dot{\psi_1}(t) &= -\frac{\partial H}{\partial x_1(t)} = 0 \\ \dot{\psi_2}(t) &= -\frac{\partial H}{\partial x_2(t)} = -\psi_1(t) \end{aligned} \tag{A.5}$$

To this evolution, it follows that:

$$\begin{aligned}\psi_1(t) &= \psi_{10} = cte \\ \psi_2(t) &= \psi_{20} - \psi_{10}t\end{aligned} \tag{A.6}$$

The analysis of this evolution combined with the control that minimizes the Hamiltonian in each case, will lead to the obtention of the optimal control commands for each problem.

A.1.1 Time optimal maneuver of the double integrator plant

In this first case, the objective is time minimization, as a consequence the defined cost function which will be treated is: $J = \int_0^T dt$, what leads to the following Hamiltonian function: $H = 1 + x_2(t)\psi_1(t) + u(t)\psi_2(t)$.

For this simple case, the control which minimizes the Hamiltonian is found to be $u(t) = -sgn\{\psi_2(t)\} = \Delta = \pm 1$.

Analyzing possible evolution of $\psi_2(t)$, the only four possible control sequences are:$\{+1\}$,$\{-1\}$,$\{+1,-1\}$, $\{-1,+1\}$.

Considering Δ constant over a finite period of time, we can solve the evolutions of the state variables, and we state that:

$$\begin{aligned}x_2(t) &= x_2(0) + \Delta t \\ x_1(t) &= x_1(0) + x_2(0)t + \tfrac{1}{2}\Delta t^2\end{aligned} \tag{A.7}$$

where we can eliminate the time to find a trajectory within the x_1x_2 plane to state:

$$x_1 = x_1(0) + \frac{1}{2}\Delta x_2^2 - \frac{1}{2}\Delta x_2(0)^2 \tag{A.8}$$

Our interest is to reach a well known state (in this case we suppose $(0,0)$), as a consequence, within these set of trajectories, of special interest are those two which lead towards $(0,0)$.

We define: The γ_+ curve is the locus of all points of the plane which can be force to $(0,0)$ by the control $u(t) = +1$ and analogously γ_- curve by the control $u(t) = -1$:

$$\begin{aligned}\gamma_+ &= \{(x_1,x_2) : x_1 = \tfrac{1}{2}x_2^2; x_2 < 0\} \\ \gamma_- &= \{(x_1,x_2) : x_1 = -\tfrac{1}{2}x_2^2; x_2 \geq 0\}\end{aligned} \tag{A.9}$$

The union of these two curves is called the switch curve, which divides the state plane (x_1,x_2) in two regions R_- and R_+. This division can be visualized in figure A.1.

$$\begin{aligned}\gamma &= \{(x_1,x_2) : x_1 = -\tfrac{1}{2}x_2|x_2|; x_2 \geq 0\} \\ R_- &= \{(x_1,x_2) : x_1 > -\tfrac{1}{2}x_2|x_2|\} \\ R_+ &= \{(x_1,x_2) : x_1 < -\tfrac{1}{2}x_2|x_2|\}\end{aligned} \tag{A.10}$$

So finally, the time-optimal control law u^* as a function of the state is given by:

$$\begin{aligned}u^* = u^*(x_1,x_2) &= +1 \qquad \text{for all} \quad (x_1,x_2) \in \gamma_+ \cup R_+ \\ u^* = u^*(x_1,x_2) &= -1 \qquad \text{for all} \quad (x_1,x_2) \in \gamma_- \cup R_-\end{aligned} \tag{A.11}$$

which defines a value to the optimal control u^* for every state in the state plane, defining then the closed loop time optimal control system. The acceleration profile of this solution is also known as Bang-Bang.

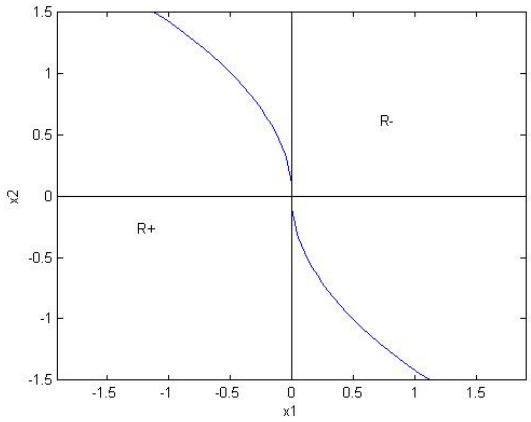

Figure A.1: *Illustration of the switch curve for the double integrator plant*

A.1.2 Fuel optimal maneuver of the double integrator plant

In this case, the analysis is quite similar but having the objective of minimizing the fuel consumption leads us to define the new cost function as follows: $J = J(u) = \int_0^T |u(t)|dt$. What permits us to find the hamiltonian H for this problem: $H = |u(t)| + x_2(t)\psi_1(t) + u(t)\psi_2(t)$.

In this case, what minimizes the Hamiltonian is given by:

$$\begin{array}{ll} u(t) = 0 & \text{if} \quad |\psi_2(t)| < 1 \\ u(t) = -sgn\{\psi_2(t)\} & \text{if} \quad |\psi_2(t)| > 1 \\ 0 \leq u(t) \leq 1 & \text{if} \quad \psi_2(t) = -1 \\ -1 \leq u(t) \leq 0 & \text{if} \quad \psi_2(t) = 1 \end{array} \tag{A.12}$$

Ignoring the particular situation when $\psi_1 = 0$ where a particular optimal control candidate can be found ([24]), for values of $\psi_1 \neq 0$, taking into account the evolution of the costate variables, only nine control sequences could be envisaged:$\{0\}$,$\{+1\}$,$\{-1\}$,$\{+1, 0\}$,$\{-1, 0\}$,$\{0, +1\}$,$\{0, -1\}$,$\{+1, 0, -1\}$,$\{-1, 0, +1\}$. Within this set of possible control sequences, there are some that lead to singular controls which do not lead to the desired position leaving this problem with no solutions for some case, aspect that will be analyzed at the end of this section.

In comparison to the cases analyzed in the previous section, only the evolution of the state variables when $u(t) = 0$ should be studied to extract some conclusion. Thus,

$$\begin{array}{l} x_2(t) = x_2(0) \\ x_1(t) = x_1(0) + x_2(0)t \end{array} \tag{A.13}$$

what means that the trajectories are horizontal lines that move from left to right if $x_2 > 0$ and from right to left if $x_2 < 0$ (in the state plane). Adding this new reasoning, and having in mind the definition of the switch curve combined with the x_1 axis (which divides the space of positive x_2 from the negative x_2, 4 new regions of the state plane can be defined:

$$\begin{array}{lll} R_1 = \{(x_1, x_2) : x_2 \geq 0; x_1 > x_1^{'}, & \text{where} & (x_1^{'}, x_2) \in \gamma_-\} \\ R_2 = \{(x_1, x_2) : x_2 > 0; x_1 < x_1^{'}, & \text{where} & (x_1^{'}, x_2) \in \gamma_-\} \\ R_3 = \{(x_1, x_2) : x_2 \leq 0; x_1 < x_1^{'}, & \text{where} & (x_1^{'}, x_2) \in \gamma_+\} \\ R_4 = \{(x_1, x_2) : x_2 < 0; x_1 > x_1^{'}, & \text{where} & (x_1^{'}, x_2) \in \gamma_+\} \end{array} \tag{A.14}$$

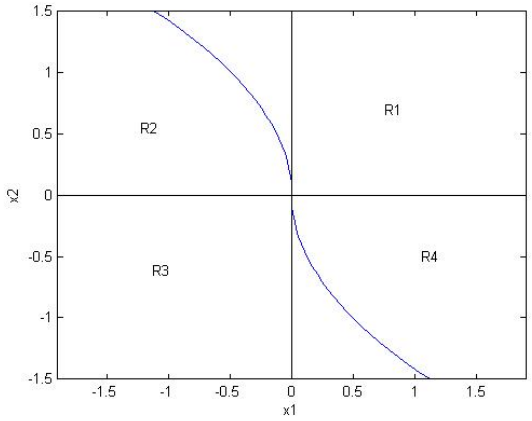

Figure A.2: *The switch curve and the $x_2 = 0$ axis divide the state space into four sets*

Once this regions are set, the optimal control law can be determined:

$$\begin{array}{lll} u^* = u^*(x_1, x_2) = +1 & \text{for all} & (x_1, x_2) \in \gamma_+ \\ u^* = u^*(x_1, x_2) = -1 & \text{for all} & (x_1, x_2) \in \gamma_- \\ u^* = u^*(x_1, x_2) = 0 & \text{for all} & (x_1, x_2) \in R_2 \cup R_4 \end{array} \tag{A.15}$$

If $(x_1, x_2) \in R_1 \cup R_3$, then there is no fuel-optimal control. But, as it is stated in [24], a quasi-fuel-optimal sequence can be determined if a sequence $\{-1, 0, +1\}$ is imposed what which lead the plant from region R_1 to R_4 and from there until the desired final position (analogous for R_3, with the sequence $\{+1, 0, -1\}$. Please refer to the commented references for further detail in this analysis.

A.1.3 Combination of time-fuel optimal maneuver of the double integrator plant

In this final case of study, the function cost is defined as a linear combination between both previous cases. As a consequence, the cost function and the resulting Hamiltonian could be defined respectively as:

$$\begin{array}{l} J(u) = J = \int_0^T [k + |u(t)|]dt \\ H = k + |u(t)| + x_2(t)\psi_1(t) + u(t)\psi_2(t) \end{array} \tag{A.16}$$

In this problem, with the inclusion of parameter k, all singular controls are eliminated because they cannot be optimal. Since the system is time-invariant, since the cost functional J is time-invariant and since T is not fixed, the Hamiltonian must be identically zero along an optimal trajectory, so then the possibility of having $|\psi_2(t)| = 1$ is not part of the possible optimal solutions.

Hence, the control that minimizes the Hamiltonian are

$$\begin{array}{lll} u(t) = 0 & \text{if} & |\psi_2(t)| < 1 \\ u(t) = -sgn\{\psi_2(t)\} & \text{if} & |\psi_2(t)| > 1 \end{array} \tag{A.17}$$

From the nine possible control sequences only six can be candidates for the optimal control problem because any control sequence ending with $u(T) = 0$ leads to $H(T) = k > 0$, what, as before, cannot be optimal.

Therefore, the only six control sequences are:$\{+1\}$, $\{-1\}$, $\{0, +1\}$, $\{0, -1\}$,$\{+1, 0, -1\}$,$\{-1, 0, +1\}$. The first four are subsequences of the two latter ones, so an analysis could be done only for the last ones and then extended to all these six combinations, because by the principle of optimality, we can conclude that if a sequence is optimal, then every one of its subsequences must be optimal.

In these control sequences, there are two commutation instants and those two could be associated with two plane points. The first instant is when the spacecraft passes from a certain command ± 1 towards a zero command and is defined in the plane state as (a_1, a_2). The second instant is the commutation from the absence of command $(u(t) = 0)$ towards $u(t) = \pm 1$ and let us defined this state as (b_1, b_2).

Stating that $(b_1, b_2) \in \gamma$ and that the Hamiltonian should be zero all along the trajectory, the locus of the switching points (a_1, a_2) can be easily determined. This locus defines a curve as a function of k:

$$\Gamma_k = \{(x_1, x_2) : x_1 = -\frac{k+4}{2k} x_2|x_2|\} \tag{A.18}$$

As before, the junction of the switch curve and this new defined curve, leads to the definition of this new four regions (visible in the figure A.3).

$$\begin{array}{l} D_1 = \{(x_1, x_2) : x_1 \geq -\frac{1}{2}x_2|x_2| \quad \text{and} \quad x_1 > -\frac{k+4}{2k}x_2|x_2|\} \\ D_2 = \{(x_1, x_2) : x_1 < -\frac{1}{2}x_2|x_2| \quad \text{and} \quad x_1 \geq -\frac{k+4}{2k}x_2|x_2|\} \\ D_3 = \{(x_1, x_2) : x_1 \leq -\frac{1}{2}x_2|x_2| \quad \text{and} \quad x_1 < -\frac{k+4}{2k}x_2|x_2|\} \\ D_4 = \{(x_1, x_2) : x_1 > -\frac{1}{2}x_2|x_2| \quad \text{and} \quad x_1 \leq -\frac{k+4}{2k}x_2|x_2|\} \end{array} \tag{A.19}$$

This last analysis leads us to the definition of the unique optimal control law u^* for the time-fuel problem as a function of the state (x_1, x_2):

$$\begin{array}{lll} u^* = u^*(x_1, x_2) = -1 & \text{for all} & (x_1, x_2) \in D_1 \\ u^* = u^*(x_1, x_2) = +1 & \text{for all} & (x_1, x_2) \in D_3 \\ u^* = u^*(x_1, x_2) = 0 & \text{for all} & (x_1, x_2) \in D_2 \cup D_4 \end{array} \tag{A.20}$$

This last case, represents a more general case of study because ponderation of the parameter k, allows us to determine different optimal control laws with difference relative importance of the time minimization in relation to the fuel minimization. As an asymptotical behavior, it is easily observed that the curve Γ_k tends to the switch curve when $k \to \infty$ and we find again the time optimal problem. On the other hand, when $k \to 0$, the Γ_k tends to the curve $x_2 = 0$, which represents the fuel optimal problem that it has been stated in the previous section.

The structure of this type of law, where a sequence of acceleration-coast-acceleration takes place is often known as Bang-Off-Bang control law and this specific case where time and fuel are about to be minimized as a combined function represents the scenario of the greatest interest for the

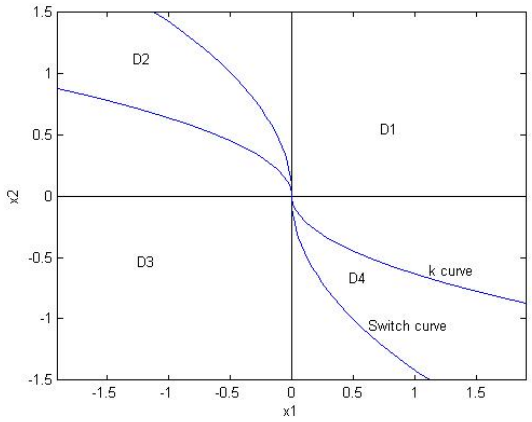

Figure A.3: *The switch curve and the Γ_k curve divide the state space into four sets*

most applications in aerospace where the resources are limited and the time to realize the mission is bounded, because minimizing the maneuver time means increasing of the science output of the mission.

A.2 Polynomial expression of the design process

As it has been stated in the design process section, after the physics analysis of the spirals maneuvers and the introduction of the acceleration profile designed to be the optimum, the resolution process leads to solve a two non linear equation system dependent on γ and t_f which are the two configuration parameters.

After all the calculus mentioned in section 3.2.3 the resulting expressions are, for the first instant ($\Upsilon_1(\gamma, t_f)$) and for the second ($\Upsilon_2(\gamma, t_f)$), respectively.

$$\begin{aligned}\Upsilon_1(\gamma, t_f) &= (a + b\alpha t_f^2[-3c^2/2 - c])^2(\alpha^2 + (\alpha\gamma t_f)^4)+ \\ &\quad (b\alpha)^2(1 + 4(\alpha\gamma t_f)^2)- \\ &\quad (a + b\alpha t_f^2[-3c^2/2 - c])2b\alpha^3(\gamma t_f)^2 - (\Gamma/m)^2\end{aligned} \tag{A.21}$$

$$\Upsilon_2(\gamma, t_f) = \alpha^2((a + bt_f^2\alpha\gamma(1-\gamma)) + b^2) - (\Gamma/m)^2 \tag{A.22}$$

where, as it was stated, $\alpha = \frac{\theta}{t_f^2\gamma(1-\gamma)}$. So then, in order to find the second equation, which is $\frac{d\Upsilon(\gamma,t_f)}{d\gamma}$ we have to consider the dependency of α in relation to γ. The obtention of this second equation does not represent any mathematical difficulty as it represents the result of a standard derivation process, therefore, and taking into consideration the big size of this formula and the little scientific interest of writing it, the author has considered more appropriate to show the evolution of both functions in the graphics below, where we can observe the good correspondence between the function and its derivative.

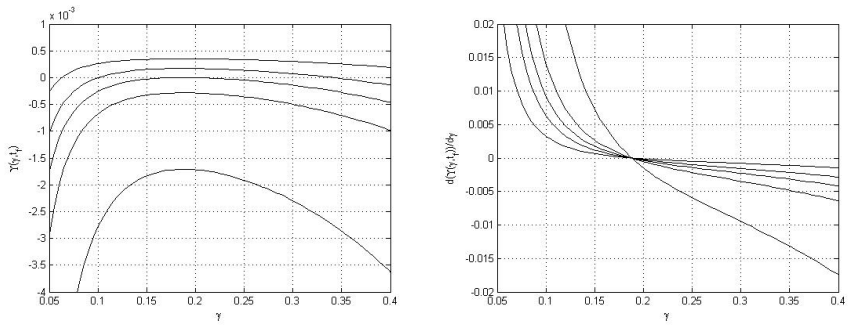

(a) (b)

Figure A.4: *Representation of: a)* $\Upsilon(\gamma, t_f)$ *and b)* $\frac{d\Upsilon(\gamma,t_f)}{d\gamma}$ *for different values of* t_f.

A.3 Fuel usage expressions

Once all parameters of the acceleration profile are determined the trajectory design is finished, and, as a continuation, the theoretical fuel usage of this trajectory which will be likely to be compared to the simulations realized on SPHERES testbed.

The fuel consumption evolution could be modeled as follows:

$$\dot{f(t)} = \begin{cases} -\mu(\Gamma_r + \Gamma_\theta) & f(t) > 0 \\ 0 & f(t) < 0 \end{cases} \tag{A.23}$$

where μ is a proportionality constant and Γ_r and Γ_θ are thruster demands in radial and transversal directions respectively.

As a consequence, the fuel usage calculus is simply stated as:

$$f(t) - f(0) = -\mu \int_0^t (|ma_r| + |ma_\theta|)dt \tag{A.24}$$

Therefore, this calculus could be structured in three phases, because as it has been stated in the previous section, the acceleration profile of the open loop law varies depending on the phase that is being driven: Acceleration phase, coast phase or deceleration phase. This calculus are the strict application of equation A.24.

In order to draw conclusions about the design and compare the theoretical results with results from the SPHERES experience, this calculus have been made and coded, so then the author has considered necessary to reference it at least within this appendix.

A.3.1 First phase: acceleration phase

Starting from equation A.24, and substituting for the right values stated in previous sections (archimedean spiral), this consumption can be calculated like that.

$$\begin{aligned} f(t_a) - f(0) &= -\mu \textstyle\int_0^{t_a} (|ma_r| + |ma_\theta|)dt = \\ &= -\mu m[(a-b)\alpha t_a + (\tfrac{5b}{6} + \tfrac{a}{3})\alpha^2 t_a^3 + \tfrac{b\alpha^3}{10} t_a^5] \end{aligned} \tag{A.25}$$

A.3.2 Second phase: coast phase

Doing an analogous calculus, the consumption during the coast phase (within the time interval: $t_a < t < t_f - t - a$) can be determined. It is worth mentioning that despite being a "coast phase", there is fuel consumption to maintain a curve trajectory and a certain spiraling rate.

$$\begin{aligned} f(t_f - t_a) - f(t_a) &= -\mu \int_{t_a}^{t_f - t_a} (|ma_r| + |ma_\theta|)dt = \\ &= -\mu m[\Big((2b+a)\alpha^2 t_a^2 - \tfrac{b}{2}\alpha^3 t_a^4\Big)(t_f - 2t_a) + \tfrac{b\alpha^3 t_a^3}{2}(t_f^2 - 2t_f t_a)] \end{aligned} \tag{A.26}$$

A.3.3 Third phase: deceleration phase

Finally, in the third phase, same calculus and reasoning should take place. Resolving this integral analytically, oblige us to find the sign of both accelerations. In both previous cases, during the whole integration time centripetal acceleration was always negative and transversal acceleration always positive. In this final case, centripetal acceleration still being negative but on the other hand, determining the sign of the transversal acceleration depends on the spiraling rate of the spiral and on the thrust time. If this thrust time is small, high acceleration is needed to decrease the angular rate, so then this transversal acceleration will be negative. Particularly, for this case of archimedean spirals and with the acceleration profile determined previously, this condition is : $\gamma < 2/7$. When this thrust time is larger than the previous condition, the angular acceleration needed is not as high, so then in order to have a negative transversal acceleration the condition is on the spiraling rate.

$$b < \frac{2a}{\alpha t_f(7\gamma^2 - 2\gamma)} \tag{A.27}$$

These conditions have been obtained analyzing the polynomial expression of the transversal acceleration of the spiral, finding its roots and analyzing those with physical meaning. Taking them into account, their consumption can be calculated and it has been calculated in order to be able to compute the whole fuel consumption of the maneuver.

$$\begin{aligned} f(t_f) - f(t_f - t_a) &= -\mu \int_{t_f - t_a}^{t_f} (|Ma_r| + |Ma_\theta|)dt = \\ &= -\mu M[At_a + \tfrac{B}{2}(t_f^2 - (t_f - t_a)^2) + \tfrac{C}{3}(t_f^3 - (t_f - t_a)^3) + \\ &\tfrac{D}{4}(t_f^4 - (t_f - t_a)^4) + \tfrac{E}{5}(t_f^5 - (t_f - t_a)^5)] \end{aligned} \tag{A.28}$$

where,

$$\begin{aligned} A &= (a+b)\alpha + (a - \tfrac{5b}{2})\alpha^2 t_f^2 + \alpha^2 b t_a(t_f - t_a) + b\alpha^3 t_a t_f^2(t_f - t_a) - \tfrac{b\alpha^3}{2}t_f^4 \\ B &= (5b - 2a)\alpha^2 t_f - 2b\alpha^3 t_a t_f(t_f - t_a) + 2b\alpha^3 t_f^3 \\ C &= (a - \tfrac{5b}{2})\alpha^2 + b\alpha^3 t_a(t_f - t_a) - 3b\alpha^3 t_f^2 \\ D &= 2b\alpha^3 t_f \\ E &= -\tfrac{b\alpha^3}{2} \end{aligned} \tag{A.29}$$

A.4 Open-loop control law expressions

Once the whole trajectory parameters and the fuel usage are perfectly determined, it is time to state the open-loop control law that should be implemented to follow this kind of trajectories with the mentioned fuel consumption.

The thrust that would have to be demanded to the double-integrator plant would be a combination of thrust in the radial direction and in the transversal direction, that are defined like that:

$$\overrightarrow{\mathbf{\Gamma}} = m\overrightarrow{\boldsymbol{a}} = m(a_r\widehat{\boldsymbol{e}_r} + a_\theta\widehat{\boldsymbol{e}_\theta}) = m(a_r\widehat{\boldsymbol{e}_r} + a_\theta(\widehat{\boldsymbol{z}} \times \widehat{\boldsymbol{e}_r})) \tag{A.30}$$

In order to determine the thrust in the coordinate dimensions, it is stated:

$$\widehat{\boldsymbol{e}_r} = \cos(\psi)\widehat{\boldsymbol{x}} + \sin(\psi)\widehat{\boldsymbol{y}} \tag{A.31}$$

where ψ is the angle of the spacecraft's position vector respect to the coordinate frame. Thus,

$$\begin{aligned} \overrightarrow{\mathbf{\Gamma}} &= m(u_x\widehat{\boldsymbol{x}} + u_y\widehat{\boldsymbol{y}}) \\ &= m((a_r\cos(\psi) - a_\theta\sin(\psi))\widehat{\boldsymbol{x}} + (a_r\sin(\psi) + a_\theta\cos(\psi))\widehat{\boldsymbol{y}}) \end{aligned} \tag{A.32}$$

Taking into account all definitions made during the design process, the radial and the transversal acceleration necessary to compute the open loop commands stated in A.32 should be computed as follows in the three different phases. These open-loop commands are implemented as the trajectory planning algorithms to the tracking stages of the control architecture.

The results for the acceleration, coast and deceleration phase for the case treated in this thesis are the following:

$$0 < t < t_a : \begin{cases} a_r = b\alpha - a(\alpha t)^2\frac{b}{2}\alpha^3 t^4 \\ a_\theta = a\alpha + \frac{5b}{2}(\alpha t)^2 \end{cases} \tag{A.33}$$

$$t_a < t < t_f - t_a : \begin{cases} a_r = (-a + \frac{b\alpha}{2}t_a^2 - b\alpha t_a t)(\alpha t_a)^2 \\ a_\theta = 2b(\alpha t_a)^2 \end{cases} \tag{A.34}$$

$$t_f - t_a < t < t_f : \begin{cases} a_r = -b\alpha - (a + b\alpha(t_a(t_f - t_a) - \frac{(t_f - t_a)^2}{2}))\alpha^2(t_f - t)^2 \\ a_\theta = -\alpha(a + b\alpha(t_a(t_f - t_a) - \frac{(t_f - t_a)^2}{2})) + 2b\alpha^2(t_f - t)^2 \end{cases} \tag{A.35}$$

Appendix B

Optimal Imaging Controllers results

In this appendix, an extended collection of results is shown to complement the whole graphical documentation presented in this thesis concerning the Optimal Imaging Controllers designed.

B.1 Incremental Controller

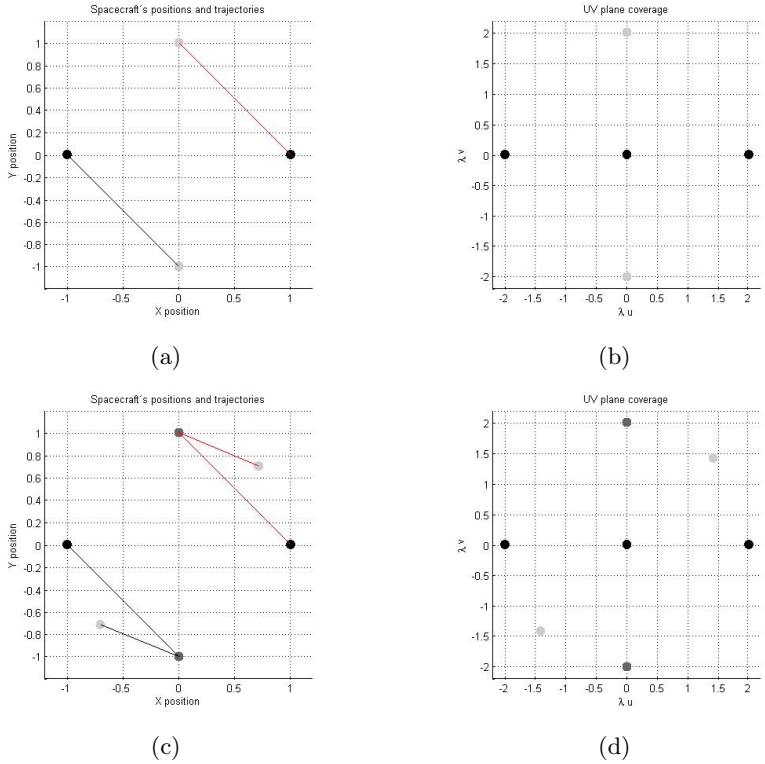

Figure B.1: *First two steps performed by the optimal controller with low r/a ratio: a) XY plane (first step) b) UV plane (first step) c) XY plane (second step) d) UV plane (second step)*

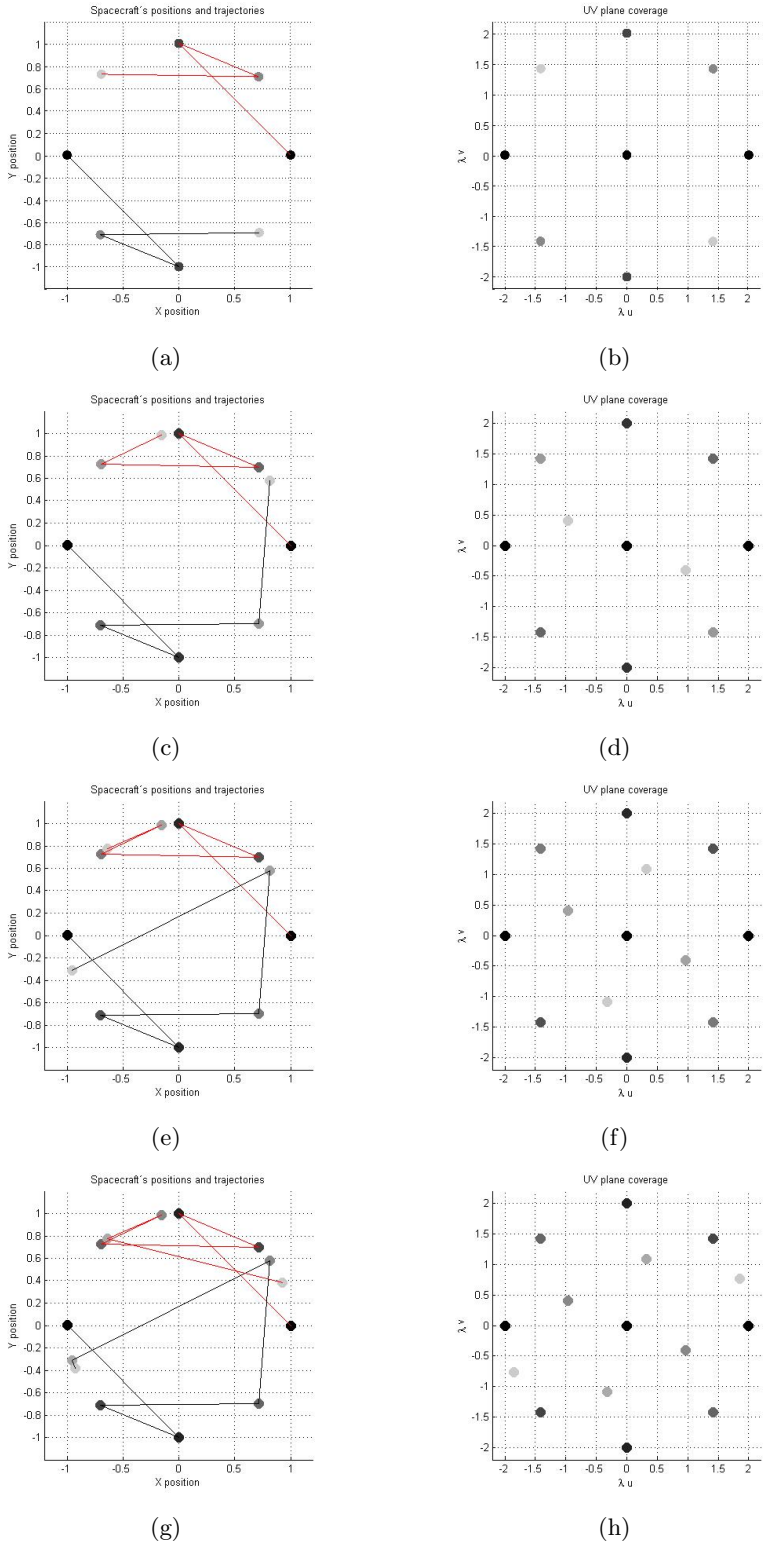

(a) (b)

(c) (d)

(e) (f)

(g) (h)

Figure B.2: *Steps 3, 4, 5 and 6 performed by the optimal controller with low r/a ratio: a) XY plane (third step) b) UV plane (third step) c) XY plane (fourth step) d) UV plane (fourth step) e) XY plane (fifth step) f) UV plane (fifth step) g) XY plane (sixth step) h) UV plane (sixth step)*

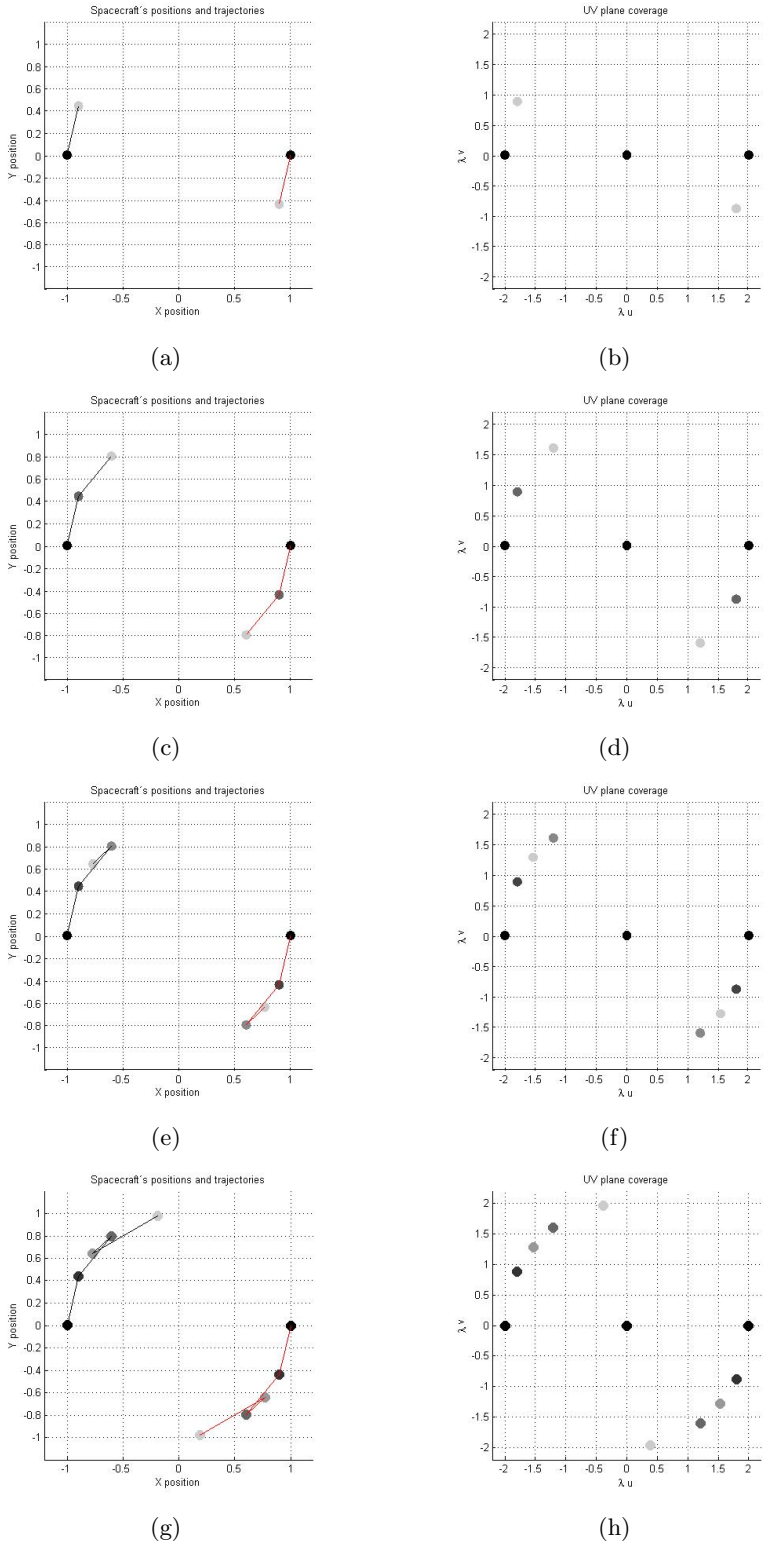

Figure B.3: *First four steps performed by the optimal controller with high r/a ratio: a) XY plane (first step) b) UV plane (first step) c) XY plane (second step) d) UV plane (second step) e) XY plane (third step) f) UV plane (third step) g) XY plane (fourth step) h) UV plane (fourth step)*

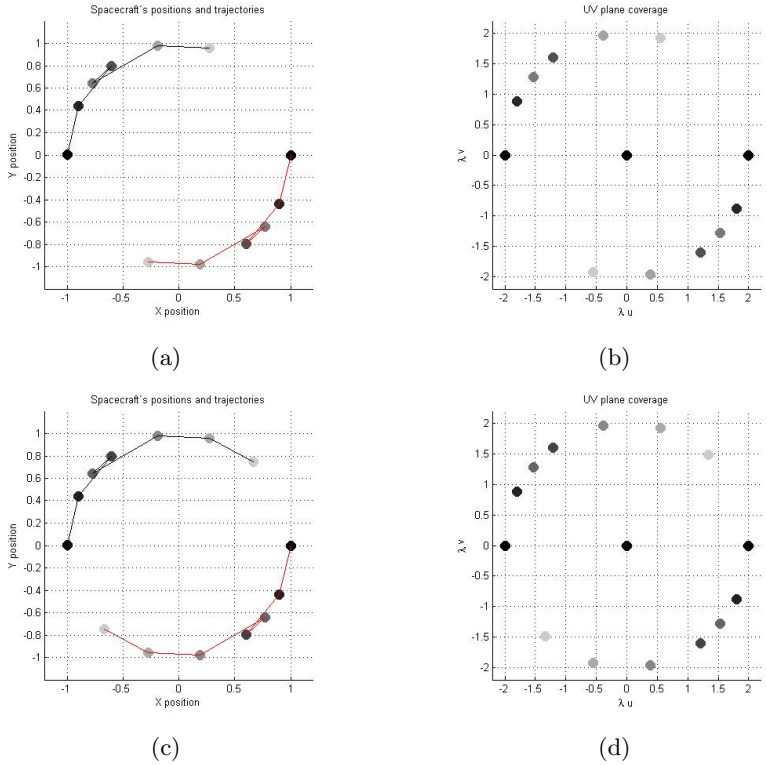

Figure B.4: *Steps 5 and 6 performed by the optimal controller with high r/a ratio: a) XY plane (fifth step) b) UV plane (fifth step) c) XY plane (sixth step) d) UV plane (sixth step)*

B.2 Position Redefining Controller

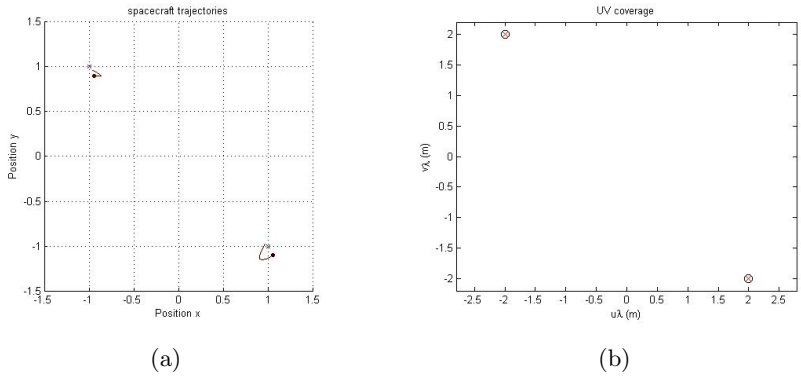

Figure B.5: *Repositioning of a 2 satellites formation with low r/a ratio : a) XY plane b) UV plane*

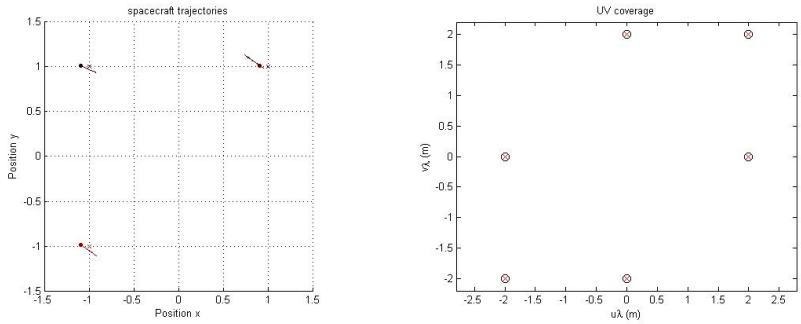

(a) (b)

Figure B.6: *Repositioning of a 3 satellites formation with low r/a ratio : a) XY plane b) UV plane*

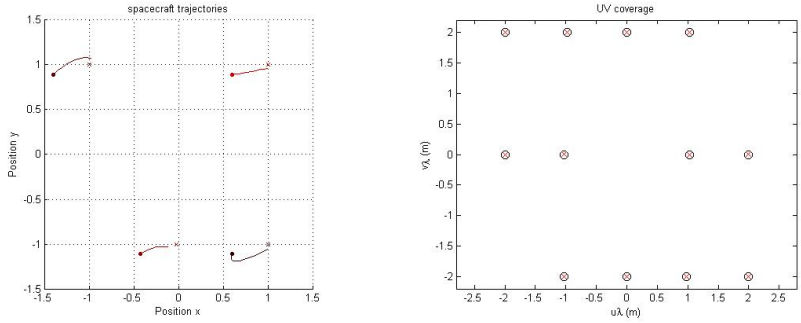

(a) (b)

Figure B.7: *Repositioning of a 4 satellites formation with low r/a ratio : a) XY plane b) UV plane*

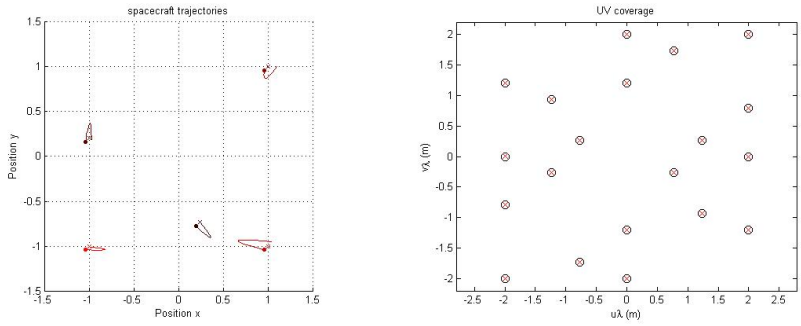

(a) (b)

Figure B.8: *Repositioning of a 5 satellites formation with low r/a ratio : a) XY plane b) UV plane*

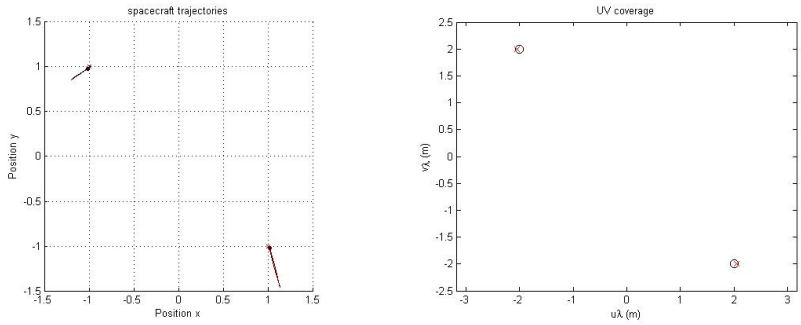

(a) (b)

Figure B.9: *Repositioning of a 2 satellites formation with high r/a ratio : a) XY plane b) UV plane*

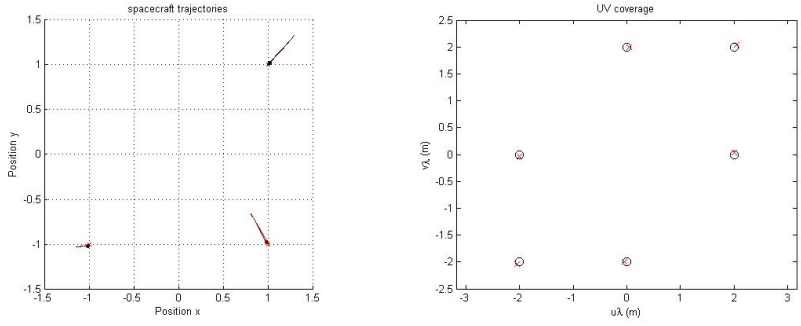

(a) (b)

Figure B.10: *Repositioning of a 3 satellites formation with high r/a ratio : a) XY plane b) UV plane*

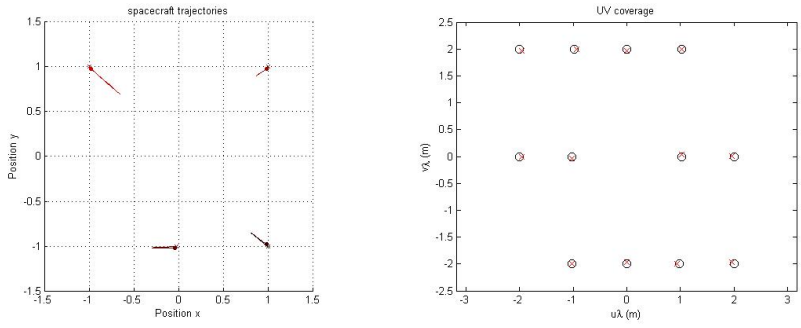

(a) (b)

Figure B.11: *Repositioning of a 4 satellites formation with high r/a ratio : a) XY plane b) UV plane*

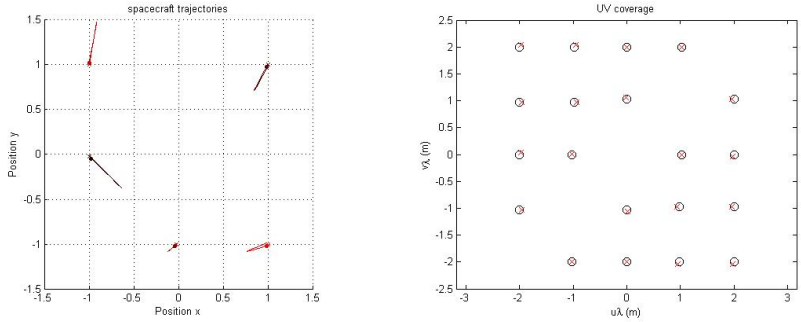

(a) (b)

Figure B.12: *Repositioning of a 5 satellites formation with high r/a ratio : a) XY plane b) UV plane*

Bibliography

[1] F.M. Naderi, *NASA Origins and Fundamental Physics Program.* SPIE's International Symposium on Astronomical Telescopes and Instrumentations. Paper no. 3350-125. March, 1998.

[2] JET PROPULSION LABORATORY, *Origins Program* http://origins.jpl.nasa.gov/index1.html

[3] Space Telescope Science Institute, *General Overview of the Hubble Space Telescope* http://www.stsci.edu/hst/

[4] M. Wehner, S. Moses, K. Kroening, E. Johnson, *Terrestrial Planet Finder Space Vehicle Architecture Trades.* SPIE Conference on Astronomical Interferometry, Kona, Hawaii. March, 1998.

[5] M. Fridlund, R. den Hartog, A. Karlsson, *Scientific Requirements on Space Interferometers.* JENAM2005 "Distant Worlds": Technology Roadmap for Future Interferometric Facilities. Liège. Belgium. 4-7 July, 2005.

[6] K.G. Carpenter et al, *Vision Mission Study Report* NASA Goddard Space Flight Center. September, 2005.

[7] K.G. Carpenter et al, *The Stellar Imager (SI) Mission Concept.* NASA Goddard Space Flight Center. September, 2005.

[8] K.G Carpenter et al, *The Stellar Imager (SI): A revolutionary Large-Baseline Imaging Interferometer at the Sun-Earth L2 point.* NASA Goddard Space Flight Center. 2005.

[9] D.P Scharf, F.Y. Hadaegh, S.R. Ploen, *A survey of spacecraft formation flying guidance and control (part 1): Guidance.* Proceedings of the American Control Conference. June 4-6, 2003.

[10] D.P Scharf, F.Y. Hadaegh, S.R. Ploen, *A survey of spacecraft formation flying guidance and control (part 2): Control.* JPL Electronic Library. 2004.

[11] S. Mohan, H. Sakamoto, D. Miller, *Formation control and reconfiguration through synthetic imaging formation flying testbed (SIFFT).* SPIE Optics & Photonics, San Diego, California. August, 2007.

[12] Ch. Mandy, A. Saenz-Otero, D. Miller *Satellite Formation Flight and Realignment Maneuver Demonstration aboard the International Space Station.* SPIE Optics & Photonics, San Diego, California. August, 2007.

[13] Ch. Mandy, H. Sakamoto, A. Saenz-Otero, D. Miller, *Implementation of Satellite Formation Flight Algorithms Using SPHERES aboard the International Space Station*. International Symposium on Space Flight Dynamics, Annapolis, MD. September, 2007.

[14] A. Saenz-Otero, *The SPHERES Satellite Formation Flight Testbed: Design and Initial Control*. M.S. Thesis. Massachusetts Institute of Techonology. August, 2000.

[15] A. Saenz-Otero, *Design Principles for the Development of Space Technology Maturation Laboratories Aboard the International Space Station*. PhD Thesis. Massachusetts Institute of Techonology. June 2005.

[16] M.O. Hilstad, *A Multi-Vehicle Testbed and Interface Framework for the Development and Verification of Separated Spacecraft Control Algorithms*. M.S Thesis. Massachusetts Institute of Technology. May, 2002.

[17] S. Nolet, *Development of a Guidance, Navigation and Control Architecture and Validation Process Enabling Autonomous Docking to a Tumbling Satellite*. PhD Thesis. Massachusetts Institute of Techonology. June, 2007.

[18] M.O. Hilstad, J.P. Enright, A.G. Richards *The SPHERES Guest Scientist Program*. Massachusetts Institute of Technology. Space Systems Laboratory. 2003.

[19] A. Saenz-Otero, *Appendix G Spheres Software Design* M.S Thesis. Massachusetts Institute of Technology. June, 2005.

[20] R.W. Beard, F.Y. Hadaegh, *Fuel Optimized Rotation for Satellite Formations in Free Space*. Proceedings of the American Control Conference. San Diego, California. June, 1999.

[21] R.W. Beard, F.Y. Hadaegh, *Fuel Optimization for Unconstrained Rotation of Spacecraft Formations*. The Journal of the Astronautical Sciences, Vol. 47 Nos. 3 and 4. July-December, 1999.

[22] R.W. Beard, T.W. McLain, F.Y. Hadaegh, *Fuel Optimization for Constrained Rotation of Spacecraft Formations*. The Journal of Guidance Control and Dynamics, Vol. 23 No. 2. March-April, 2000.

[23] C.A. Bailey, T.W. McLain, R.W. Beard *Fuel saving strategies for separated spacecraft interferometry*. AIAA Guidance, Navigation and Control Conference. 14-17 August, 2000.

[24] M. Athans, P.L Falb *Optimal Control*. Dover Publication Inc. Mc Graw Hill, 1966.

[25] D.E. Kirk *Optimal Control Theory: An Introduction*. Prentice Hall Inc. Englewood Cliffs. New Jersey, 1970.

[26] R.A. Laskin, *Technology For Space Optical Interferometry*. American Institute of Aeronautics and Astronautics. 2005.

[27] A. Labeyrie, H. Le Coroller, *Extrasolar planet imaging*. New Frontiers in Stellar Interferometry, edited by Wesley A. Traub, Proceedings of SPIE Vol. 5491. 2004.

[28] M. Faucherre, B. Delabre, P. Dierickx, F. Merkie, *Michelson versus Fizeau type beam combination : Is there a difference?*. SPIE Vol. 1237 Amplitude and Intensity Spatial Interferometry. 1990.

[29] A. Labeyrie, *Comparison of ELTs, interferometers and hypertelescopes for deep field imaging and coronagraphy*. Collège de France. Observatoire de Calern, Caussols, France. Elsevier Masson SAS. August, 2007.

[30] P.Y. Bely, CJ. Burrows, F. Roddier, *A Space Interferometer Concept for the Detection of Extrasolar Earth-like Planets*. SPIE Vol. 1237 Amplitude and Intensity Spatial Interferometry. 1990.

[31] S.R. Martin., R. Morgan, S.M. Gunter, R. Bartos, *The StarLight space interferometer: optical design and performance modeling*. Interferometry in Space, Michael Shao, Editor, Proceedings of SPIE Vol. 4852. 2003.

[32] A. Labeyrie, S.G. Lipson, P. Nisenson, *Optical Stellar Interferometry*. Cambridge University Press. 2006.

[33] M. Golay, *Point arrays having compact non-redundant autocorrelations*. Journal of Optical Society of America, Vol. 61. 1971.

[34] T.J. Cornwell *A novel principle for optmization of the instantaneous Fourier plane coverage of correlation arrays*. IEEE Transactions on Antennas and Propagation, Vol. 36, No. 8. August, 1988.

[35] S.W. Golomb and H. Taylor *Two-Dimensional Synchronization Patterns for Minimum Ambiguity*. IEEE Transactions on Information Theory Vol. IT-28, No. 4. July, 1982.

[36] E.M. Kong, D.W. Miller, R.J. Sedwick, *Optimal trajectories and orbit design for separated spacecraft interferometry*. M.S Thesis. Massachusetts Institute of Techonology. November, 1998.

[37] E.M. Kong, *Spacecraft formation flight exploiting potential fields*. PhD Thesis. Massachusetts Institute of Techonology. February, 2002.

[38] A.R. Thompson, J.M. Moran, G.W. Swenson Jr., *Interferometry and synthesis in radio astronomy*. 1986.

[39] C.D. Jilla, *Separated Spacecraft Interferometry - System Architecture Design and Optimization*. M.S. Thesis. Massachusetts Institute of Technology. 1998.

[40] JET PROPULSION LABORATORY, *Space Interferometry Mission*. http://planetquest.jpl.nasa.gov/SIMLite/sim_index.cfm

[41] D. Miller, O. de Weck, S.J. Chung, *Introduction to optics*. Internal Documentation. Space Systems Laboratory. Massachusetts Institute of Technology. February, 2001.

[42] JET PROPULSION LABORATORY, *Palomar Testbed Interferometer*. http://pti.jpl.nasa.gov/

[43] Keck Observatory, *Keck Interferometer*. https://www.keckobservatory.org/

[44] JET PROPULSION LABORATORY, *Large Binocular Telescope Interferometer*. http://planetquest.jpl.nasa.gov/lbti/lbti_index.cfm

[45] The MMT Observatory, *Multiple Mirror Telescope*. http://www.mmto.org/

[46] National Radio Astronomy Observatory, *Very Large Array*. http://www.vla.nrao.edu/

[47] MERLIN National Facility, *Multi-Element Radio Linked Interferometer Network*. http://www.merlin.ac.uk/

[48] JET PROPULSION LABORATORY, *Planet Imager* http://origins.jpl.nasa.gov/missions/missions.html#pi

[49] S. Chakravorty, J. Ramirez, *Fuel Optimal Maneuvers for Multispacecraft Interferometric Imaging Systems*. Journal of Guidance Control and Dynamics, Vol. 30 No. 1. January-February, 2007.

[50] S. Chakravorty, *Design and optimal control of Multi-spacecraft Interferometic imaging systems*. PhD Thesis. Department of Aerospace Engineering, University of Michigan, Ann Arbor, MI. 2004.

[51] S. Chakravorty, P.T. Kabamba, D.C. Hyland *Modeling of image formation in Multi-spacecraft interferometric imaging systems*. AIAA Space 2004 Conference and Exposition, Vol. 1. 2004.

[52] M.A. Branch, T.F. Coleman, Y. Li, *A Subspace, Interior, and Conjugate Gradient Method for Large-Scale Bound-Constrained Minimization Problems*. SIAM Journal on Scientific Computing, Vol. 21, No. 1. 1999.

[53] R.H. Byrd, J.C. Gilbert, J. Nocedal, *A Trust Region Method Based on Interior Point Techniques for Nonlinear Programming*. Mathematical Programming, Vol. 89, No. 1. 2000.

[54] J.E. Slotine, *Non-linear control design. Class 2.152*. MIT courses.